

Southern Methodist University

SMU Scholar

---

Earth Sciences Theses and Dissertations

Earth Sciences

---

Spring 5-11-2024

# THE GEOLOGY AND GEOCHEMISTRY OF THE WESTERN IRON ORE GROUP GREENSTONE BELT, SINGHBHUM CRATON, EASTERN INDIA

JORDAN WRIGHT  
wrightjk@smu.edu

Follow this and additional works at: [https://scholar.smu.edu/hum\\_sci\\_earthsciences\\_etds](https://scholar.smu.edu/hum_sci_earthsciences_etds)



Part of the [Geochemistry Commons](#), and the [Geology Commons](#)

---

## Recommended Citation

WRIGHT, JORDAN, "THE GEOLOGY AND GEOCHEMISTRY OF THE WESTERN IRON ORE GROUP GREENSTONE BELT, SINGHBHUM CRATON, EASTERN INDIA" (2024). *Earth Sciences Theses and Dissertations*. 34.

[https://scholar.smu.edu/hum\\_sci\\_earthsciences\\_etds/34](https://scholar.smu.edu/hum_sci_earthsciences_etds/34)

This Dissertation is brought to you for free and open access by the Earth Sciences at SMU Scholar. It has been accepted for inclusion in Earth Sciences Theses and Dissertations by an authorized administrator of SMU Scholar. For more information, please visit <http://digitalrepository.smu.edu>.

THE GEOLOGY AND GEOCHEMISTRY OF THE WESTERN IRON ORE GROUP  
GREENSTONE BELT, SINGHBHUM CRATON, EASTERN INDIA

Approved by:

---

Robert T. Gregory, Ph.D.,  
Professor of Geology

---

Andrew N. Quicksall, Ph.D.,  
Professor of Environmental Engineering

---

Beatrice M. Magnani, Ph.D.,  
Professor of Geophysics

---

Crayton J. Yapp, Ph.D.,  
Professor of Geology

---

Neil J. Tabor, Ph.D.,  
Professor of Geology

THE GEOLOGY AND GEOCHEMISTRY OF THE WESTERN IRON ORE GROUP  
GREENSTONE BELT, SINGHBHUM CRATON, EASTERN INDIA

A Dissertation Presented to the Graduate Faculty of the

Dedman College

Southern Methodist University

in

Partial Fulfillment of the Requirements

For the Degree of

Doctor of Philosophy

with a

Major in Geology

By

Jordan K. Wright

B.Sc., Geology, University of Texas at Arlington  
M.Sc., Geology, University of Texas at Arlington

May 11, 2024

Copyright (2024)

Jordan K. Wright

All Rights Reserved

Wright, Jordan K.

B.Sc., Geology, University of Texas at Arlington  
M. Sc., Geology, University of Texas at Arlington

The Geology and Geochemistry of the Western Iron Ore Group  
Greenstone Belt, Singhbhum Craton, Eastern India

Advisor: Professor Robert T. Gregory

Doctor of Philosophy conferred May 11, 2024

Dissertation completed April 24, 2024

This thesis presents new data on the origin of the Western Iron Ore Group (W-IOG), a Paleoproterozoic succession deposited on sialic rocks of the Singhbhum Craton. U-Pb ages from zircons from a tuff overlying the Lower Shales just below a banded iron formation (BIF) pin the age of the section to 3.39 Ga. Unconformably overlying the whole IOG section is the Darjiling Group, which contains the Birtola Sandstone (on the basis of this work, now estimated to be 2.35 Ga). The lack of penetrative deformation and low-grade metamorphism makes these rocks excellent subjects for combined radiogenic and stable isotope studies. Data on the W-IOG constrain the development of earth systems operating during the Archean into the Proterozoic (4.0-2.4 Gyr).  $^{143}\text{Nd}/^{144}\text{Nd}$  isotopes for basal Lower Lava greenstones suggest a whole-rock isochron with an apparent age of  $3.42 \pm 0.14$  Ga exhibiting perhaps the highest positive initial  $\epsilon_{\text{Nd}}$  ( $\epsilon_{\text{Nd}} = +5.7 \pm 2.5$ ) observed thus far for an Archean greenstone, and suggesting it is a possible remnant of early Earth differentiation. The initial  $\epsilon_{\text{Nd}}$  of 2.7 at 2.65 Ga for the Upper Lava (i.e., 3  $\epsilon_{\text{Nd}}$  units lower than the greenstones of the Lower Lava) might reflect the cumulative effect of recycling of less Light Rare Earth Element (LREE) depleted sediments into the mantle by subduction processes. The Lower Lava and the Lower Shale plot on a common whole-rock  $^{143}\text{Nd}/^{144}\text{Nd}$  versus  $^{147}\text{Sm}/^{144}\text{Nd}$  line. When combined with REE data, this indicates

that the provenance for the Lower Shale is from mafic rocks similar to the underlying Lower Lava, perhaps a subaerial constructional pile of mafic rocks (i.e., the Lower Lava). Lower Shale rocks are rich in iron (avg. 18 Fe<sub>2</sub>O<sub>3</sub> wt.%,  $n = 7$ ) and with diachronous sedimentation could be the proto-ore for the BIF. The spread in iron isotope ratios ( $-0.693 \leq \delta^{56}\text{Fe} \leq 1.735 \text{ ‰}$ ) suggests the oxidation of iron may have been biologically mediated 3.4 billion-years ago. The Upper Shales share a common line with Singhbhum's granitic basement (with an apparent age of  $3.36 \pm 0.09$ ), implying that these iron-poor shales formed primarily from the unroofing of subvolcanic granitic basement. New zircon U-Pb, Lu/Hf and <sup>18</sup>O/<sup>16</sup>O along with the  $\delta^{18}\text{O}$  of host rock sandstones of the Birtola Formation demonstrates that mantle-like zircon  $\delta^{18}\text{O}$  values are consistent with source regions that have been affected by the addition of subducted recycled crustal Hf. If so, the additions would have been in proportions implying significant refertilization of the MASH source regions that are the presumed igneous source for the Birtola Sandstone. Using the  $\Delta^{18}\text{O}$  quartz-zircon, forward modelling of the  $\delta^{18}\text{O}$  values of the quartz from the zircons and zircons from the quartz distributions are consistent with temperatures of silicic extrusive rock magmatic temperatures. Some low <sup>18</sup>O Archean zircons ( $\delta^{18}\text{O} < -5$ ) in the Birtola, coupled with their appearance elsewhere in, and the high <sup>18</sup>O of the IOG greenstone succession requires surface temperatures more consistent with the faint early Sun. The climate implications and the evidence of recycling down into the mantle all suggest plate tectonics in the early Earth.

## ACKNOWLEDGMENTS

My wife, Emily, initially encouraged me to pursue a Ph.D. and has patiently sacrificed a great deal over the past five years to enable this accomplishment. I thank Bob Gregory for inviting me to pursue a PhD at SMU. I thank Asish R. Basu for serving as an informal Ph.D. advisor over the years. I thank chairman Heather De Shon for persistently supporting me. I am appreciative of Niel Tabor, Beatrice Magnani, Andrew Quicksall, and Crayton Yapp for serving as committee members and for allowing my dissertation to reflect my own interpretations of the data, some of which are still under revision. Chapter 2 was published in *Geology* (2024) and chapter 3 is currently in review.

I am extremely grateful to Ian Richards and John Robbins for their assistance in the lab, as well as their interest and support. I want to thank Mouhcine Gannoun at CNRS for Nd and Fe isotope analysis as well as Trevor Ireland and Bin Fu at ANU for their assistance in the zircon SHRIMP analysis in this dissertation. I thank Yogmaya Shukla for providing and collecting the stromatolites and black chert samples. I thank Nilotpal Ghosh for assisting with major element analysis. Finally, I would like to thank Stephanie Schwob for making every year run as smoothly as possible, and to the Roy M. Huffington Department for annual financial support. Financial support for this thesis came from the Roy M. Huffington account, the SMU Stable Isotope Laboratory, the Clifford Matthews chair account, the American Federation of Mineralogical Societies, the Society of Independent Professional Earth Scientist, and personal finances from myself.

# TABLE OF CONTENTS

LIST OF FIGURES.....	ix
LIST OF TABLES.....	xi
CHAPTER 1: INTRODUCTION.....	1
1.1 Overview.....	1
1.2 Chapter 2: Vestiges of Earth’s earliest depleted mantle reservoir.....	8
1.3 Chapter 3: Relationship between flood basalts and large banded iron formation 3.4 Ga ago.....	8
1.4 Chapter 4: Wilson cycle timescales and cool climate conditions inferred from sandstones along the Archean-Proterozoic Boundary.....	8
1.5 Other work:.....	8
CHAPTER 2: .....	9
2.1 Abstract.....	9
2.2 Introduction.....	10
2.3 Materials and Methods.....	14
2.4 Results.....	21
2.5 Discussion.....	29
2.6 Conclusions.....	32
CHAPTER 3: .....	33
3.1 Abstract.....	33
3.2 Introduction.....	33
3.3 Materials and Methods.....	36

3.4 Results.....	40
3.5 Discussion.....	48
3.6 Conclusions.....	51
CHAPTER 4: .....	60
4.1 Abstract.....	60
4.2 Introduction.....	62
4.3 Geologic Setting.....	64
4.4 Materials and Methods.....	65
4.5 Results.....	72
4.6 Discussion.....	84
4.7 Conclusions.....	93
CHAPTER 5: CONCLUSIONS.....	95
APPENDICES.....	98
A. References corresponding to Figure 22A.....	99
REFERENCES.....	100

## LIST OF FIGURES

<b>Figure 1</b> The relationship between U-Pb crystallization age and depleted mantle model ages due to mixing via recycling.....	7
<b>Figure 2</b> Geological map of the Singhbhum Craton, Eastern India.....	11
<b>Figure 3</b> Field map of the Western-Iron Ore Group Greenstone Belt.....	12
<b>Figure 4</b> Stratigraphic succession of the Western-Iron Ore Group.....	13
<b>Figure 5</b> Nd-isotope comparison between MC-ICP-MS and TIMS.....	20
<b>Figure 6</b> Whole-rock Sm-Nd isotopic evolution diagrams for both the Western and Eastern limb samples of the W-IOG greenstone units.....	26
<b>Figure 7</b> A precise U-Pb isotopic plot of 22 zircon grains separated from the stratigraphically intermediate tuffaceous layer < 30 cm below the banded iron formation.....	27
<b>Figure 8</b> (A) Nd-isotope evolution diagrams for the Earth and (B) Plot of initial epsilon Hf vs. absolute U-Pb age of magmatic and detrital zircons from Singhbhum Craton based on available data.....	28
<b>Figure 9</b> Stratigraphic succession of the W-OG.....	35
<b>Figure 10</b> Plot of measured $\delta^{56}\text{Fe}$ versus $\delta^{57}\text{Fe}$ values of W-IOG samples .....	38
<b>Figure 11</b> W-IOG shales plotted on a Total Alkali versus Silica (TAS) diagram.....	39
<b>Figure 12</b> Photomicrographs of sedimentary W-IOG rocks .....	41
<b>Figure 13</b> Primitive-mantle normalized incompatible element diagrams for the W-IOG sedimentary units .....	44
<b>Figure 14</b> Isotope evolution diagrams .....	46
<b>Figure 15</b> W-IOG origin model.....	50

<b>Figure 16</b> Birtola stratigraphic column.....	67
<b>Figure 17</b> Photomicrographs of sedimentary Birtola sandstones.....	73
<b>Figure 18</b> Concordia diagram for Birtola sandstone sample PRM.....	75
<b>Figure 19</b> $\delta^{18}\text{O}$ -zircon versus time diagram.....	77
<b>Figure 20</b> $\epsilon_{\text{Hf}}$ zircon evolution diagram.....	79
<b>Figure 21</b> Birtola sandstone age diagram.....	81
<b>Figure 22</b> Zircon Hf and O diagrams for Birtola sandstones.....	83
<b>Figure 23</b> $\delta^{18}\text{O}$ -Sandstone versus time diagram.....	85
<b>Figure 24</b> Antiquity of continents diagram.....	91

## LIST OF TABLES

<b>Table 1</b> Results obtained for reference materials by ID-TIMS and MC-ICP-MS.....	21
<b>Table 2</b> Sm-Nd isotope systematics data measured on the Western Iron Ore Group greenstone lavas, Singhbhum Craton.....	23
<b>Table 3</b> U-Pb geochronology for zircons from a volcanic tuff just below the BIF.....	24
<b>Table 4</b> Major and trace element concentrations of the Iron Ore Group from the Eastern Indian Craton.....	52
<b>Table 5</b> Sm-Nd isotopic data on the W-IOG sedimentary units of the Singhbhum Craton.....	58
<b>Table 6</b> Fe isotopic data on the W-IOG sedimentary units of the Singhbhum Craton.....	59
<b>Table 7</b> Detrital U-Pb zircon geochronology and oxygen isotope compositions for sandstone sample PRM from the Birtola formation.....	70
<b>Table 8</b> Lu-Hf isotope zircon data measured from sample PRM from the Birtola Formation.....	71
<b>Table 9</b> Whole rock oxygen and hydrogen data for the Birtola sandstones.....	72

## CHAPTER 1 INTRODUCTION

### 1.1 Overview

This thesis continues some of the PhD thesis work of Sandeep Banerjee (2010) by extending the previous stable isotope studies to radiogenic isotopes and geochronology along with trace element and major element data on the Iron Ore Group (IOG) of the Singhbhum Craton and from the Birtola Formation part of sediments that non-conformably overlie Archean Singhbhum granites. The samples are part of the rock collection of Asish Basu used in (Basu et al., 2008; Saha et al., 2004) who collaborated with SMU on this study and the previous Banerjee PhD thesis work.

The results of oxygen and hydrogen isotope studies on the IOG greenstone and shales have isotope ratios consistent with alteration of Archean greenstone by fluids similar to the modern ocean. The results are consistent with the buffering of seawater oxygen isotopes by hydrothermal exchange at mid-ocean ridges (Muehlenbach and Clayton, 1976; Gregory and Taylor, 1981; Gregory, 1991; Gregory, 2002). Greenstone pillow lavas with  $^{18}\text{O}$ -enriched relative to mantle-derived basalts are characteristic of plate tectonic regimes; seawater is either its present value or slightly enriched relative to modern seawater. It is not depleted in  $^{18}\text{O}$  as proposed using data of from sedimentary rocks (e.g. Kasting et al., 2006). In Archean greenstone belts the similarity of  $^{18}\text{O}/^{16}\text{O}$  ratios of these rocks is consistent with Phanerozoic seafloor rocks.

If as indicated by stable isotope data on greenstones that plate tectonics were operative in the Archean, then is it possible to detect in trace element and radiogenic isotopes signature evidence of processes consistent with a plate tectonic regime? Additionally, the original work on mantle and crustal reservoirs invoked the chondritic Earth model and gradual growth of

complementary crust and mantle reservoirs. Mass balance calculation suggested that the depleted mantle reservoir down to the 650 km seismic discontinuity was balanced by the continental crustal reservoir. Below the 650 km discontinuity chondritic and unfractionated reservoirs were hypothesized.

A contrarian view (e.g. Armstrong, 1991) that like other solar system terrestrial objects, the Earth differentiated early and that continental crustal volume has remained relatively constant over geologic time. Armstrong (1991) and Gregory (1991) proposed that chemical weathering was a mechanism to recycle continents through subduction of pelagic sediments.

This thesis will test the proposition that the recycling that occurs during subduction affects the source regions of basalts. Hafnium isotopes (sensitive to mantle-crust formation processes) of detrital zircons that can be dated using concordant U-Pb ages to establish evolutionary patterns. Zircons which are resistant to post-crystallization oxygen isotope exchange represent the isotopic composition of the source rocks at the time of partial melting. “Normal” mantle oxygen isotope values are consistent with silicic rocks formed without influence of surface-derived oxygen isotopes. However, surface derived trace elements with higher concentrations introduced by subduction processes, exchanging or mixing with mantle wedges, reveal their presence in the low concentration environment of the depleted mantle wedge.

Low  $^{18}\text{O}$  zircons are known to exist (e.g Valley, 2005) and low  $^{18}\text{O}$  silicic magmas are likely result of partial melting of hydrothermally altered basalts (e.g in Iceland, Pope et al 2014). Using the systematics of stable isotopes (Taylor, 1974; Gregory et al. 1989), zircon  $^{18}\text{O}/^{16}\text{O}$  ratios provide a constraint on the oxygen isotope composition of meteoric waters. The isotopic composition of meteoric waters reflects the temperature distribution in the atmosphere and hence is a proxy for paleoclimate,

## Radiogenic Isotopes

The isochron method plots the measured daughter product ratio (Y) against the measured parent/daughter ratio (X). If the samples followed the conditions for an age: 1) homogenous daughter isotope ratios at  $t=0$ ; 2) parent/daughter ratios equilibrated according to chemical fractionation from a common reservoir, 3) the system is closed once formed, and 4) mass is conserved (i.e. the system remains closed) except for each decay of a parent atom, one daughter atom is created, then each measured pair satisfies the equation:

$$\text{Eq.1} \quad D_{\text{measured}} = D_{\text{initial}} + P_{\text{measured}}(e^{\lambda t} - 1)$$

There are two unknowns: the initial daughter ratio and the age itself. By assuming an initial daughter ratio, the calculated  $t$  is called model age.

By measuring more than three pairs, the plotted pairs will map out a line called the isochron where the  $X=0$  intercept is the inferred  $D_{\text{initial}}$  and the slope of the line is:

$$\text{Eq.2} \quad (e^{\lambda t} - 1)$$

The calculated age is therefore:

$$\text{Eq.3} \quad t = \frac{\ln(1 + (e^{\lambda t} - 1))}{\lambda}$$

In words, this real age is the natural log of (1+slope of the line ) divided by the decay constant with assumptions 1-3 satisfied. Real ages are the gold standard of geochronology.

Using the two measured parameters, equation 1 generates an apparent initial daughter ratio as a function of  $t$ ; this is called an evolution curve. Samples that lie on isochrons all intersect at the same inferred initial at the same time. Any two points on a multiple point isochron are a solution to the two equations and two unknowns represented by equation 1.

At each time in an evolution diagram, the isotope ratios can be transformed in epsilon values by the time integrated LREE -depleted samples (generally more mafic rocks) become more positive with time and LREE-enriched rocks (generally more felsic rocks) become more negative with time. Mantle or chondrite separation ages, the intersection of the evolution curves for measured samples with an evolutionary curve for either the depleted mantle or chondrites.

Figure 1 illustrates how (A) a mantle derived mafic source will have a U-Pb crystallization (e.g., 3.0 Ga) age identical to its depleted mantle model age ( $T_{DM}$ ). Figure 1B shows how this 3.0 Ga source can become reworked during a younger 2.8 Ga juvenile magmatic event, imparting an older  $T_{DM}$  age (e.g., 2.9 Ga) over a younger U-Pb crystallization age. The initial age and initial  $\epsilon_{Hf}$  of the source prior to mixing can be determined based on the samples that fall on a common evolutionary line that projects back to the same  $T_{DM}$ . In such a case for LREE enriched rocks, the samples will exhibit increasingly negative initial  $\epsilon_{Hf}$  values due to the radiogenic ingrowth of Hf. The crustal residence age,  $\Delta t$ , is a proxy for the timescale of mixing via recycling and can be calculated by  $T_{DM} - T_{U-Pb}$ .

## Stable Isotopes

The basis for light stable isotope (HCNOS) geochemistry is the exchange reaction. Using zircon quartz as an example:



The equilibrium constant for this reaction is:

Eq. 5

$$K = \left( \frac{^{18}\text{O}/^{16}\text{O}_{\text{quartz}}}{^{18}\text{O}/^{16}\text{O}_{\text{zircon}}} \right)^4$$

In this case the fractionation factor  $\alpha$  is defined as  $K^{1/4}$ . The temperature dependence of this fractionation is given by:

Eq. 6

$$1000 \ln \alpha \approx \delta^{18}\text{O}_{\text{quartz}} - \delta^{18}\text{O}_{\text{zircon}} \equiv \Delta^{18}\text{O} \text{ (T)}$$

Big delta,  $\Delta$ , is called the fractionation, the small case deltas,  $\delta$ , facilitate measurements with respect to isotope standards,  $\delta \equiv [R_{\text{sample}}/R_{\text{standard}} - 1] 1000$ , where the R's reflect the stable isotope ratios of interest in the HCNOS system or any other stable isotope system (e.g. Fe later in this thesis).

In the case of quartz-zircon pairs, the temperature dependence (Trail et al.2009, Geochimica) of the fractionation is:

Eq. 7

$$\Delta^{18}\text{O}_{\text{quartz-zircon}} = \frac{(2.33 \pm 0.24) \times 10^6}{T^2}$$

In a sedimentary rock with two mineral mechanical mixtures, the forward model distribution of one of the minerals using the fractionation factor and the measured isotope ratios of the other allow to test whether they come from similar sources. Zircons are resistant to subsolidus isotope exchange commonly found in more silicic igneous rocks. Are the quartz oxygen isotope values consistent with origin from similar magmas to those of the zircons over a reasonable magmatic temperature range?

Surface waters on the Earth are controlled by oxygen isotopic composition of the oceans, buffered by processes at mid-ocean ridges and atmospheric processes. The relationship between

the D/H and  $^{18}\text{O}/^{16}\text{O}$  ratios of meteoric waters (Craig, 1961) is fundamental to paleoclimatology studies.

Eq. 8 
$$\delta\text{D} \approx 8 \delta^{18}\text{O} + 10$$

If a basaltic rock suffers subsolidus hydrothermal exchange Taylor's (1974) water/rock equation can be used to estimate the end member fluid necessary to cause the altered signature.

Eq. 9 
$$\frac{W}{R} = \frac{\delta_{final} - \delta_{initial}}{\delta W_{initial} - (\delta_{final} - \Delta_{rock-water})}$$

Where the  $\delta$ 's initial and final refer to the rocks with +6 for the initial rock in a basaltic system,  $\delta W$  referring to external fluid seawater or meteoric water. For basalt-water at the temperatures of interest (Bowers and Taylor, 1985) the  $\Delta$  is approximately 6. On a molar basis from conservation of energy, water/rock ratios of 1 are typical for volcanic piles of basalt (e.g. Gregory et al. 1989) For the Iceland low  $^{18}\text{O}$  zircons plotted later in this thesis, a meteoric water of -14 predicts the +2 per mil values for zircons from Iceland volcanic rocks.

Using International Atomic Energy Agency data, Ferguson et al. (1991), proposed the following relations between surface Mean Annual Temperatures (MAT) and meteoric water compositions:

$$T \approx 1.58 \delta^{18}\text{O} + 21.8 \text{ (maritime)} \text{ and } T = 1.05 \delta^{18}\text{O} + 18.1 \text{ (continental)} \text{ where } T \text{ is in } ^\circ\text{C}.$$

The isotopic composition of meteoric waters reflects the temperature distribution in the atmosphere and hence is a proxy for paleoclimate.

Low  $^{18}\text{O}$  zircons are known to exist (e.g., Valley, 2005), and low  $^{18}\text{O}$  silicic magmas are likely result of partial melting of hydrothermally altered basalts (e.g., in Iceland, Hatori and

Muehlenbachs, 1982; Pope et al., 2014). Using the systematics of stable isotopes (Taylor, 1974; Gregory et al. 1989), during subsolidus hydrothermal exchange, igneous zircon  $^{18}\text{O}/^{16}\text{O}$  ratios who sample the partial melts of altered rocks provide a constraint on the oxygen isotope composition of ancient surface meteoric waters. This may be particularly important for the early Earth as many sedimentary rocks do not preserve primary depositional isotope ratios (e.g., Gregory et al 1989).

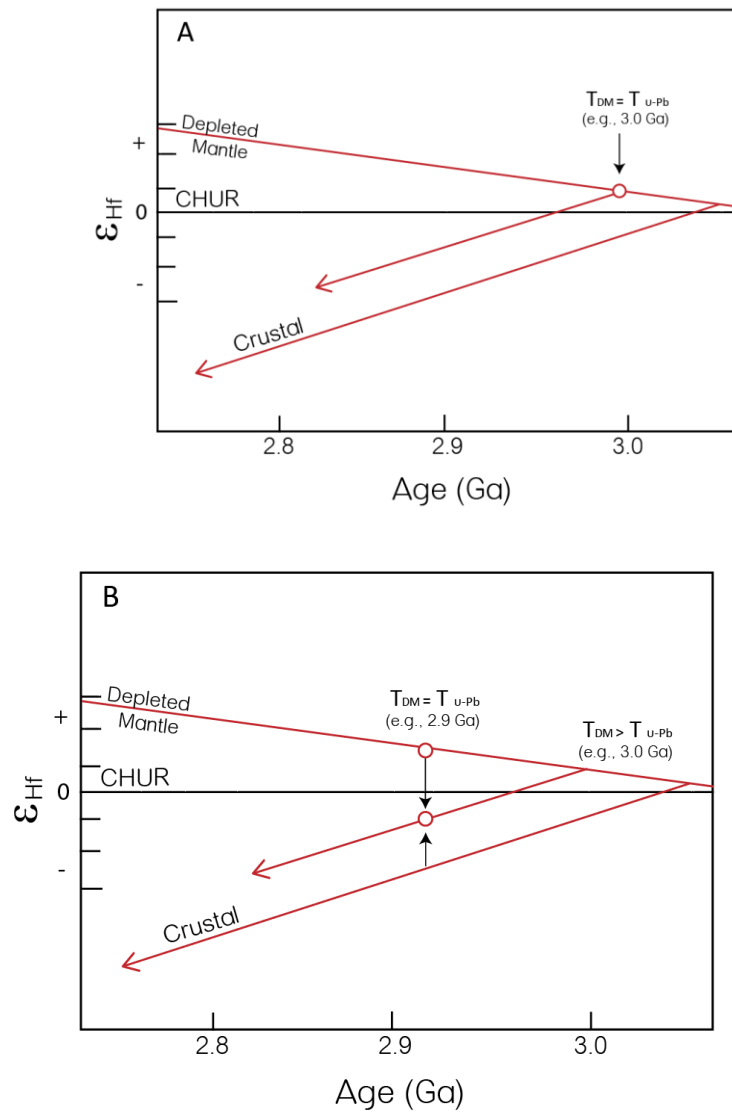


**Figure 1.** The relationship between U-Pb crystallization age and depleted mantle model ages due to mixing via recycling.

## **1.1 Chapter 2: Vestiges of Earth's earliest depleted mantle reservoir**

Chapter 2 presents Nd data for two temporally distinct but spatially equivalent greenstone units. This paper discusses the evidence for the survival of Earth's primary depleted mantle that formed during its initial planetary differentiation event, as well as the destruction and recycling of its complementary crust. This study was recently published: Jordan K. Wright, Asish R. Basu; Vestiges of Earth's earliest depleted mantle reservoir. *Geology* 2024; doi: <https://doi.org/10.1130/G51936.1>

## **1.2 Chapter 3: Relationship between flood basalts and large banded iron formation 3.4 Ga ago**

Chapter 3 presents Nd isotope, Major, and Trace element data on all the W-IOG sedimentary units, as well as Fe isotopes on the Lower Shale, BIF, Black Chert, and Stromatolites. This paper provides insight into the provenance of all the W-IOG sedimentary units, including the world's largest Paleoarchean BIF.

## **1.3 Chapter 4: Wilson cycle timescales and cool climate conditions inferred from sandstones along the Archean-Proterozoic time boundary.**

Chapter 4 reports U-Pb, Hf, and oxygen isotopic data from zircons as well as oxygen and hydrogen isotope data from detrital quartz for the Birtola sandstones from the Singhbhum craton. This paper provides insight into provenance, as well as potentially contemporary paleotectonics and paleoclimate.

## **1.4 Other work**

The appendices provide supplementary references corresponding to figure 22A.

## CHAPTER 2

### VESTIGES OF EARTH'S EARLIEST DEPLETED MANTLE RESERVIOR

#### 2.1 Abstract

There is a paucity of evidence preserved in the rock record regarding the Earth's earliest enriched crust and its complementary depleted mantle during the Hadean. In recent years, vestiges for these early reservoirs have been inferred by examining Hf isotope systematics compiled from zircons. The Singhbhum Craton of Eastern India, for example, preserves only the existence of an enriched ( $\epsilon_{\text{Hf}} < 0$ ) crustal reservoir during the Hadean-Eoarchean, with the notable absence of a depleted mantle reservoir signature ( $\epsilon_{\text{Hf}} > 0$ ) until  $\sim 3.5$  Ga. Here we report a new Sm-Nd isochron for the Lower Lava greenstones of the Western-Iron Ore Group (W-IOG) from the Singhbhum craton, confirming a  $3.42 \pm 0.14$ -billion-year-old crystallization age with an initial  $\epsilon_{\text{Nd}} = +5.7 \pm 2.5$ . This is the highest positive  $\epsilon_{\text{Nd}}$  value derived from an isochron of this age. We infer that this depleted mantle source is a vestige complementary to the primary crust following planetary differentiation. Furthermore, we present U-Pb zircon ages for a  $3.39 \pm 0.02$  Ga tuff which lies stratigraphically above the Lower Lava and less than 30 cm below an extensive conformable Banded Iron Formation (BIF). This age implies that the W-IOG's BIF is the largest economic grade iron formation for its Paleoproterozoic age, suggesting that free atmospheric oxygen existed as more than just whiffs at this time.

## 2.2 Introduction

While there is evidence to suggest that Earth differentiated into an enriched crust and a depleted mantle reservoir early in its history (>4.5 Ga, e.g., Harper and Jacobsen, 1992), the fate of these complementary reservoirs and the role they have played in the evolution of Earth systems remains a subject of great interest. Over the decades, several studies have reported  $^{142}\text{Nd}$  anomalies, with some authors proposing the earliest enriched crust became reworked to form cratons (O'Neil and Carlson, 2017) while also possibly remaining stored at the base of the lower mantle (Carlson and Boyet, 2008). However, although  $^{143}\text{Nd}$  systematics provides traces for an extremely depleted mantle reservoir in the Archean (Collerson et al., 1991), there are few proposals for the potential survival of a >4.5 Ga depleted mantle source (e.g., Jackson et al., 2010; Caro and Bourdon, 2010). The inaccessibility of Earth's earliest depleted mantle, the lack of well-preserved mantle-derived Archean rocks, and overprinting by continuous surface recycling have all contributed to our limited understanding of these ancient reservoirs (e.g., Armstrong, 1991), although, recently, the most ancient accessible reservoirs of Earth's mantle have been implicated from studies in basalts of the Baffin Island and West Greenland (see, Caro and Bourdon, 2010; Jackson et al., 2010).

The purpose of this study is to apply the  $^{147}\text{Sm}$ - $^{143}\text{Nd}$  isotopic system (based on the long-lived decay of  $^{147}\text{Sm}$  to  $^{143}\text{Nd}$ ,  $\lambda_{\text{Sm}} = 6.54 \times 10^{-12} \text{yr}^{-1}$ ) on well-preserved greenstones from the W-IOG greenstone belt, in order to establish their age as well as to evaluate the significance of their initial  $^{143}\text{Nd}/^{144}\text{Nd}$  ratios with respect to the evolution of the depleted mantle. Located in the Singhbhum craton, Eastern India, the W-IOG is part of a regional (55 x 35 km) NNE plunging asymmetric synclinorium structure in the Jambha-Koira Valley (Fig. 2, 3). Greenstones make up two significant lithologies within the W-IOG stratigraphy, with the lowermost stratum

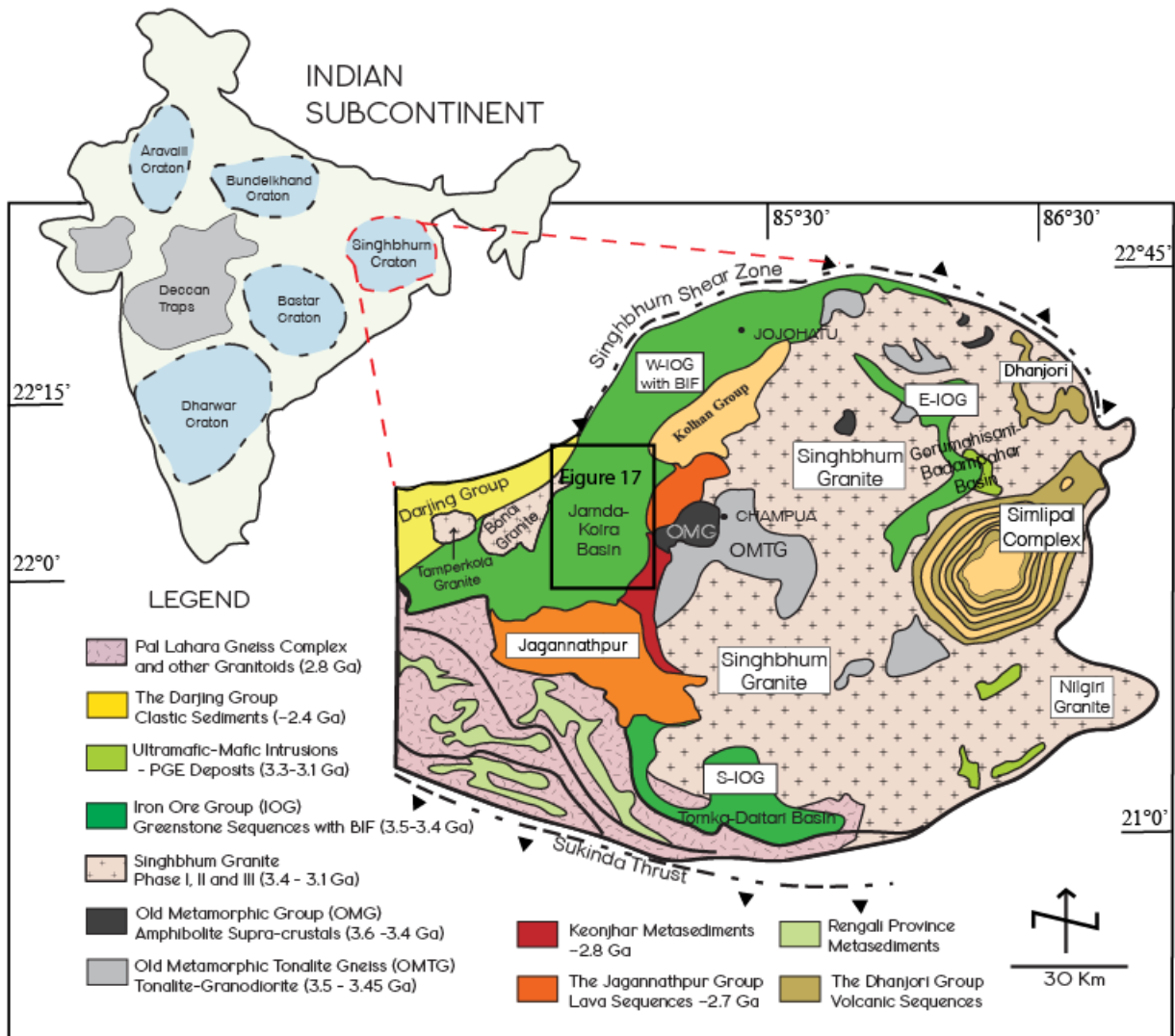


**Figure 2. Geological map of the Singhbhum craton, Eastern India.** The Western-Iron Ore Group (W-IOG) is situated along the margin of the craton. The samples for this study were collected within the parameters of the black square of the Jambda-Koira Basin. Modified after (Saha, 1994; Dunn, 1929, 1940).

designated as the “Lower Lava” and the uppermost stratum “Upper Lava” (Fig. 4). Together, these

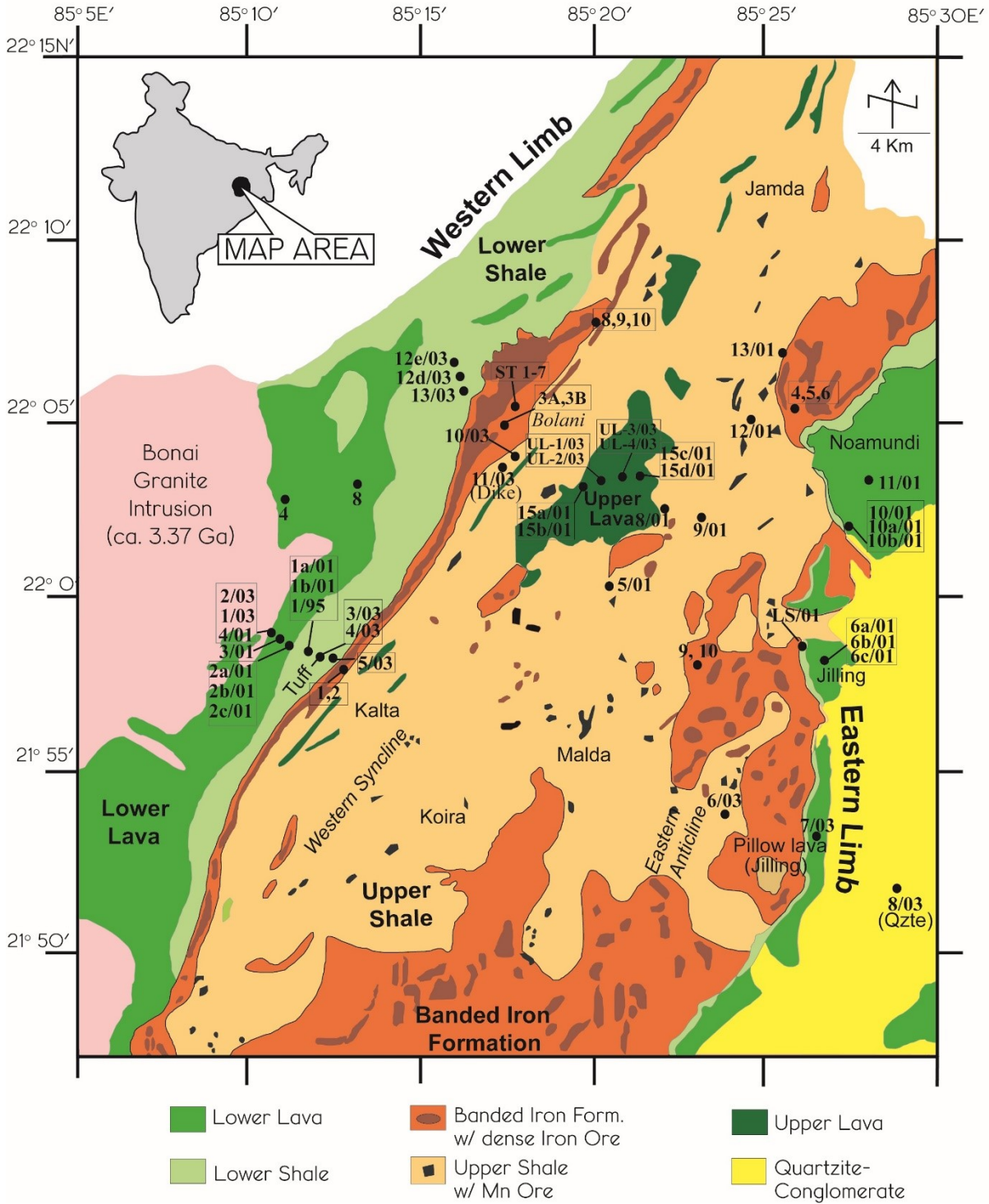


**Figure 3. Geological map of the Western Iron Ore Group greenstone belt.** Samples analyzed for this study were collected from the Noamundi-Jamda-Koira type area from both the Eastern and Western limbs. Sample numbers are marked by darkened filled circles. Modified after (Dunn, 1940).

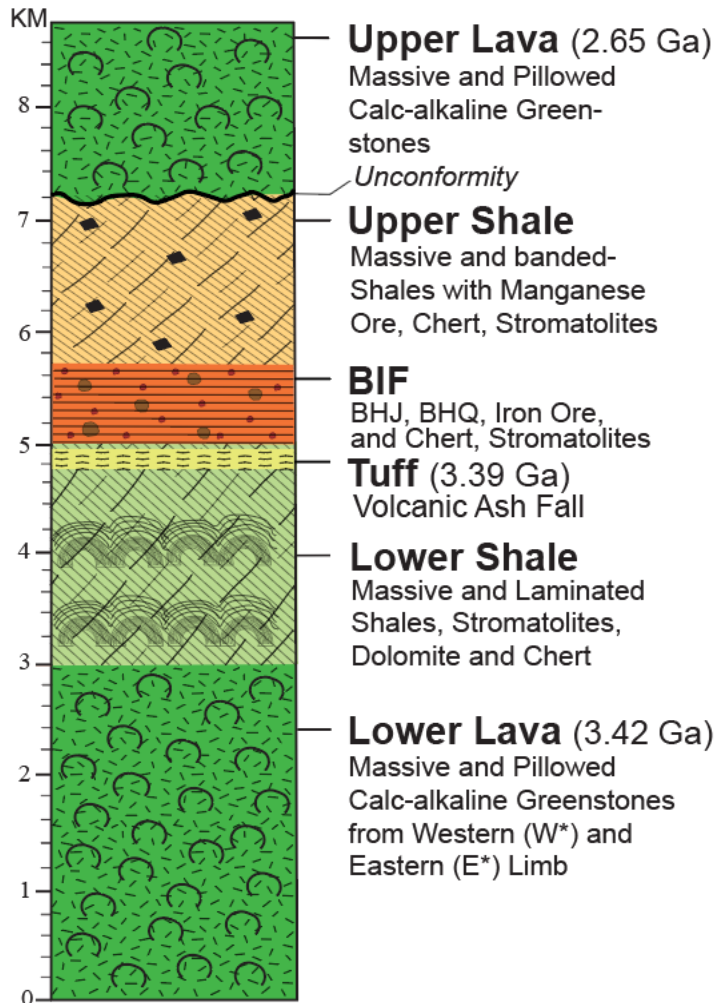


**Figure 4. Stratigraphic succession of the Western Iron Ore Group (W-IOG).** The greenstones measured for this study were collected from the lowermost unit named the ‘Lower Lava’ and from the uppermost unit ‘Upper Lava’. This study has dated, using Sm-Nd isotope systematics, the Lower Lava to be 3.42 Ga and the Upper Lava to 2.65 Ga. We have also dated the tuffaceous horizon intermediate within the column using U-Pb zircon geochronology to be ~3.4 Ga. Note that the thickness of the tuffaceous unit is exaggerated. Modified after Mukhopadhyay, 1988.

greenstones encompass an apparent 8 km thick volcano-sedimentary and economic-grade banded-iron formation bearing greenstone belt succession (e.g., Basu et al., 2008). Samples were collected from both the Eastern and Western Limb of the Lower Lava W-IOG synclinorium as well as the overlying Upper Lava deposited on an unconformity (Fig. 3, 4). All the W-IOG greenstones are characterized by their low-grade greenschist facies (quartz + albite + chlorite), primary igneous augite and pigeonite, lack of penetrative deformation, preservation of original volcanic textures (i.e., hydrothermal metamorphism), dominant calc-alkaline affinities with subordinate tholeiite, massive-pillowed morphologies, and average basaltic-andesite composition.

Here we report the W-IOG Lower Lava to preserve the most depleted initial  $\epsilon^{143}\text{Nd}$  signature derived from a paleoarchean isochron. We also present new U-Pb zircon geochronology for a stratigraphically overlying tuff whose age agrees with the Lower Lavas isochron age. Lastly, we examine the significance of the new  $^{143}\text{Nd}$  results presented in this study within the evolutionary context of Singbhum's  $\text{Hf}_{\text{zircon}}$  isotopic record.

## **2.3 Materials and Methods**

### *2.3.1 Sample description and preparation*

The present study involves greenstones collected from the Western-Jamda-Koira district representing samples from the freshest and relatively unweathered outcrops—avoiding domains of deformation and zones of shearing. All samples were carefully cleaned with 18.2 M $\Omega$  ultrapure water and dried prior to pulverization. Large whole-rock samples were selected and homogenized into a fine powder in a steel jaw crusher. Previous sample powder adhering to the surface of the grinding and splitting equipment were removed through treatment with detergent, 18.2 M $\Omega$

ultrapure water, and followed by a 30-minute grinding cycle of high purity quartz sand and ending with a 30-minute ultrasonic bath in 18.2 M $\Omega$  ultrapure water to remove any embedded material. This regimen of precaution was exercised between sample use to prevent cross-contamination.

### *2.3.2 Trace element procedure*

Trace element concentrations were determined using an Inductively Coupled Plasma Mass Spectrometer (ICP-MS) (Thermo elemental X-7) at the University of Rochester, NY. For ICP-MS analysis, 25-50 mg of homogenized whole-rock sample powder were treated with trace element grade HNO<sub>3</sub> and HF acid mixtures and digested and diluted to 100 mL in 2% HNO<sub>3</sub> solution and spiked with ~10 ppb internal standards of In, Cs, Re and Bi. The elemental concentrations for these samples were analyzed using known concentrations from the external standards BIR-2 and BCR-2. Repeated measurements of AGV-2 and BHVO-2 standards were run as unknowns to estimate the concentrations of various elements within less than 5% error. Whereas, the rare earth elements, particularly Sm and Nd, were more precisely determined within less than 2% error, respectfully.

### *2.3.3 U-Pb geochronology*

22 zircon grains (~350 $\mu$ m long) were separated from a tuffaceous layer < 1m below the banded iron formation. Epoxy grain mount of hand-selected zircons are polished to expose grain interiors. After ultrasonic cleaning and drying down, samples are coated with about 10 nm of Au. U-Pb ages are obtained by the UCLA CAMECA IMS 1270 ion microprobe using a 15-nA <sup>16</sup>O-primary beam focused on a 25  $\mu$ m diameter spot. Secondary ions are extracted at 10kV, and the mass spectrometer is tuned to a mass resolution of ~5000 to resolve molecular interferences in the mass range

analyzed ( $^{94}\text{Zr}_2\text{O}^+$ ,  $^{204}\text{Pb}^+$ ,  $^{206}\text{Pb}^+$ ,  $^{207}\text{Pb}^+$ ,  $^{232}\text{Th}^+$ ,  $^{238}\text{U}^+$ ,  $^{238}\text{U}^{16}\text{O}^+$ ). The sample analysis surface is flooded with oxygen gas at a pressure of  $4 \times 10^{-3}$  Pa to increase the Pb yields by a factor of 2. The relative sensitivities of Pb and U were determined on 9 reference zircons for AS-3 (Paces and Miller, 1993) with an average concordant  $^{207}\text{Pb}/^{206}\text{Pb}$  age ( $1099 \pm 1$  Ma) that agrees with the accepted standard value ( $1099 \pm 1.2$  Ma; Paces and Miller, 1993) using a calibration technique similar to Compston et al., 1984. Th/U ratios are obtained by multiplying measured  $^{232}\text{Th}^+/^{238}\text{U}^+$  with relative sensitivity value determined on reference zircon 91500. Data were plotted using ISOPLOT (see, Vermeesch, 2018).

#### *2.3.4 Sm-Nd isotope analytical procedure*

Sm-Nd isotope systematics were analyzed at CNRS, Laboratoire Magmas et Volcans, UMR 6524, Clermont Auvergne University, France. Chemical handling was carried out under a class 10 vertical laminar flow hoods in a laboratory with an overpressure of filtered air, at a temperature of  $20^\circ\text{C}$ . All water used was purified to a resistivity of 18.2 M $\Omega$  cm. About 100-200 mg weighted powders were digested overnight (12 hours) in a closed Teflon vessel within a solution of 1 mL of 14 N  $\text{HNO}_3$  and 2 mL of 29 N HF at  $70^\circ\text{C}$ . The solution is then evaporated to dryness with volatilization of fluorides by increasing the hotplate temperature to  $100^\circ\text{C}$  for 48 hours. After evaporation, the decomposition of sparingly soluble fluorides that might sequester REEs was accomplished by adding 0.1 mL of 6 N  $\text{HClO}_4$  and heating on the hotplate up to  $170^\circ\text{C}$ . Following evaporation, the sample is taken up with 1 mL of 14 N  $\text{HNO}_3$ , kept overnight at mild temperatures and then evaporated dryness. The residue is dissolved in 5 mL of 7 N HCl, kept overnight on the hotplate at  $70^\circ\text{C}$  to convert the nitrates into chlorides and then evaporated to dryness. The sample salts were taken up in 10 mL of 1 N  $\text{HNO}_3$  and kept at  $50^\circ\text{C}$  for 3-4

hours. The resulting solutions were then transferred to a centrifuge tube and processed for 20 minutes at 4000 rpm to isolate any insoluble residue, which, if present, were treated in high-pressure Teflon bombs to achieve complete dissolution.

The cation-exchange and extraction chromatographic methods are described in detail by Sanchez-Lorda et al., (Sanchez-Lorda et al., 2013), and was followed similarly for the samples in this study. Prior to the MC-ICPMS analysis, a solution was obtained containing Sm- and Nd present in the samples without the mutual fractionation of these elements. It was necessary to get rid of matrix elements, for these purposes, the samples were processed through two separation steps based on cation-exchange and extraction chromatography, respectively, as described in (Pin et al., 2014).

The first separation step uses silica glass columns (Height = 8 cm, internal diameter = 0.7 cm), a polyethylene frit at the bottom, and are loaded with 2 mL of Dowex AG50W X4 200-400 mesh resin in an H<sub>2</sub>O medium. The second separation step uses 3.5 cm in height columns containing 83 mg of the TRU extraction chromatography material. The columns were calibrated with solutions of rock standards to check for adequate recovery of Sm-Nd, by semi quantitative measurement of the elements of interest using a quadrupole ICP-MS instrument (Thermo XSeries II). The purpose of the first column is to eliminate all major elements, especially Fe<sup>3+</sup>, which competes with the LREEs for extraction by the TRU resin. Once the solution containing the LREE fraction is collected from the first separation step, the sample solution is evaporated to dryness. The sample is then loaded and passed through the second separation step to obtain a solution purified from essentially all other elements. This chemical procedure does not fractionate Sm from Nd appreciably. This chemistry achieves consistent quantitative yields of at least 97%. Total

procedural blanks, including sample dissolution and element separation, were <1 ng for Sm and Nd.

The concomitant determination of  $^{143}\text{Nd}/^{144}\text{Nd}$  and  $^{147}\text{Sm}/^{144}\text{Nd}$  ratios in the samples from this study have been achieved with a good precision and accuracy (reproducibility of  $^{147}\text{Sm}/^{144}\text{Nd}$  typically 0.2% RSD) by using a ThermoFisher Scientific's MC-ICPMS Neptune Plus (Multiple Collector – Inductively Coupled Plasma -Mass Spectrometry), without resorting to the isotope dilution method. Both ratios were measured simultaneously on a single solution of LREE separated from matrix elements by combined cation exchange and extraction chromatography following the chemical procedures described by Pin et al., 2014. The method requires sample introduction using a 2-step aerosol desolvation device reducing oxide/metal ratios to less than 0.02%, thereby reducing to negligible levels the difference in oxide formation which is a major cause of inter-element Sm/Nd fractionation in the ICP. For unknown samples, the instrumental fractionation of the Sm/Nd ratio, which might arise from the minor differences in the ionization efficiencies of these elements, were corrected by quantifying this effect in known samples such as mixed synthetic solutions of a high purity Nd and Sm metals provided by the Ames (Iowa) Laboratory as well as rock standards using a bracketing technique. Such fractionation was found to be negligible.

This procedure involves the simultaneous measurement of signals at mass 143, 144, 145, 146, 147, and 149, respectively for about 12 minutes. Then the direct determination of the  $^{143}\text{Nd}/^{144}\text{Nd}$  and  $^{147}\text{Sm}/^{144}\text{Nd}$  were achieved, with correction of the isobaric interference of  $^{144}\text{Sm}$  on  $^{144}\text{Nd}$  by standard stripping procedures, while accounting for the independent instrumental mass bias by normalization to  $^{146}\text{Nd}/^{144}\text{Nd} = 0.7219$ . The  $^{143}\text{Nd}/^{144}\text{Nd}$  were compared with repeat analysis of the Sm-free JNdi-1 solution as reference. The mean of 25 measurements on the pure JNdi-1 standard during this study was 0.512101 (2SD = 0.000009), slightly lower than the recommended value of

512115 ± 22 (Tanaka et al., 2000). This method outlined by Sanchez-Lorda et al., 2013 illustrates that the  $^{143}\text{Nd}/^{144}\text{Nd}$  and  $^{147}\text{Sm}/^{144}\text{Nd}$  ratios measured in various international geologic reference materials show fair reproducibility and accuracy, as illustrated by a comparison with published data obtained by using the conventional ID-TIMS method (see, Fig. 5). It has been observed that, although comparison between the measurements of geologic standards do not produce strictly equivalent values, the differences between the average MC-ICPMS data and the individual ID-TIMS results do not exceed 0.2  $\epsilon_{\text{Nd}}$  units (present-day values) (see, Sanchez-Lorda et al., 2013) (Table 1). Data were plotted using ISOPLOT (see, Vermeesch, 2018). Uncertainties are at the 95% confidence level.  $\sigma$  represents the standard deviation of the mean. Note that the ‘rock-type’ description in Table 2 was determined using a TAS diagram. As reported in Fig. 20, the  $\epsilon_{\text{Nd}}(t)$  value defined as:  $\epsilon_{\text{Nd}}(t) = [({}^{143}\text{Nd}/{}^{144}\text{Nd})_{\text{initial}}^t / ({}^{143}\text{Nd}/{}^{144}\text{Nd})_{\text{CHUR}}^t - 1] \times 10^4$ , where the  $\epsilon_{\text{Nd}}$  represents the deviation of the  $^{143}\text{Nd}/^{144}\text{Nd}$  in parts in  $10^4$  from the CHUR evolution at the time of formation of the greenstones, where  $t = 3.42$  Ga for the Lower Lava and  $t = 2.65$  Ga for the Upper Lava. Present day reference values for CHUR are  $^{143}\text{Nd}/^{144}\text{Nd} = 0.512638$  (Goldstein et al., 1984) and  $^{147}\text{Sm}/^{144}\text{Nd} = 0.1967$  (Jacobsen and Wasserberg, 1984) and the decay constant  $\lambda_{\text{sm}} = 6.54 \times 10^{-12} \text{ yr}^{-1}$  (Lugmair and Marti, 1978). The Enrichment Factor ( $f_{\text{Sm}/\text{Nd}}$ ) calculated as  $[(^{147}\text{Sm}/^{144}\text{Nd})_{\text{sample}} / ({}^{147}\text{Sm}/^{144}\text{Nd})_{\text{CHUR}} - 1]$  where CHUR is chondritic uniform reservoir and  $({}^{147}\text{Sm}/^{144}\text{Nd})_{\text{CHUR}} = 0.1967$ . Calculated using the present-day bulk earth (CHUR) values of  $^{143}\text{Nd}/^{144}\text{Nd} = 0.512638$ . The  $\epsilon_{\text{Nd}}(0)$  value represents the deviation of  $^{143}\text{Nd}/^{144}\text{Nd}$  in parts of  $10^4$  from the present day CHUR value.  $T_{\text{DM}} = 1/\lambda \ln [1 + ((^{143}\text{Nd}/^{144}\text{Nd})_{\text{sample today}} - ({}^{143}\text{Nd}/^{144}\text{Nd})_{\text{depleted mantle today}}) / (({}^{147}\text{Sm}/^{144}\text{Nd})_{\text{sample today}} - ({}^{147}\text{Sm}/^{144}\text{Nd})_{\text{depleted mantle today}})]$ , where the decay constant  $\lambda_{\text{sm}} = 6.54 \times 10^{-12} \text{ yr}^{-1}$  and the DM today values are from this study ( $^{147}\text{Sm}/^{144}\text{Nd} = 0.236$  and  $^{143}\text{Nd}/^{144}\text{Nd} = 0.5138170$ ).

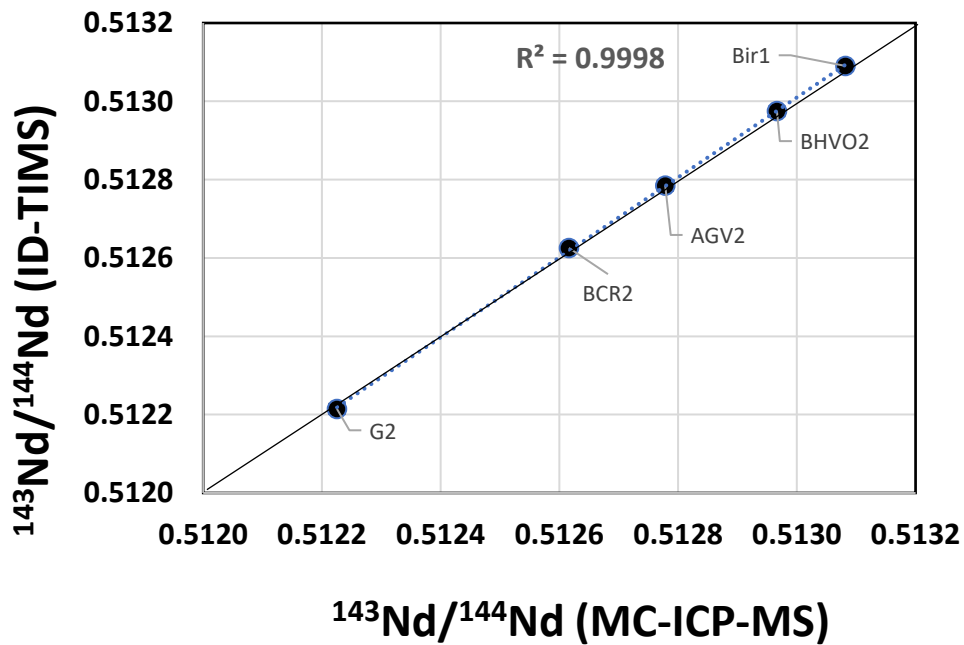
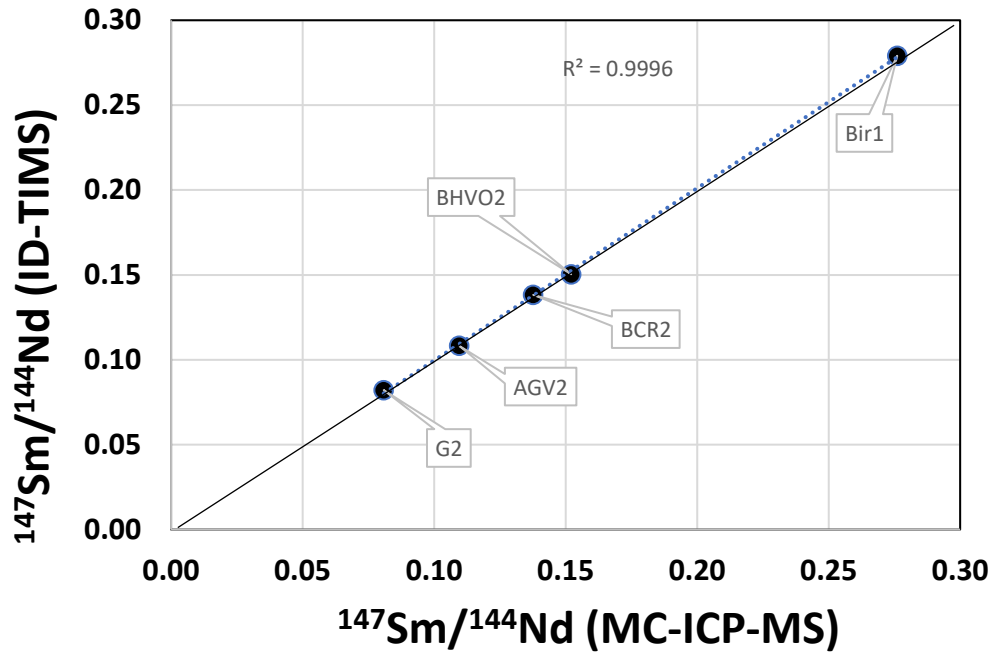


**Figure 5.** (A) Comparison of  $^{147}\text{Sm}/^{144}\text{Nd}$  ratios and (B) comparison of  $^{143}\text{Nd}/^{144}\text{Nd}$  ratios obtained by MC-ICP-MS and ID-TIMS methods for the reference materials in this analytical protocol.

**Table 1**

Results obtained for reference materials by ID-TIMS and MC-ICP-MS methods.

ID-TIMS							
	N	$^{143}\text{Nd}/^{144}\text{Nd}$	2SD	eNd	$^{147}\text{Sm}/^{144}\text{Nd}$	2SD	2SD (%)
<b>Bir1</b>	3	0.513090	0.000009	8.8	0.2791	0.0010	0.4
<b>AGV2</b>	3	0.512784	0.000010	2.9	0.1082	0.0009	0.9
<b>BHVO2</b>	3	0.512975	0.000009	6.6	0.1504	0.0005	0.4
<b>BCR2</b>	4	0.512626	0.000008	-0.2	0.1383	0.0006	0.4
<b>G2</b>	3	0.512215	0.000008	-8.3	0.0821	0.0009	1.1
MC-ICP-MS							
	N	$^{143}\text{Nd}/^{144}\text{Nd}$	2SD	eNd	$^{147}\text{Sm}/^{144}\text{Nd}$	2SD	2SD (%)
<b>Bir1</b>	3	0.513082	0.000012	8.7	0.2761	0.0016	0.6
<b>AGV2</b>	3	0.512778	0.000013	2.7	0.1096	0.0010	0.9
<b>BHVO2</b>	5	0.512966	0.000012	6.4	0.1521	0.0013	0.8
<b>BCR2</b>	3	0.512616	0.000011	-0.4	0.1377	0.0010	0.7
<b>G2</b>	3	0.512225	0.000013	-8.1	0.0808	0.0013	1.6

Note that the difference between the average MC-ICP-MS data and the average ID-TIMS results do not exceed 0.2  $\epsilon\text{Nd}$  units (present-day values). As reported by GeoREM, the basalt standard BCR2 has a  $^{143}\text{Nd}/^{144}\text{Nd} = 0.51263 - 0.512638$  and  $^{147}\text{Sm}/^{144}\text{Nd} = 0.1383$ .

## 2.4 Results

### 2.4.1 Nd, U-Pb isotopes

The data used to construct the Sm-Nd isochrons for both the Lower- and Upper Lava units are provided in Table 2. The Lower Lava of the Eastern and Western limb defines a 10-sample whole-rock isochron registering an age of  $3,420 \pm 140$  Ma, an initial  $^{143}\text{Nd}/^{144}\text{Nd}$  ratio of  $0.50848 \pm 13$  ( $\epsilon\text{Nd}_i = +5.7 \pm 2.5$ ) with a low value of 0.98 for the mean square weighted deviates, MSWD (Fig. 6A). Sm/Nd ratios for these lavas are subchondritic which is a result of the bulk rock being Light

Rare Earth Element (LREE) enriched — possibly from fractionation during melting of the mantle source. A relatively small range of  $^{147}\text{Sm}/^{143}\text{Nd}$  from 0.12 to 0.17 (Table 2) for the Lower Lava derives from the variable amounts of feldspar, altered glass, primary clinopyroxene and a few Western Limb samples having minor secondary amphibole.

Precise secondary ion microprobe U-Pb ages of 22 zircons (grains  $\sim 350\mu\text{m}$  long) were measured from a tuff unit which lies above the Lower Lava but just 30 cm conformably below the BIF (Fig. 3, 4; samples 4/03). The concordant  $3,392 \pm 29$  Ma tuff age (Fig. 7; Table 3) confirms the BIFs Paleoproterozoic antiquity (see Basu et al., 2008); stratigraphically agreeing with the Lower Lava's 3.42 Ga age. The significance of this tuff age is remarkable being close to that of the BIF, exceeding a 220m thickness in the type area with single ore bodies up to 3 km long along strike and several hundred meters wide. This makes the W-IOG BIF the largest for its age ( $> 5 \times 10^{10}$  tons) which remains a significant economic grade iron-ore deposit ( $> 60$  wt.%  $\text{Fe}_2\text{O}_3$ ; Beukes et al., 2008).

In addition to the Lower Lava isochron age agreeing with the tuff age, it is also consistent with the age of the younger Bonai granite  $\sim 3.37$  Ga (see, Asokan et al., 2021), which has an intrusive relationship with the western limb of the W-IOG syncline (Fig.3). The  $3.42 \pm 0.14$  Ga

**Table 2.** Sm-Nd isotope systematics data measured on the Western Iron Ore Group (W-IOG) greenstone lavas, Singhbhum Craton.

For analytical methods see Materials and Methods text for more details.

Sample	Rock Type	Sm (p.p.m)	Nd (p.p.m)	$^{147}\text{Sm}/^{144}\text{Nd} \pm 2\sigma$	$^{143}\text{Nd}/^{144}\text{Nd} \pm 2\sigma$
<u>Lower Lava</u>					
IG-10a/01	Basaltic Andesite	2.02	9.92	0.1239 ± 07	0.511283 ± 4
IG-10b/01	Basalt	3.92	15.38	0.1512 ± 11	0.511886 ± 5
IG-6a/01	Basaltic Andesite	2.29	11.16	0.1263 ± 10	0.511328 ± 4
IG-4	Basaltic Andesite	6.11	28.74	0.1262 ± 10	0.511353 ± 5
IG-1/03	Basalt	2.17	8.59	0.1505 ± 11	0.511866 ± 4
IG-4/01	Basalt	3.93	13.67	0.1717 ± 10	0.512364 ± 4
IG-3/01	Basaltic Andesite	4.16	18.96	0.1315 ± 08	0.511459 ± 6
IG-2b/01	Basaltic Andesite	3.12	13.62	0.1375 ± 08	0.511562 ± 4
IG-2a/01	Basalt	3.85	18.1	0.1297 ± 08	0.511368 ± 4
IG-8	Basaltic Andesite	2.93	11.25	0.1560 ± 14	0.511977 ± 5
<u>Upper Lava</u>					
UL-1/03	Basaltic Andesite	5.51	19.02	0.1757 ± 08	0.512395 ± 7
UL-2/03	Basaltic Andesite	4.22	19.27	0.1301 ± 08	0.511607 ± 7
UL-4/03	Basaltic Andesite	2.71	13.45	0.1195 ± 07	0.511419 ± 5
IG-15b/01	Basalt	2.48	10.48	0.1456 ± 08	0.511888 ± 6
IG-15c/01	Basaltic Andesite	3.13	14.89	0.1297 ± 10	0.511581 ± 5

\*Sm and Nd concentration data were determined by ICP-MS.

\*The Sm-Nd systematics in this study were carried out on MC-ICP-MS at CNRS, France. For further confirmation of the relatively new analytical technique employed in this study, see methodology.

\*Neodymium isotopes were normalized to  $^{146}\text{Nd}/^{144}\text{Nd} = 0.7219$ .

The mean of 25 measurements on the pure JNDi-1 standard during this study was 0.512101 (2SD = 0.000009), slightly lower than the recommended value of  $0.512115 \pm 22$ .

All sample numbers listed in Table 2 are shown in Figure 3 without the “IG” prefix.

**Table 3.** U-Pb geochronology for zircons from a volcanic tuff just below the BIF and above the lowermost shale as shown in Fig. 18. See Materials and Methods text for more details.

Zircon Grain	Th/U	± 1 s.e.	% Pb 206	Isotope Ratios					Age (Ma)							
				$^{207}\text{Pb}/^{235}\text{U} \pm 1 \sigma$	$^{206}\text{Pb}/^{238}\text{U} \pm 1 \text{ s.e.}$	$^{207}\text{Pb}/^{206}\text{Pb}$	$\pm 1 \text{ s.e.}$	$^{207}\text{Pb}/^{206}\text{Pb} \pm 1 \text{ s.e.}$	$^{206}\text{Pb}/^{238}\text{U} \pm 1 \text{ s.e.}$	$^{207}\text{Pb}/^{206}\text{Pb} \pm 1 \text{ s.e.}$	Conc. (%)					
1	0.469	0.009	99.79	24.6000	0.8090	0.6630	0.0216	0.2690	0.0026	3291	32	3278	84	3300	15	99
2	0.601	0.017	99.72	27.7000	1.2300	0.7080	0.0298	0.2840	0.0032	3409	44	3452	112	3384	18	102
3	2.030	0.052	99.53	15.4000	0.4400	0.4000	0.0113	0.2800	0.0027	2842	27	2168	52	3363	15	64
4	1.350	0.021	99.81	24.9000	2.1300	0.6300	0.0535	0.2870	0.0020	3306	83	3151	212	3401	11	93
5	0.546	0.016	99.64	26.1000	2.0700	0.6470	0.0494	0.2930	0.0042	3352	77	3217	193	3433	22	94
6	1.330	0.025	99.58	13.5000	0.3330	0.3990	0.0098	0.2450	0.0012	2713	23	2166	45	3150	8	69
7	0.750	0.016	99.79	28.0000	1.0900	0.7080	0.0286	0.2860	0.0015	3418	38	3451	108	3398	8	102
8	1.900	0.034	99.59	23.9000	1.0300	0.6050	0.0256	0.2860	0.0025	3262	42	3051	103	3395	14	90
9	2.350	0.044	99.72	24.3000	0.9410	0.6180	0.0235	0.2850	0.0017	3279	38	3101	94	3390	9	91
10	2.860	0.060	99.32	17.8000	0.5350	0.4780	0.0147	0.2700	0.0033	2979	29	2519	64	3306	19	76
11	0.698	0.010	99.84	20.9000	0.5150	0.5680	0.0139	0.2670	0.0012	3133	24	2899	57	3286	7	88
12	2.740	0.029	99.88	26.8000	0.8490	0.6790	0.0232	0.2860	0.0022	3376	31	3339	89	3397	12	98
13	2.720	0.045	99.68	26.0000	1.3200	0.6580	0.0333	0.2870	0.0024	3347	50	3259	130	3400	13	96
14	0.515	0.007	99.79	19.7000	0.6240	0.5310	0.0165	0.2690	0.0014	3075	31	2744	70	3299	8	83
15	1.190	0.022	99.88	27.1000	1.0600	0.6750	0.0266	0.2910	0.0017	3387	39	3324	102	3425	9	97
16	1.420	0.021	99.91	26.8000	0.8630	0.6630	0.0212	0.2930	0.0019	3375	32	3277	82	3434	10	95
17	0.501	0.010	99.81	24.3000	0.7460	0.6500	0.0195	0.2710	0.0018	3281	30	3228	76	3313	11	97
18	0.507	0.014	99.92	24.0000	0.9460	0.6450	0.0262	0.2700	0.0021	3268	38	3210	103	3304	12	97
19	0.640	0.047	99.34	23.8000	1.2400	0.6160	0.0321	0.2810	0.0044	3261	51	3093	128	3366	24	92
20	0.864	0.010	99.74	21.1000	0.4560	0.5650	0.0120	0.2710	0.0014	3144	21	2887	49	3313	8	87
21	1.670	0.058	99.38	16.7000	0.4360	0.4460	0.0121	0.2730	0.0026	2920	25	2375	54	3321	15	72
22	1.080	0.026	99.57	19.6000	0.8770	0.5060	0.0231	0.2810	0.0021	3073	43	2638	99	3371	12	78

age of the Lower Lava Sm-Nd isochron and the U-Pb zircon tuff age places the antiquity of the W-IOG into the same emplacement timeline as the 3.51 Ga U-Pb zircon age for the S-IOG (Mukhopadhyay et al., 2008) and E-IOG (Jodder et al., 2021) greenstone belts in Singhbhum (Fig. 16). The Upper Lava greenstones, collected on a 4 km traverse, lie on a 5-sample whole-rock isochron which yields an age of  $2,654 \pm 104$  Ma and an initial  $^{143}\text{Nd}/^{144}\text{Nd}$  ratio of  $0.509332 \pm 97$  (initial  $\epsilon_{\text{Nd}} = +2.7 \pm 1.9$ ; Fig. 6B). This isochron also displays a small range of Sm/Nd ratios from 0.11 to 0.17 with an MSWD of 0.57 (Table 2).

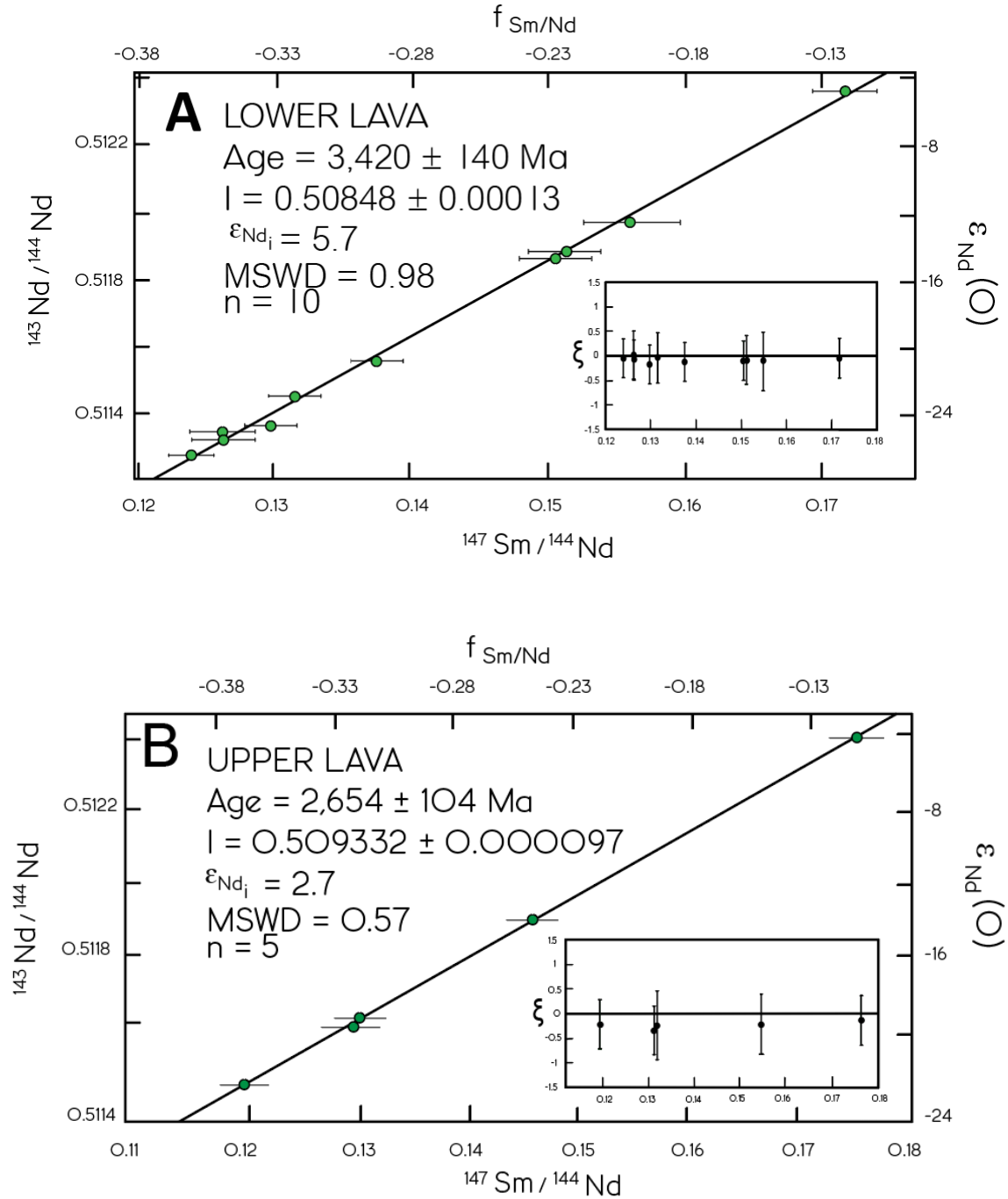


**Figure 6. Isotope Geochronology for the W-IOG Lower Lava and Tuff (IG-4/03) (A)** Ten whole-rock samples Sm-Nd age and initial for the Lower Lava greenstones of the W-IOG. **(B)** Five whole rock samples Sm-Nd age and initial for the Upper Lava greenstones. The inset shows  $\xi$  vs  $^{147}\text{Sm}/^{144}\text{Nd}$ , where  $\xi$  represents the deviation, in  $\epsilon$  units, of each data point from the best-fit line.

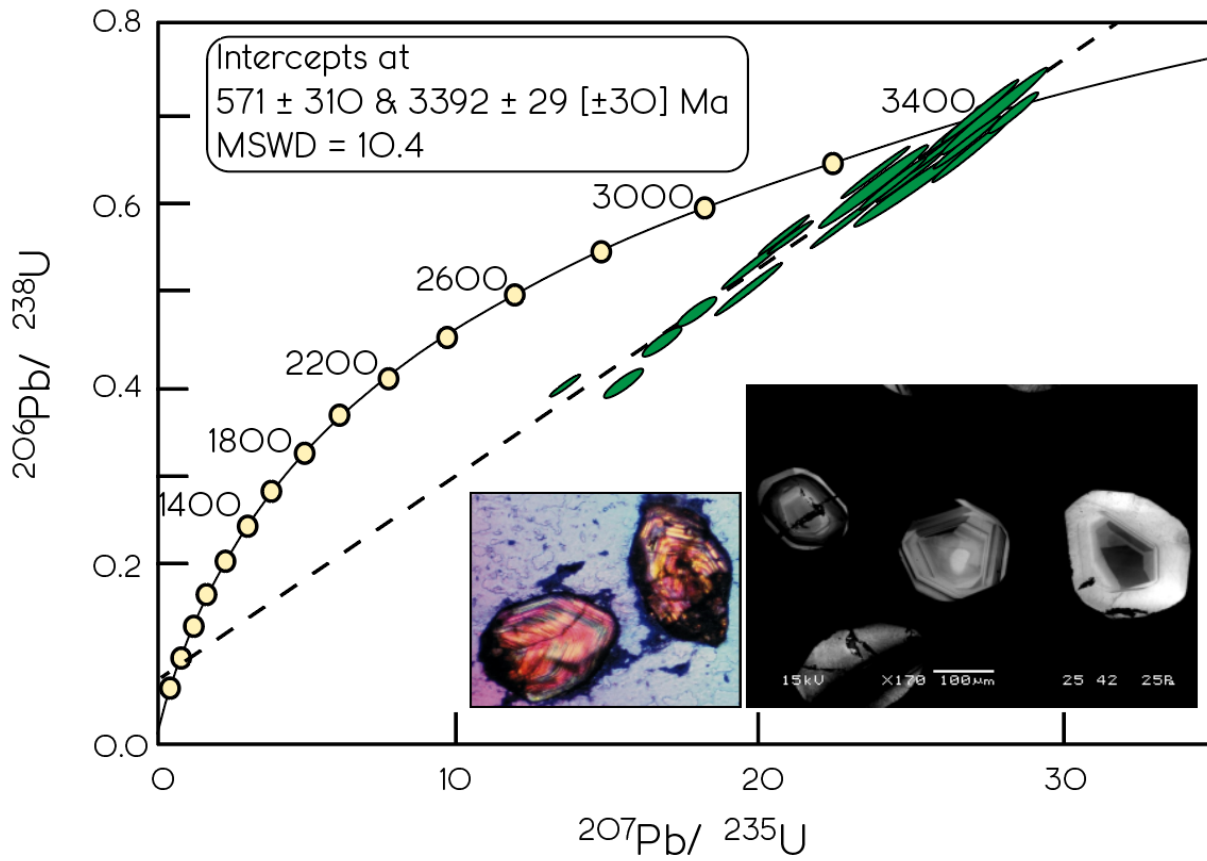


**Figure 7.** A precise U-Pb isotopic plot of 22 zircon grains separated from the stratigraphically intermediate tuff layer (sample IG-4/03; Fig. 17) < 30 cm below the banded iron formation. The zircons (inset) show oscillatory zoning, igneous Th/U=1.7 to 2.5. Data ellipses are at the 1 $\sigma$  level.

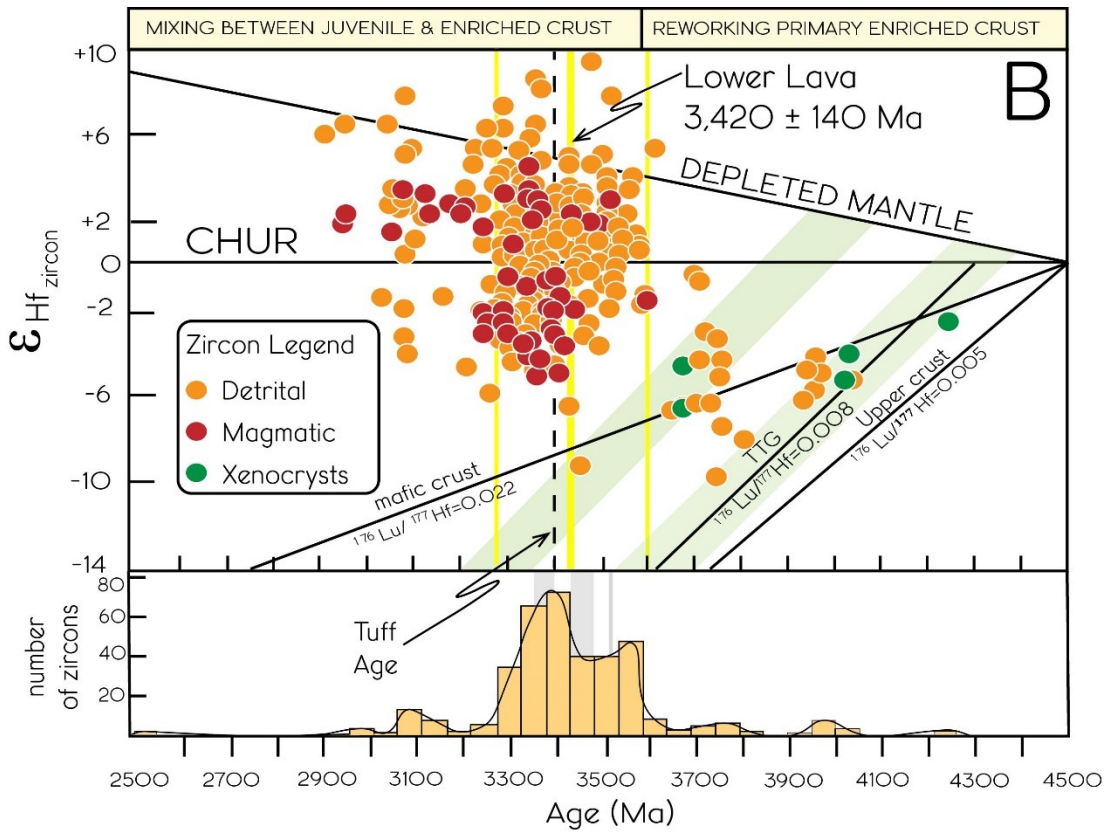
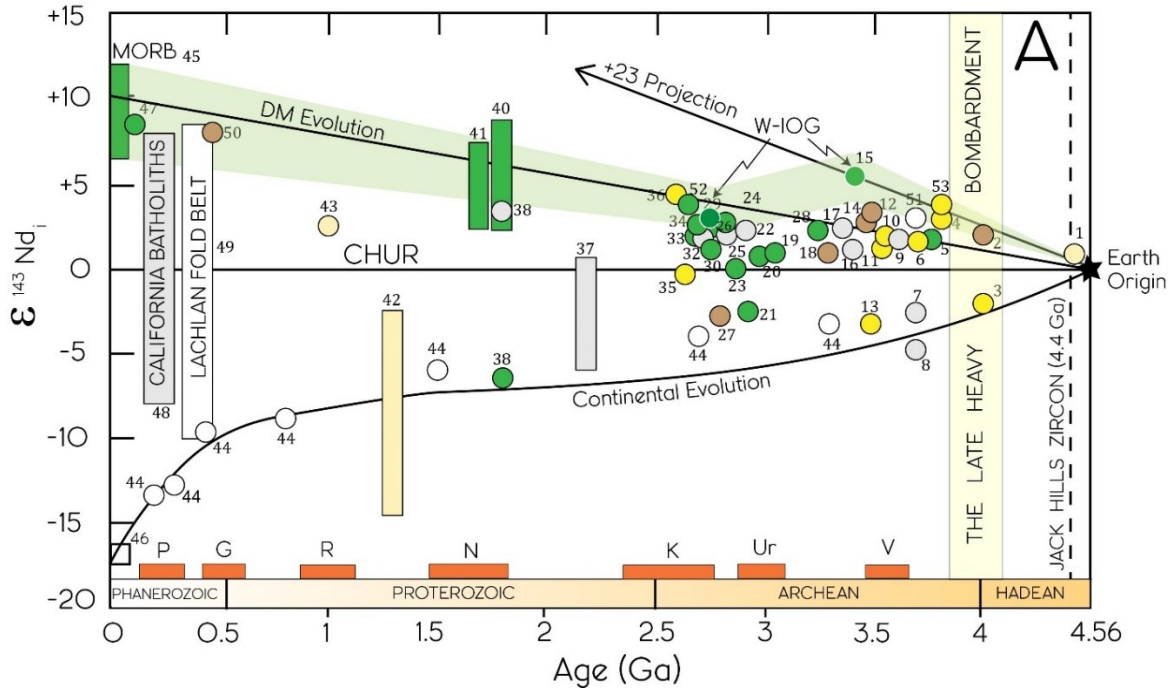


**Figure 8.** Isotope evolution diagrams. (A) Initial  $\epsilon_{Nd}$  evolution diagram for the depleted mantle isotopic array complementary to the crustal array. Previous terrestrial data corresponds to the

reference numbers given in the Appendix. The two small green circles represent measured Lower- and Upper-Lava ages and initials reported in this study. Orange boxes represent supercontinent and/or hypothesized supercraton events found in literature (e.g., Mahapatro et al., 2012). The light green band represents the depleted mantle evolution trajectory inferred from the W-IOG data. Green circles represent meta-basalts; Yellow are ultramafics; Brown are gabbro/amphibolite; Orange are anorthosite; Grey are granitoids; and White are sedimentary. (B) Plot of initial epsilon Hf vs. absolute U-Pb age of zircons from the Singhbhum Craton (see, Chaudhuri et al., 2018; Sreenivas et al., 2019; Miller et al., 2018; Ranjan et al., 2020; Jodder et al., 2021; Dey et al., 2017). The three light yellow bars represent Sm-Nd isotope age range for the Lower Lava. Zircons from the tuff unit give a U-Pb age of 3.39 Ga, represented as the bold dashed vertical line. As this tuff unit lies above the Lower Lava (Fig. 18), 3.39 Ga is its minimum age. Note that the influence of the depleted mantle occurs at ~3.5 Ga, coinciding with the formation of the W-IOG Lower Lava greenstones. Shaded Gray regions in the histogram represent major TTG crustal formation events in Singhbhum. CHUR, Chondritic Uniform Reservoir.

## 2.4 Discussion

The mantle source for the Lower Lava greenstones represents the highest inferred time-integrated  $^{143}\text{Nd}/^{144}\text{Nd}$  ratio (with-respect-to chondrite) of any Archean suite reported to date, using the “real age” isochron technique and not individually calculated model  $\epsilon_{\text{Nd}}$  values using other chronometers for the age at the time of its initial value (Fig. 8A). Assuming planetary fractionation occurred at 4.5 Ga, the early depleted mantle reservoir the Lower Lavas were derived from (initial  $\epsilon_{\text{Nd}}$  value = + 5.7) at 3.42 Ga has an estimated present-day  $^{143}\text{Nd}/^{144}\text{Nd} = 0.513817$  and  $^{147}\text{Sm}/^{144}\text{Nd} = 0.236$  ratio that projects to a modern day  $\epsilon_{\text{Nd}} = +23 \pm 10$ . Straddling this evolution line are ultramafics from Labrador (Collerson et al., 1991) and West Greenland (Locht et al., 2020) which depict the presence of an existing terrestrial mantle reservoir with a similar Sm-Nd fractionation history. Since a younger mantle separation age requires the existence of increasingly higher present-day  $\epsilon_{\text{Nd}}$  values, we propose  $\epsilon_{\text{Nd}} = +23$  to be a more reasonable estimate. Thus, the Lower Lava’s initial  $\epsilon_{\text{Nd}}$  value (+5.7) argues having been derived from a long-lived (>1 Ga) mantle source which evolved within a closed system. This observation is consistent with previous studies that report Nd

isotopic data supporting the presence of chemical heterogeneities in Earth's early mantle which persisted for at least the first billion years of Earth history, as well as highly depleted mantle reservoirs (e.g., Bennett et al., 1993, 2007; Hoffmann et al., 2010).

It has been problematic to compare the depleted  $\epsilon^{143}\text{Nd}$  signature reported by other studies from the Singhbhum Craton to that recorded by the W-IOG Lower Lava in the current study. This is because these reported ages and initial  $\epsilon_{\text{Nd}}$  values were either not derived from an isochron (e.g., Chaudhuri et al., 2017; Asokan et al., 2023; Pandey et al., 2019), derived from an errorchron (e.g., Pandey et al., 2019; Maltese et al., 2022), samples were significantly affected by crustal contamination (e.g., Adhikari et al., 2021a; Adhikari et al., 2021b; Chaudhuri et al., 2017), or its isochron derived age does not agree with other independent stratigraphic chronometers (e.g., Basu et al., 1981; Adhikari et al., 2021b). It is important to specify that the assumed initial  $\epsilon_{\text{Nd}}$  value of +5.2 for a single Singhbhum Granitic sample accepted by Pandey et al. (2019) and reused by Maltese et al. (2022) was calculated not from a reliable isochron, but from using a single U-Pb zircon age, whose  $^{147}\text{Sm}$ - $^{143}\text{Nd}$  data also formed an errorchron (very high MSWD) according to Pandey et al. (2019). The results from these discussed studies suggest the samples were not cogenetic, and have not remained a closed system, or were the result of a mixing line between two or more temporally distinct magmatic events. The strength of the current study is that the initial  $\epsilon_{\text{Nd}}$  value (+5.7) and age (3.42 Ga) of the Lower Lava are derived from a well-constrained isochron (closed-system behavior), whose age agrees with two independent stratigraphic chronometers. Plotting the  $^{143}\text{Nd}/^{144}\text{Nd}$  vs  $1/\text{Nd}$  (ppm) for both the Lower- and Upper Lava do not exhibit a correlation, suggesting they are not mixing lines. Lastly, the calculated initial  $\epsilon_{\text{Nd}}$  values for the individual samples comprising both the Lower Lava ( $\pm 0.3$ ) and Upper Lava ( $\pm 0.1$ ) exhibit low deviations from their isochron derived initial  $\epsilon_{\text{Nd}}$  values indicating their cogenetic derivation.

Hafnium isotopes can provide an independent examination for the plausibility of the neodymium data since the behavior of the  $^{147}\text{Sm}$ - $^{143}\text{Nd}$  system parallels that of the  $^{176}\text{Lu}$ - $^{176}\text{Hf}$  system. The current  $\text{Hf}_{\text{zircon}}$  isotopic record from the Singhbhum Craton (Fig. 8B), suggests that an enriched primary crust (implied from the presence of only negative  $\epsilon_{\text{Hf}}$  values) evolved not from the addition of juvenile magma from the mantle, but rather from extensively reworking of an older existing enriched crust between the Hadean (4.2 Ga) to the Eoarchean ( $\sim 3.5$  Ga) (e.g., Bauer et al., 2020). This older Hadean enriched crust suggests the existence of an isolated complementary depleted mantle reservoir equivalent in age. The simultaneous occurrence of both positive and negative  $\epsilon_{\text{Hf}}$  values abruptly beginning at  $\sim 3.5$  Ga signals the sustained emergence for the addition of a juvenile mantle signature (e.g., Sreenivas et al., 2019). This excursion of positive  $\epsilon_{\text{Hf}}$  values coincides with the emplacement of the  $3.42 \pm 0.14$  Ga Sm-Nd whole-rock age of the Lower Lava greenstones. Therefore, the 1-billion-year interval from 4.5 to 3.5 Ga provides a reasonable geological timescale for the closed system ingrowth of  $^{143}\text{Nd}$  to occur in order to impart their distinctly positive initial ( $\epsilon_{\text{Nd}} = +5.7$ ) value (Fig. 8A). An early Earth differentiation event for the Singhbhum craton is consistent with the inferred 4.2-4.5 Ga separation model ages (Chaudhuri et al., 2018; Maltese et al., 2022). The emergence of a zircon Hf juvenile signature at 3.5 Ga, with many samples having initial  $\epsilon_{\text{Hf}} > +6$  above the proposed Hf evolution curve for the depleted mantle (Fig. 22B), may indicate that the high-inferred depleted nature recorded by the W-IOG Lower Lava greenstones is a characteristic of the Singhbhum craton preserved in both the Nd and Hf isotopic systems.

The difference in 3  $\epsilon^{143}\text{Nd}$  units between the  $\sim 770$  Ma emplacement period for the Lower Lava (5.7 at 3.42 Ga) and Upper Lava (2.7 at 2.65 Ga) could either be interpreted to reflect the sampling of different mantle sources, or the progressive recycling of LREE-enriched material into

the mantle source (e.g., Frost et al., 2023). If the latter is correct, then the  $\epsilon^{143}\text{Nd}$  became suppressed, preventing the growth of a depleted mantle reservoir with ever positive values from resulting as preserved by some samples from other planetary silicate bodies (e.g., Moon and Mars; Borg et al., 2011; Lapen et al., 2017) that lack an active surface recycling plate tectonic regime (e.g., Armstrong, 1991; Bowering and Housh, 1995). The difference between the inferred present-day W-IOG depleted mantle source for the Lower Lava (+23) and present-day MORBs (+10) suggests that crustal recycling has suppressed Earth's mantle by a minimum of 13  $\epsilon_{\text{Nd}}$  units over 3.4 Ga geologic time. However, this assumes that the depletion recorded in the Singhbhum craton is representative of a global phenomenon, that is a mantle vestige of the early differentiation of the primary crust.

## **2.5 Conclusions**

We obtained a 3.42 Ga Sm-Nd isochron age for the Lower Lava, which agrees with the 3.39 Ga zircon U-Pb age obtained for the stratigraphically overlying tuff. The Lower Lava's initial  $^{143}\text{Nd}$  suggests derivation from a source that represents one of the best-preserved examples of early Earth's Hadean LREE- depleted mantle reservoir, whose  $^{143}\text{Nd}$  evolution mirrors that of the  $^{176}\text{Hf}$ -enriched crust as preserved in Singhbhum's zircon record. The new Nd isochrons reported between the Lower Lava and the unconformable Upper Lava bracket the depositional age of the W-IOG basin between 3.42-2.65 Ga. Lastly, the 3.39 Ga zircon tuff age immediately below the conformably overlying huge BIF deposit indicates large variations of free atmospheric oxygen during the Paleoarchean.

## CHAPTER 3

### RELATIONSHIP BETWEEN FLOOD BASALTS AND LARGE BANDED IRON FORMATION 3.4 GA

#### **3.1 Abstract**

A genetic relationship between Banded Iron Formations (BIF) and flood basalts has long been assumed based on their close temporal and spatial association. However, proving causation has remained difficult given the absence of geochemical evidence, leading some authors to speculate BIFs are not primary deposits. Herein the entire lithological suite of the western Iron Ore Group from the Singhbhum craton, which includes Earth's largest economic grade BIF of its Paleoproterozoic age. The Lower Lava flood basalts to plot on a Sm-Nd isochron with the conformably overlying Lower Shale, suggesting a  $3.42 \pm 0.10$  Ga depositional model age for this iron-rich (avg. 18.26 Fe<sub>2</sub>O<sub>3</sub> wt.%,  $n = 7$ ) clastic unit, implying it may be a progenitor to the conformably overlying  $3.39 \pm 0.02$  Ga BIF. This is the first occurrence of flood basalts being genetically linked to ferruginous shale on a Sm-Nd isochron and may support the hypothesis that BIFs are products of secondary replacements of ferruginous clastic precursors. We assign a volcanogenic origin to this Algoma-type BIF and suggest its abnormally large size is related to the unroofing of the Lower Lava flood basalts during a major crustal formation event.

#### **3.2 Introduction**

While Banded Iron Formations (BIF) serve as the essential economic iron reservoirs mined for industrial activities, their presence in the rock record is also thought to monitor the gradual oxygenation of Earth's ocean-atmosphere system (Klein, 2005). However, many aspects of their formation such as depositional cause, source of iron, and depositional rate have become

increasingly unclear (e.g., Bekker et al., 2010; Ding et al., 2022; Lantink et al., 2022; Wang et al., 2009). This lack of clarity has bifurcated the genesis of BIFs to either be viewed as primary chemical precipitates or secondary replacements of iron-rich clastic precursors (e.g., Dunn, 1935; Krapez et al., 2003; Robbins et al., 2019), whose source of iron was either introduced from submarine hydrothermal vents (e.g., Polat and Frei, 2005; Derry and Jacobsen, 1988), subaerial weathering of the continental landmass (e.g., Alibert and McCulloch, 1993; Miller and O’Nions, 1985; Morris and Horwitz, 1983; Gruner, 1922) or a hybrid of the two models (e.g., Li et al., 2015). One reason for such conflicting provenance interpretations is because studies typically restrict themselves to focusing on the geochemical information extracted only from BIFs, which are notoriously endowed with complex diagenetic and metamorphic histories (e.g., Gregory, 1986). Furthermore, although younger BIFs are typically better preserved, their association with multi-cycle sediments makes it difficult to evaluate the BIFs depositional relationship between the provenance of coeval clastic sedimentary rocks.

The purpose of this study is to apply geochemical proxies such as major and trace elements, as well as the  $^{147}\text{Sm}$ - $^{143}\text{Nd}$  isotopic system (based on the long-lived decay of  $^{147}\text{Sm}$  to  $^{143}\text{Nd}$ , decay constant  $\lambda_{\text{Sm}} = 6.54 \times 10^{-12} \text{ yr}^{-1}$ ) on well-preserved shales that conformably over-and-underlie a BIF succession from the western Iron Ore Group (W-IOG) greenstone belt, Eastern India, in order to assess their source, depositional rate, and age which can provide an evolutionary geologic framework for the origin of the BIF. Located in the Singhbhum craton, the W-IOG is part of a regional (55 x 35 km) NNE-plunging asymmetric synclinorium structure in the Jamda-Koira Valley (Fig. 2, 3). The recent work by Wright and Basu (2024) established a 3.42 Ga Sm-Nd isochron age for the Lower Lava flood basalts, which is the lowermost stratum of the W-IOG, as well as a 3.39 Ga U-Pb zircon age for a tuff that conformably lies less than 30 cm below the

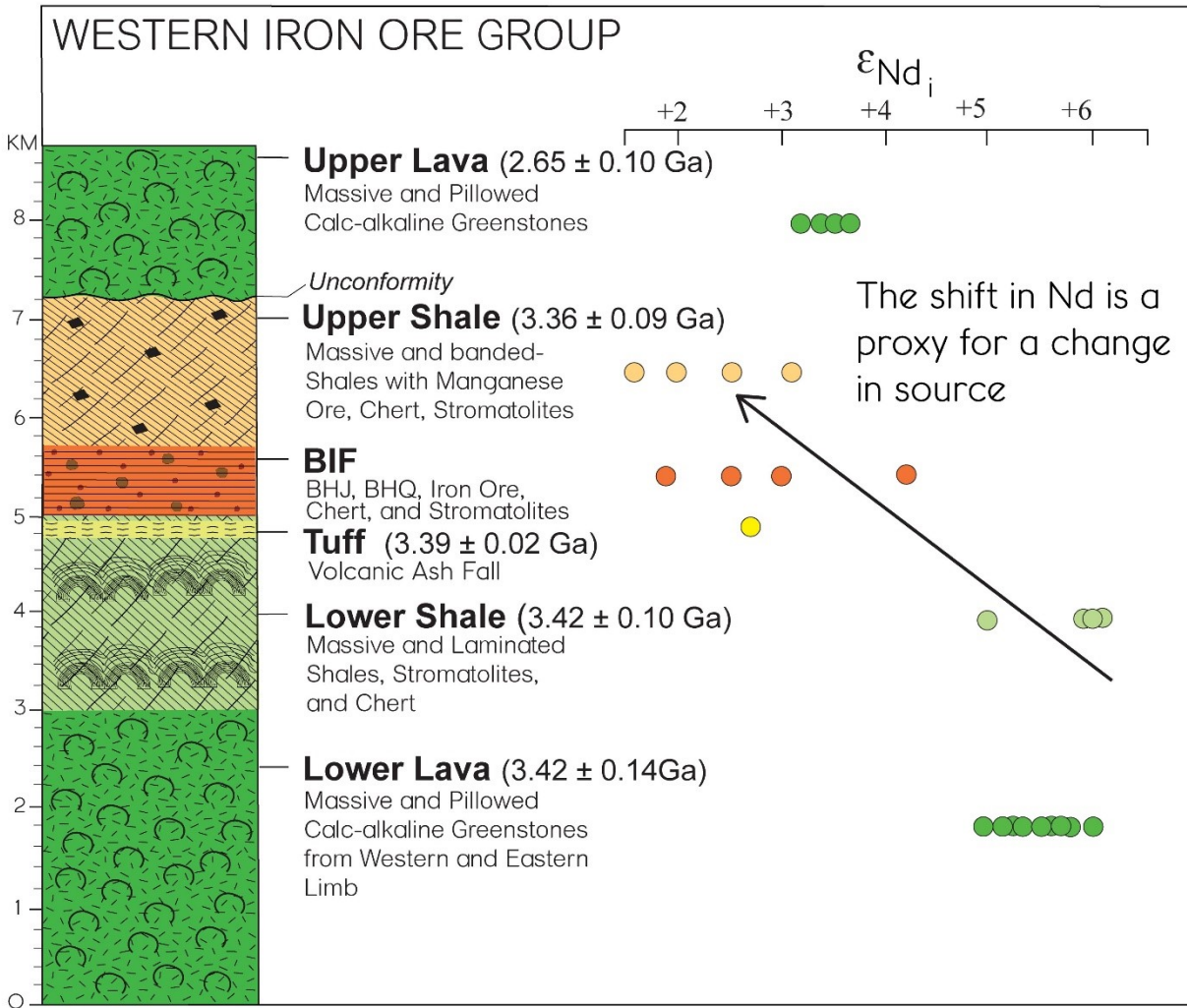


**Figure 9.** Stratigraphic succession of the western Iron Ore Group greenstone belt. Age constraints from Wright and Basu (2024) and the present study. These ages agree with their stratigraphic position. The arrow indicates the petrogenetic links with respect to the BIF as proposed in this study. The BIF and tuff thicknesses are exaggerated. See the Sm-Nd methodology in the Supplemental Material for the definition and explanation of initial  $\epsilon_{Nd}$ . Modified after Basu 2008; Jones, 1934; Dunn, 1940; Mukhopdhyay, 1988.

intermediate BIF (Fig. 4). Furthermore, Shales make up two significant lithologies within the W-IOG stratigraphy, wherein the “Lower Shale” conformably underlies, and the BIF succession conformably underlies the “Upper Shale” (Fig. 9).

The apparent significance of this stratigraphic relationship comes from the observation that both shale units exhibit areas with excellent preservation of original fissile textures, often being undeformed, and unmetamorphosed. Furthermore, unlike most Archean BIFs which are highly deformed, small-sized, and economically insignificant, the W-IOGs BIF is relatively undeformed, large ( $5 \times 10^{10}$  tons), and a high-grade ( $> 60$  wt.%  $\text{Fe}_2\text{O}_3$ ; see Beukes et al., 2008) economic deposit. Therefore, the W-IOG provides a unique opportunity to study in detail a well-preserved section of Paleoarchean history, especially since the antiquity and large size of this BIF implies that 1-billion-years prior to the Great Oxygenation Event, large variations of free atmospheric oxygen existed as more than just whiffs (e.g., Anbar et al., 2007; Basu et al., 2008).

Starting with the oldest, lowermost stratum and working upward through the stratigraphic succession, each successive layer from the W-IOG is evaluated and used to assess development stages associated with the emplacement of Earth's largest Paleoarchean BIF.

### **3.3 Materials and Methods**

#### *3.3.1 X-Ray Diffraction*

Modal mineral assemblages from selected samples were determined through the utilization of the X-ray Diffraction (XRD) method. Homogenized whole-rock powders were pressured into pellet disks and analyzed in a Shimadzu-7000 x-ray diffractometer at the Department of Earth and Environmental Science, University of Texas at Arlington.  $2\theta$  scans were performed employing  $\text{CuK}_\alpha$  radiation at 40 kV and 30 mA, while operating with a scanning condition set from a range of 3-65 degrees.

### 3.3.2 Major and trace element procedure

Trace element concentrations were determined using an Inductively Coupled Plasma Mass Spectrometer (ICP-MS) (Thermo elemental X-7) at the University of Rochester, NY. For ICP-MS analysis, 25-50 mg of homogenized whole-rock sample powder were treated with trace element grade HNO<sub>3</sub> and HF acid mixtures and digested and diluted to 100 mL in 2% HNO<sub>3</sub> solution and spiked with ~10 ppb internal standards of In, Cs, Re and Bi. The elemental concentrations for these samples were analyzed using known concentrations from the external standards BIR-2 and BCR-2. Repeated measurements of AGV-2 and BHVO-2 standards were ran as unknowns to estimate the concentrations of various elements within less than 5% error. Whereas, the rare earth elements, particularly Sm and Nd, were more precisely determined within less than 2% error, respectfully. Major element concentrations were analyzed using two different laboratories. First, major element concentrations were analyzed on a Jobin-Yuon Ultima-C Inductively Coupled Plasma Optical Emission Spectrometry (ICP-OES) at Boston University. For flux fusion digestion analysis, 100 mg of sample were introduced to the instrument in 5% HNO<sub>3</sub> in a Meinhardt-C nebulizer with a flow rate of about 1 mL/min. Ultima-C routinely achieves better than 3 to 4% drift over a typical 12-hour analytical session. Blank solutions were prepared identically to analyzing samples and were ran at the beginning at each ran. Several standard reference materials were used to generate a calibration curve. Calibration curves typically had a rsq value of 0.99 or better and were used to calculate sample concentrations. Major and trace element analyses were also conducted by a commercial laboratory (ACTLAB) and are indicated by an asterisk next to the sample identification in Table 4. A lithium metaborate fusion technique was deployed. A molten bead is digested in nitric acid solution, and analysis was done by ICP-OES and ICP-MS. Several replicates

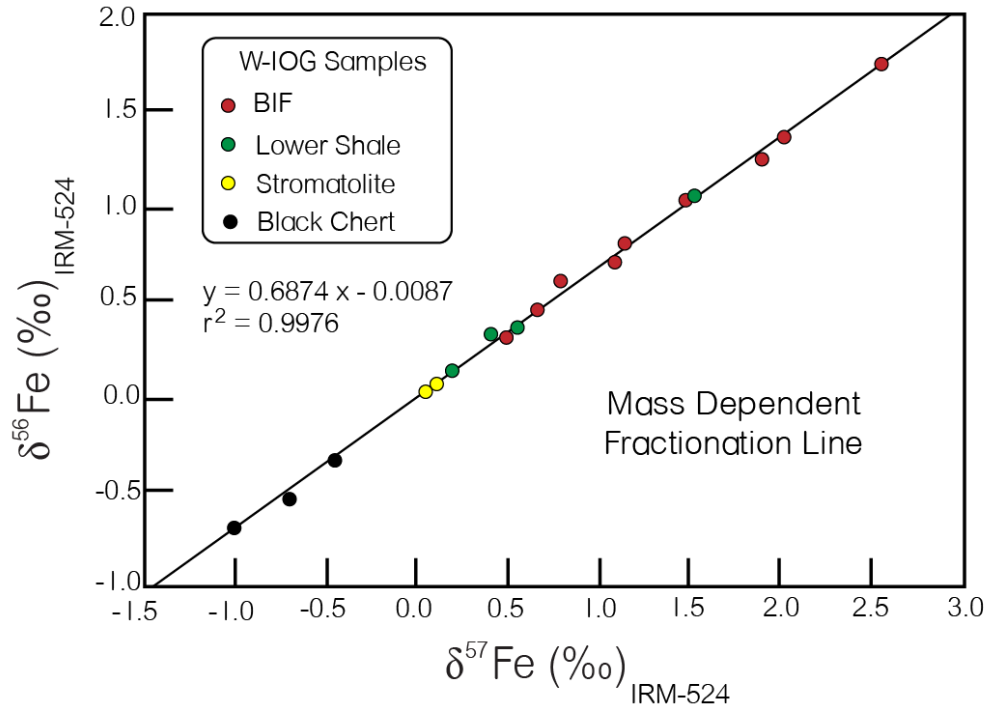


**Figure 10.** Plot of measured  $\delta^{56}\text{Fe}$  versus  $\delta^{57}\text{Fe}$  values of W-IOG samples analyzed from this study. The isotopic variations plot along the mass dependent equilibrium fractionation line.

and standards were used with an analytical error less than 5%. Whereas, the rare earth elements, particularly Sm and Nd, were more precisely determined within less than 2% error, respectfully. Loss on ignition (LOI) was determined by heating the sampled powder to 1050°C for two hours. Subsequently the weight difference of the powders was then weighed and calculated.

### 3.2.3 Iron isotope analytical procedure

Iron isotope analyses were carried out on a MC-ICP-MS Neptune Plus ThermoFisher Scientific (LMV, Clermont-Ferrand). Iron isotopes were resolved from Argide interferences ( $\text{ArO}^+$ ,  $\text{ArOH}^+$  and  $\text{ArN}^+$ ) using the high mass resolution mode ( $M/\Delta M \approx 10000$ ). The four iron isotopes  $^{54}\text{Fe}$ ,  $^{56}\text{Fe}$ ,  $^{57}\text{Fe}$ ,  $^{58}\text{Fe}$  were measured simultaneously along with  $^{53}\text{Cr}$  and  $^{60}\text{Ni}$  to correct respectively from the interference of  $^{54}\text{Cr}$  on  $^{54}\text{Fe}$  and of  $^{58}\text{Ni}$  on  $^{58}\text{Fe}$ . Instrumental mass bias and

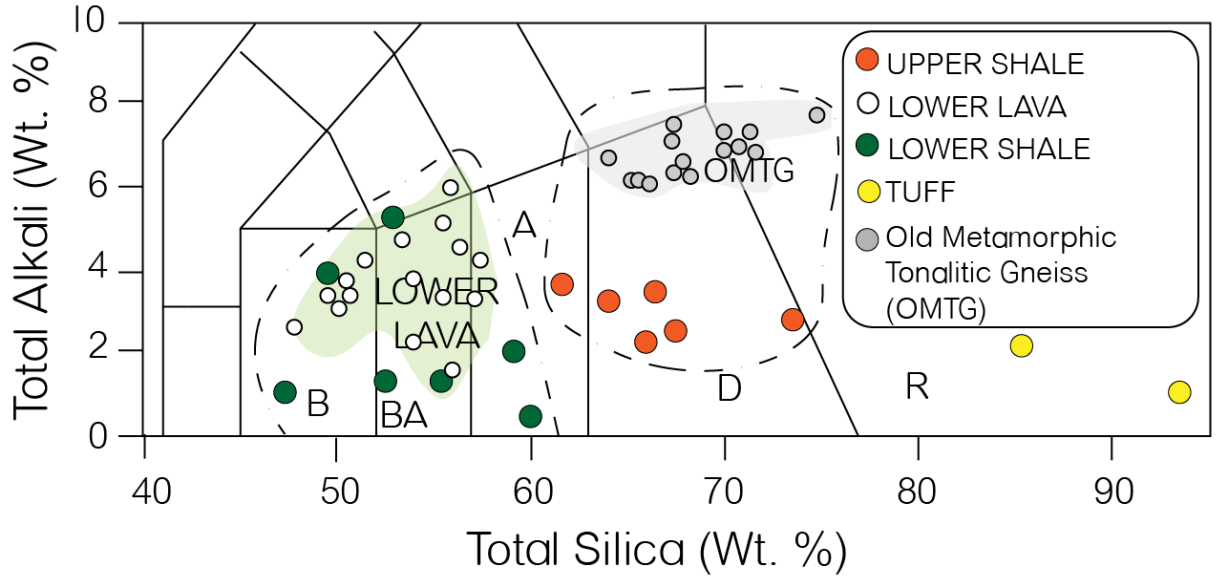


**Figure 11.** Clastic samples affinities as seen on a Total Alkali versus Silica diagram. The green field represents the parameters for the Lower Lava (western and eastern limb). The Lower Shale is nearly all basaltic and overlaps the Lower Lava field. In contrast, the Upper Shale is mostly dacitic like the Old Metamorphic Tonalitic Gneisses (OMTG). Abbreviations: B, Basalt; BA, Basaltic Andesite; A, Andesite; D, Dacite; R, Rhyolite. OMTG data from Sharma et al., 1994 and Basu et al., 1981.

drift were corrected using the standard bracketing method (Beard et al., 2003; Rouxel et al., 2003; Albarède and Beard, 2004). Iron isotopes compositions are reported as  $\delta^{56}\text{Fe}$  and  $\delta^{57}\text{Fe}$  relative to IRMM-524 standard, whose isotopic composition is identical to the out-of-stock IRMM-014 (Craddock and Dauphas, 2011), and, is expressed in per mil (‰) units according to the following equations:

$$\text{Eq.10} \quad \delta^{56}\text{Fe} = \left[ \frac{({}^{56}\text{Fe}/{}^{54}\text{Fe})_{\text{sample}}}{({}^{56}\text{Fe}/{}^{54}\text{Fe})_{\text{IRM-524}}} - 1 \right] \times 1000$$

The data set plots along a mass dependent equilibrium fractionation line as seen on a  $\delta^{56}\text{Fe}$  versus  $\delta^{57}\text{Fe}$  plot (Fig. 10) with a slope of 0.68.

## 3.4 Results

### 3.4.1 Mineralogy and major elements

Major element data is provided in Table 4. The Lower Shale features an unusually high iron concentration (12.08 to 24.68; avg. 18.26 Fe<sub>2</sub>O<sub>3</sub> wt.%,  $n = 7$ ), which is reflective in its mineralogical composition (quartz-kaolinite-muscovite-Fe-chlorite  $\pm$  hematite  $\pm$  magnetite  $\pm$  montmorillonite  $\pm$  smectite). In comparison, the conformably overlying BIF exhibits the highest concentration ( $30.43 \leq \text{Fe}_2\text{O}_3 \leq 84.55$  wt.%; avg. 52.01 Fe<sub>2</sub>O<sub>3</sub> wt.%,  $n = 10$ ), indicative of its ferruginous mineralogical composition (quartz-magnetite-hematite), while the conformable Upper Shale shows the lowest ferruginous composition (1.54 to 9.48; avg. 6.73 Fe<sub>2</sub>O<sub>3</sub> wt.%,  $n = 6$ ), which is also seen in its mineralogical composition (quartz-kaolinite-muscovite-hematite). On a Total Alkali vs Silica diagram (Fig. 11; see LeBas et al., 1986), the Lower Shale overlaps with the Lower Lava, depicting a mafic affinity. The Upper Shale exhibits a dacitic affinity like Singhbhum's Old Metamorphic Tonalitic Gneiss (OMTG) suite that is adjacent to the W-IOG basin (Fig. 2), and the tuffs show rhyolitic affinities. See Fig. 12 for photomicrographs.

### 3.4.2 Trace elements

Trace element data is provided in Table 4. On a primitive-mantle normalized plot, the different lithologic members of the W-IOG all show a strikingly similar pattern which includes positive Th-U-Pb anomalies and negative Nb-Ta anomalies. The Lower Shale mimics the Lower Lava's trace element patterns (Fig. 13A), including flat heavy rare earth elements (REE) which is suggestive of a mafic source. The tuffs characteristically exhibit overall higher total concentrations of incompatible elements, as well as more fractionated light REEs and pronounced negative Eu and Sr anomalies (Fig. 13B), indicative of intracrustal partial melting due to plagioclase fractionation

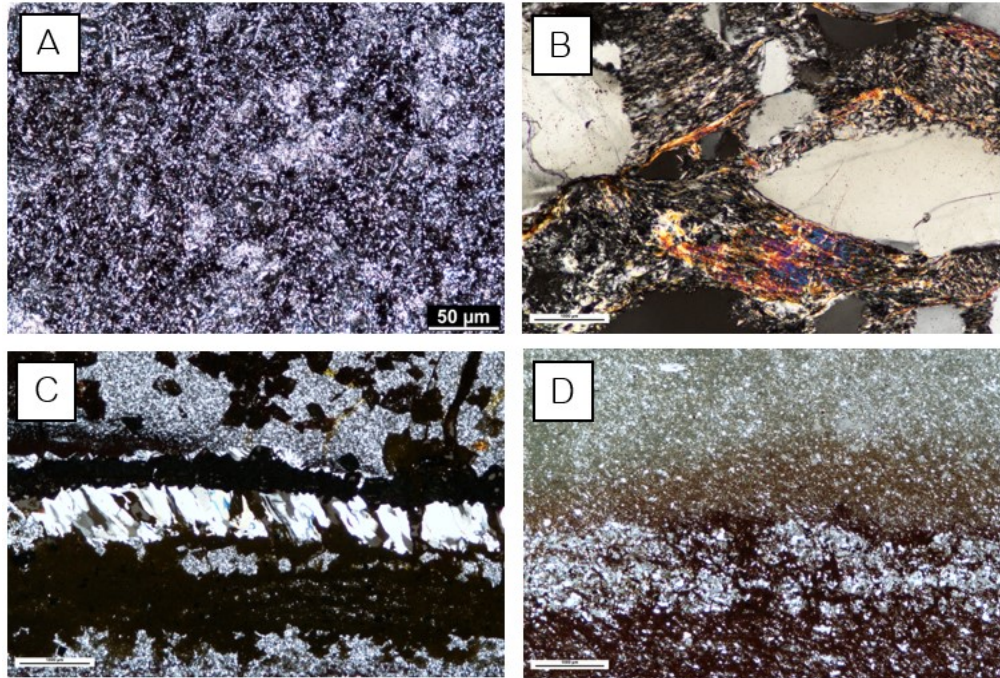


**Figure 12.** Photomicrographs of sedimentary western Iron Ore Group rocks. (A) An unmetamorphosed Lower Shale (IG-5/03) exhibiting predominantly fine grained quartz, kaolinite, muscovite, chlorite, and montmorillonite; (B) Tuff (IG-4/03) exhibiting vugs of volcanic glass and a fine texture of angular quartz in a fine matrix of sericite; (C) Banded Hematite Jasper (BIF-5) featuring microcrystalline band of chert adjacent to dark ribbons of magnetite and hematite; (D) An unmetamorphosed Upper Shale (IG-9/03) displaying well-developed planar laminations by light colored kaolinite-quartz and darker hematite rich layers. The scale bar for B, C, and D represents 1000 micrometers.

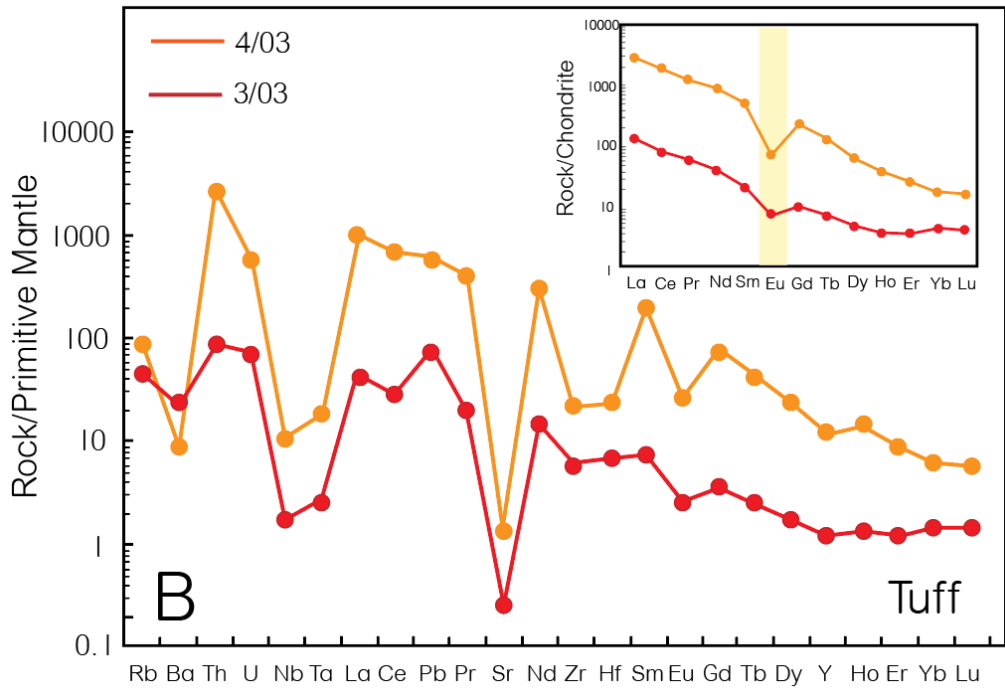
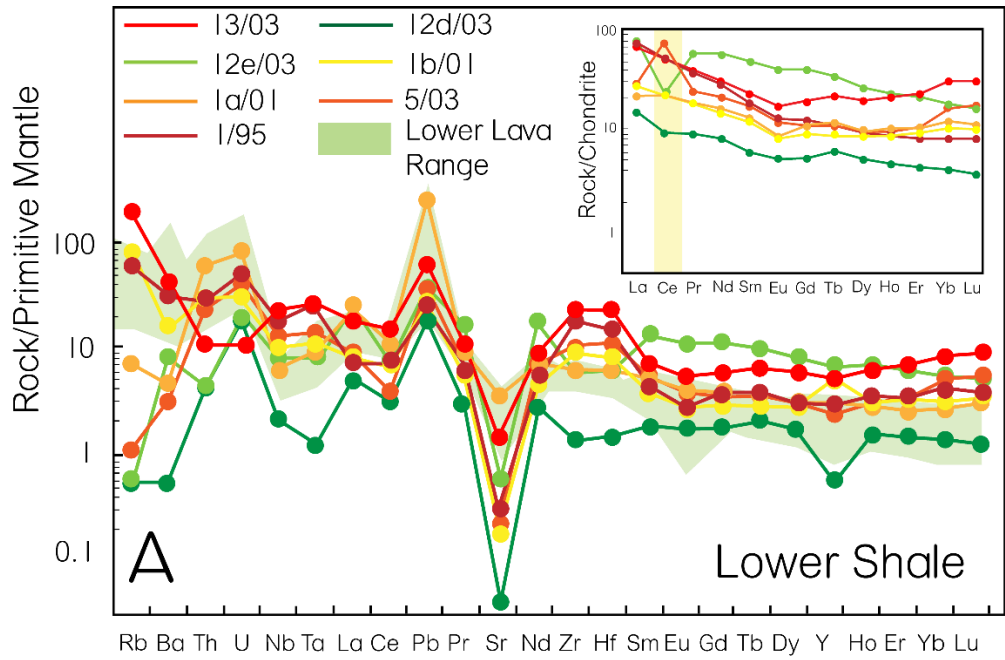
of an extraneous Tonalite-Trondhjemite-Granodiorite source. Although the absolute abundances of the BIFs trace elements vary widely (Fig. 13C), they strikingly resemble the Lower Lavas and tuffs, suggesting the BIF reflects syndepositional volcanic inputs forming a mixture between the Lower Lava (or Lower Shale) and the aerial input of the airfall tuff. A ferruginous chert (IG-6) with small amounts of clay content mirrors the Lower Lava pattern, implying clay formation during Lower Lava weathering may have played a significant role. The Upper Shale, on the other hand, shows a close correspondence between the OMTG (Fig. 13D), which includes slightly

greater fractionation of heavy REE patterns—indicative of a felsic source. The presence of a negative Sr anomaly in the Upper Shale may be due to its high solubility and residence time.

### *3.4.3 Nd isotopes, a proxy for provenance change*

Presented in Table 5 is Sm-Nd isotopic whole rock data for all the W-IOGs sedimentary units. Wright and Basu (2024) reported 10 whole rock Lower Lava samples to define a Sm-Nd isochron with a  $3420 \pm 140$  Ma age and initial  $^{143}\text{Nd}/^{144}\text{Nd}$  ratio of  $0.50848 \pm 13$  ( $\epsilon_{\text{Nd}} = 5.7 \pm 2.5$ ; Mean Square Weighted Deviates, MSWD, 0.98). We report four of the freshest and least altered whole rock Lower Shale samples to plot on the Lower Lava isochron defining a more precise age ( $3428 \pm 103$  Ma; MSWD = 1.4) and initial  $^{143}\text{Nd}/^{144}\text{Nd}$  ratio of  $0.508472 \pm 95$  ( $\epsilon_{\text{Nd}} = 5.7 \pm 1.8$ ) (Fig. 14A). This correlation implies a genetic and synchronous relationship, where the Lower Shale was exclusively derived from the monolithic Lower Lava, in addition to suggesting a depositional model age for these first cycle sediments. This inference is consistent with the Lower Shales mafic affinities and stratigraphic position, conformably overlying the Lower Lava.

Furthermore, we selected adjacent OMTG samples ( $n = 11$ ; Fig. 14A) whose Nd data was reported by Sharma et al., 1994 to have a 3.35 Ga isochron age. Additionally, since the OMTG isochron reported by Basu et al., 1981 is suggestive to be a mixing line between a 3.5 Ga and 3.35 Ga plutonic event (see Moorbath et al., 1986), we selected the two samples (SR 581, ON1) representative of the 3.35 Ga event. Collected from the same Champua area (Fig.2), these 13 OMTG samples produce a  $3,397 \pm 140$  Ma isochron age with an initial  $^{143}\text{Nd}/^{144}\text{Nd} = 0.50834 \pm 11$  ( $\epsilon_{\text{Nd}} = 2.2 \pm 2.2$ ; MSWD = 0.3). A single tuff (IG-4/03) plots precisely within a tight cluster of OMTG samples and this isochron age is consistent with the tuff's reported  $3.39 \pm 0.02$  Ga U-Pb



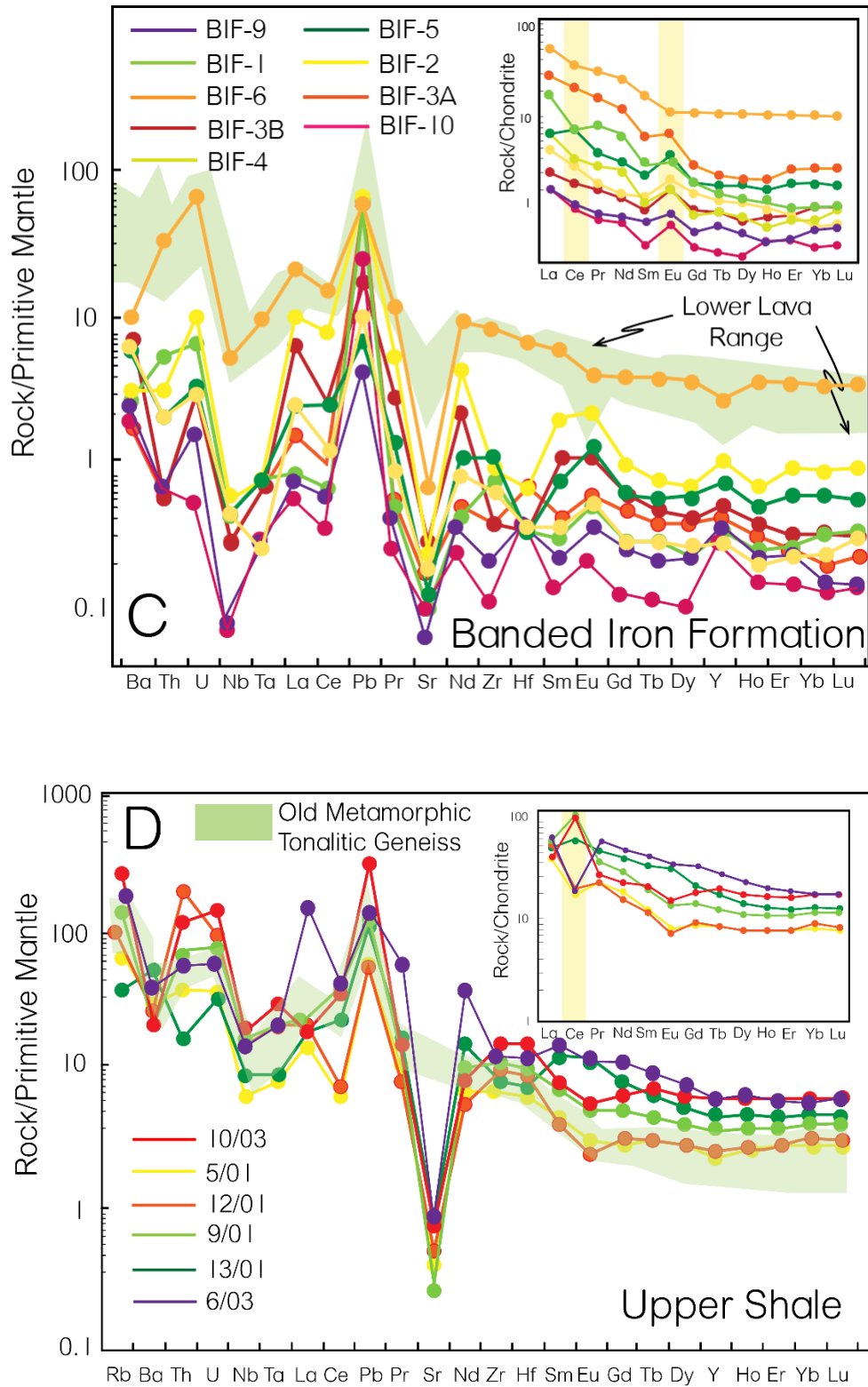


**Figure 13.** Incompatible element variation diagrams. (a) The Lower Shale mirrors the Lower Lava represented by the green field. (b) Tuffs reflect an extraneous source compared to the underlying Lower Lava and Lower Shale. (c) BIF reflects syndepositional volcanic inputs forming a mixture

between Lower Shale (i.e., Lower Lava) and ashfall tuff. The green band represents the Lower Lava range (d) Upper Shale mimics the OMTG represented by the green field. OMTG data from Sharma et al., 1994 and partially Basu et al., 1981. Primitive mantle normalization after McDonough et al., 1992. Chondrite normalization after McDonough and Sun, 1995.

zircon age. This correlation indicates a genetic relationship between the OMTG and the tuff, and is consistent with the tuff's rhyolitic affinities.

Interestingly, four of the freshest and least altered whole rock Upper Shale samples plots on this same OMTG isochron (Fig. 14A), yielding a more precise age ( $3365 \pm 96$  Ma; MSWD = 0.74) and initial  $^{143}\text{Nd}/^{144}\text{Nd}$  ratio of  $0.508370 \pm 75$  ( $\epsilon_{\text{Nd}} = 2.2 \pm 1.6$ ). Despite these 13 OMTG samples all registering the same approximate 3.35 Ga depleted mantle model ages (depleted mantle model ages,  $T_{\text{DM}}$ , defined in equation 13), and all being closely collected from the same Champua outcrop area, this isochron may represent a mixing line between a 3.39 Ga and 3.35 Ga magmatic event. However, this is difficult to evaluate given the paucity of reliable Nd data for Singhbhum Granitoids (see Wright and Basu, 2024). Nevertheless, this isochron model age agrees with the narrow range of depleted mantle model ages exhibited by the four Upper Shale samples ( $T_{\text{DM}} = 3.35 \pm 0.08$  Ga), which is also remarkably similar to the  $3368 \pm 8$  Ma Bonai Granite (Asokan et al., 2021) that intrudes into the western limb Lower Lava (Fig. 3). This suggests a genetic and synchronous relationship between the two members, implying the Upper Shale was exclusively derived from

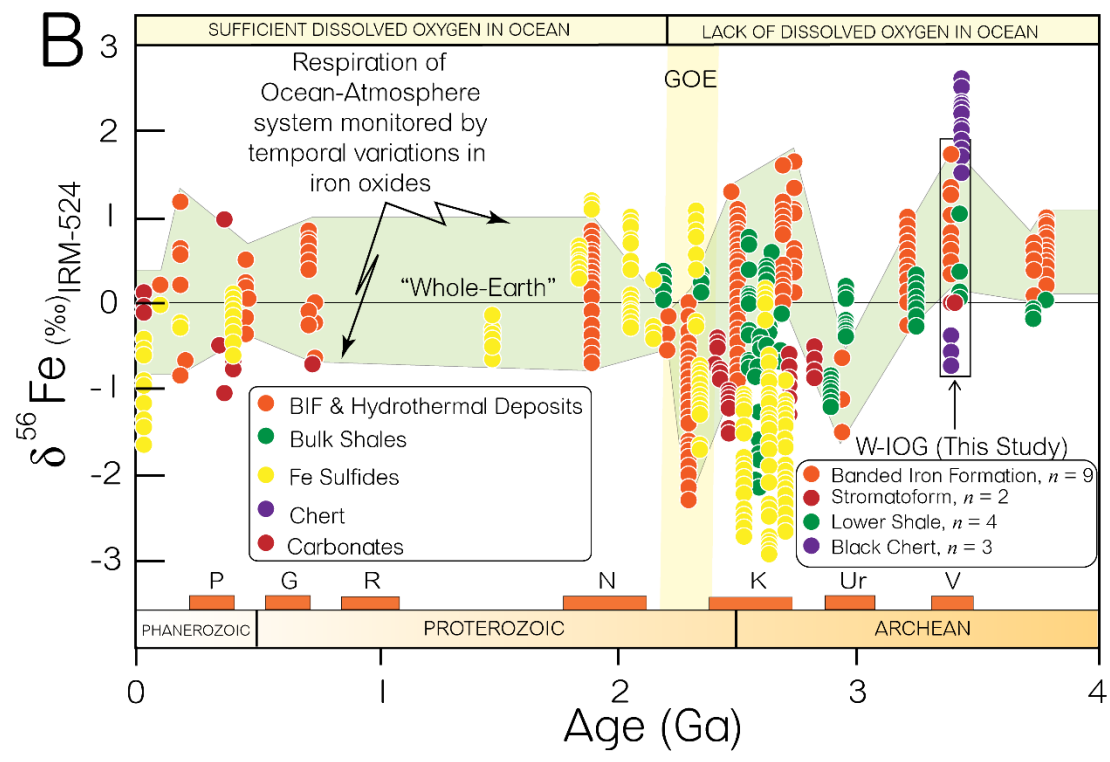
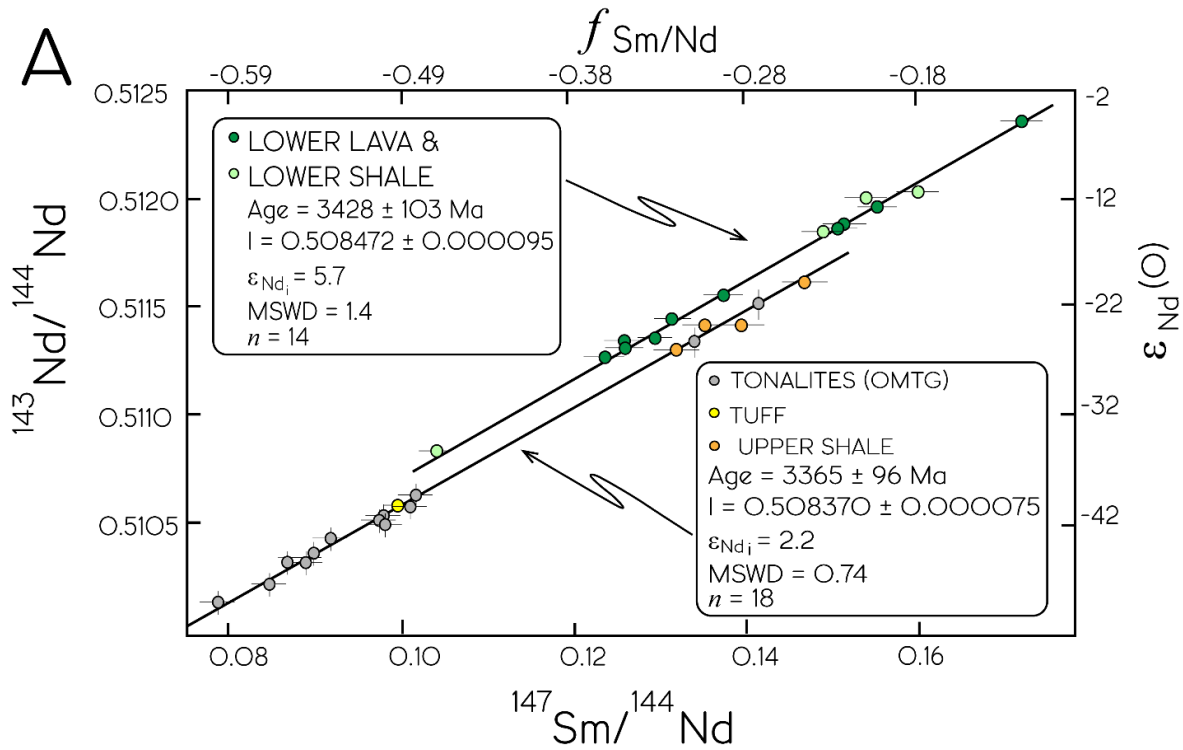


**Figure 14.** Isotope evolution diagrams for the western Iron Ore Group samples. (a) isochron diagrams showing a genetic link between the Lower Lava flood basalts and the conformably

overlying mafic Lower Shale. The tuff plots with the OMTG samples implying a genetic relationship. A parentage is also suggested between the dacitic Upper Shale and the adjacent OMTG. The horizontal error bars represent the error in the measured  $^{147}\text{Sm}/^{144}\text{Nd}$  ratio. The error in the measured  $^{143}\text{Nd}/^{144}\text{Nd}$  ratio is smaller than the symbol size. The error associated with the  $f_{\text{Sm/Nd}}$  and  $\epsilon_{\text{Nd}(0)}$  values (defined and explained in the methodology) are not expressed in this plot. (b)  $\delta^{56}\text{Fe}$  vs time diagram showing the W-IOGs coeval sedimentary rocks analyzed in this study to record the most positive BIF values and negative values (recorded by chert) for their age. Considering the stratigraphic relationship between the stromatolites and black chert interlayered in the BIF, this  $\delta^{56}\text{Fe}$  range may support a biologically mediated signature for iron oxidation 3.38 Ga ago. The “whole-Earth” line represents the bulk  $\delta^{56}\text{Fe}$ .  $\delta^{56}\text{Fe}$  is defined and explained in the methodology. Data from Ye et al., 2017; White et al., 2018 and references therein.

the monolithic OMTG, as well as providing a depositional model age for these first cycle sediments. This inference is also consistent with the Upper Shales dacitic affinity and the OMTGs geographic position, boarding the eastern limb of the basin.

Lastly, we report Nd data on four whole rock BIF samples and suggest that their broad range (initial  $\epsilon_{\text{Nd}} = 1.6$  to  $4.1$  at  $3.39$  Ga) indicates either (1) the water column was stratified in Nd due to a poorly mixed, restricted basin, (2) is a mixture between the slightly depleted tuffs ( $\epsilon_{\text{Nd}} = +2$ ) and highly depleted Lower Lava ( $\epsilon_{\text{Nd}} = +5.7$ ), (3) Nd may have been heterogeneously leached from the Lower Shale assuming the Lower Shale was replaced to form the BIF, or (4) is the result of diagenesis.

#### *3.4.4 Iron isotopes, a proxy for changes in oxidation*

Reported in Table 6 is one of the largest  $\delta^{56}\text{Fe}$  ranges (2.4 ‰) for a suite of cogenetic whole rock samples of Paleoproterozoic age (Fig. 14B). While ten BIF samples were collected extensively throughout the basin, organic-carbon bearing black cherts and silica-carbonate stromatolites intercalated with BIF strata (Shuckla et al., 2020) were sampled at high-stratigraphic fidelity at

the Kasia Mine near Barbil (Fig. 3). The Lower Shale and BIF exhibit all positive  $\delta^{56}\text{Fe}$  values ( $0.13 \text{ ‰} \leq \delta^{56}\text{Fe} \leq 1.7 \text{ ‰}$ ; avg. 1.1,  $n = 13$ ), implying large pools of  $\text{Fe}^{2+}$  were only partially oxidized to  $\text{Fe}^{3+}$  within seawater. The black cherts exhibit a negative  $\delta^{56}\text{Fe}$  signature ( $-0.69 \text{ ‰} \leq \delta^{56}\text{Fe} \leq -0.34 \text{ ‰}$ ; avg. -0.52,  $n = 3$ ), and represent the most negative  $\delta^{56}\text{Fe}$  values reported for their Paleoproterozoic age. Lastly, two stromatolite samples produced near zero  $\delta^{56}\text{Fe}$  values (0.02 and 0.05 ‰) suggesting near-complete oxidation. These results are consistent with modern microbialites (Hohl and Viehmann, 2021).

### 3.5 Discussion

This data set suggests a possible sequence of events leading to the origin of the W-IOGs BIF (Fig. 15A-D), beginning with subaerial weathering of the Lower Lava to produce the iron-rich Lower Shale. Despite the uncertainties associated with the measured ages and stratigraphic thicknesses, estimates of depositional rates are provided herein. Bracketed by the 3.42 Ga Lower Lava and the 3.39 Ga tuff, the 2 km thick Lower Shale implies a rapid depositional rates and vertical aggradation of  $\sim 66 \text{ m/Myr}$ , a likely consequence of rapid uplift of interlands and subsidence within the basin. The 3.39 Ga tuff horizon represents an ashfall deposit akin to the OMTG suite. This depositional age coincides with widespread siliceous volcanism in Singhbhum (e.g., Chaudhuri et al., 2022).

The W-IOGs BIF has long been suspected to be volcanogenic based on field observations (e.g., Dunn, 1935; Prasad et al., 2022) despite a lack of convincing geochemical evidence. We suggest the BIF to be a mixing product between the Lower Shale (i.e., Lower Lava) and tuffs. Other mixing relations can be ruled out based on the stratigraphic positions of the three units. If the Upper Shale was exclusively derived from the OMTG as our data suggests, then it implies the 3 km thick Lower Lava flood basalts were rapidly unroofed for the Upper Shale to become exclusively sourced from the OMTG. This scenario may provide a credible explanation for why

the Lower Shale is remarkably ferruginous, the BIF prodigious, and the Upper Shale comparatively iron deficient. Bracketed by the 3.39 Ga tuff and the 3.36-3.35 Ga Upper Shale, we propose the depositional rate for the >220 m thick BIF to be 5 to 7 m/Myr. Similar depositional rate estimates were made in Lantink et al., 2022 for the Brockman Iron Formation, Australia.

While it is not clear whether the BIF in W-IOG originated from secondary replacement of iron from the Lower Shale, or there was simply an abundance of dissolved  $\text{Fe}^{2+}$  leftover in seawater to precipitate out of solution as a ferric ( $\text{Fe}^{3+}$ ) phase, the prerequisite of the Lower Lava weathering is undeniable as a result of the compilation of the presented geochemical dataset. This result is significant as previous studies (e.g., Isey, 1995; Isey and Abbott, 1999; Barley et al., 1997) only reported temporal and spatial relationships between flood basalts and BIFs assuming causality. Furthermore, the 3.42 Ga age of the Lower Lava, 3.39 Ga age of the tuff, and 3.36 Ga age of the Upper Shale all coincide with major periods of volcanism and crustal formation as revealed by Singhbhum's zircon record (e.g., Mukhopadhyay and Matin, 2020), implying that the origin of the W-IOG BIF can be partially attributed to pulses of orogenesis, a feature that may characterize all BIFs (e.g., Yin et al., 2023).

The oxidation mechanism of iron, however, is more speculative than definitive. Preliminary studies have reported stromatolites in the Lower Shale as well as the BIF (e.g., Shuckla et al., 2020; Avasthy, 1980; Grant et al., 1980). With the Lower Shale being a fertile siliciclastic-volcaniclastic source of bioavailable nutrients (e.g., Fe, P), it seems reasonable to hypothesize that the formation of the Lower Shale influenced the growth and activity of oxidizing bacteria (e.g., Maisch et al., 2016). This inference is consistent with that

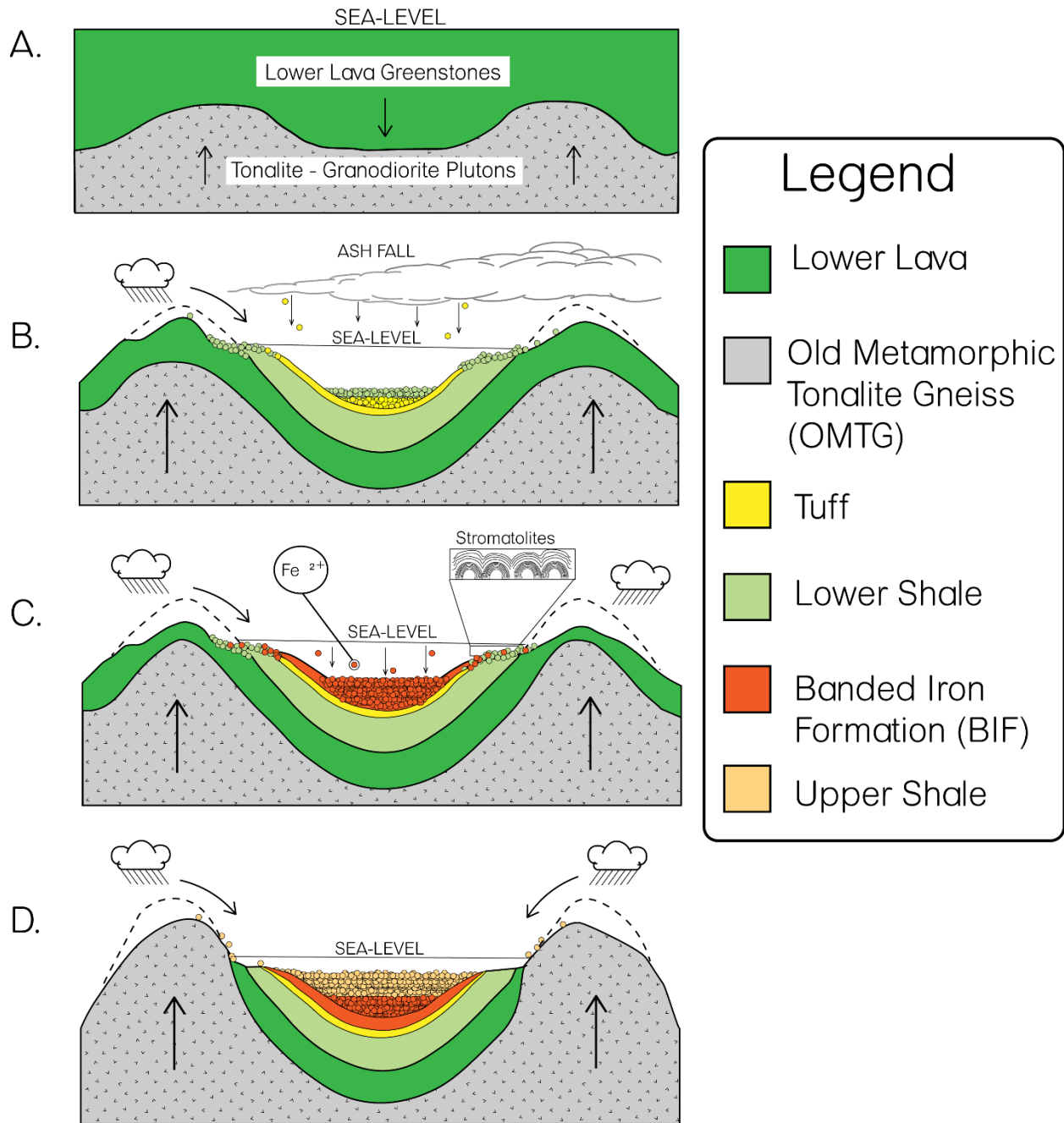


**Figure 15.** Autochthonous inheritance model for the origin of the sedimentary units from the western Iron Ore Group horseshoe syncline. Schematic diagrams (not to scale) illustrate this studies inference for the origin of the BIF and associated shales. We suggest 3 kms of Lower Lava flood basalts were unroofed rapidly to form the ferruginous Lower Shale. Either the Lower Shale was replaced by hydrothermal leaching of iron and silica to form the BIF, or sufficient ferrous iron remained dissolved in seawater solution which became oxidized by stromatolites to generate the BIF. Thus, we propose that the BIF is formed by mixtures (coprecipitation) of incongruently dissolved Lower Lava while synchronously receiving silicic volcanic tuffaceous material. The data suggests that the Lower Lava was unroofed rapidly so that the Upper Shale became exclusively sourced from the younger intruding OMTG during a major crustal formation event.

reported by Tostevin and Ahmend (2023) which propose greenalite formation-controlled micronutrient availability in the Archean oceans. Our reported  $\delta^{56}\text{Fe}$  data from coeval BIF, black chert, and stromatolite samples may provide evidence for biologically mediated oxidized iron. Several studies (e.g., Li et al., 2015) have proposed that negative  $\delta^{56}\text{Fe}$  values reflect microbial dissimilatory reduction. If accurate, the reported black chert data (Fig. 14B) may represent the oldest biological processes recorded by  $\delta^{56}\text{Fe}$ . This is a plausible hypothesis considering the stratigraphic relationship between the stromatolites and black chert interlayered within the BIF.

### **3.6 Conclusion**

In summary, the entire lithological suite of the W-IOG was examined, including its relationship with the concomitant emplacement of the adjacent OMTG and invoked a genetic relationship between the unroofing of the Lower Lava flood basalts and the origin of the BIF. Sedimentation of BIF strata within the basin occurred over 60 Ma and ceased at  $\sim 3.36$  Ga. While the  $\delta^{56}\text{Fe}$  data alone cannot distinguish between the involvement of photosynthetic cyanobacteria or anoxygenic photoferrotrophic oxidizing bacteria, it appears that the biomass of the oxidant was limited.

**Table 4.** Major and trace element concentrations of the Iron Ore Group from the Eastern Indian Craton

Sample Name	Lower-Lava Eastern Limb								
	IG-6a-01	IG-6b-01	IG-6c-01*	IG-7-03*	IG-10-01*	IG-10a-01	IG-10b-01	IG-11-01	IG-9-03*
<b>Major Oxides (wt%)</b>									
SiO <sub>2</sub>	55.94	55.64	55.66	56.02	55.18	56.57	49.88	54.14	57.83
Al <sub>2</sub> O <sub>3</sub>	13.82	13.77	12.65	11.81	11.33	13.23	14.31	11.33	13.16
Fe <sub>2</sub> O <sub>3</sub>	10.91	11.08	9.59	9.72	9.42	9.27	12.77	10.28	10.56
MnO	0.13	0.11	0.14	0.16	0.11	0.13	0.18	0.16	0.15
MgO	3.14	5.41	6.31	6.49	4.19	5.99	5.06	10.21	3.62
CaO	5.22	1.49	9.48	9.79	1.94	7.52	9.4	7.12	7.96
Na <sub>2</sub> O	4.15	3.19	2.34	0.36	0.8	2.58	2.01	1.15	2.43
K <sub>2</sub> O	1.92	1.97	0.96	1.09	3.98	1.97	1.36	1.12	1.38
TiO <sub>2</sub>	1.14	1.21	0.62	0.59	0.68	0.49	1.08	0.48	0.77
P <sub>2</sub> O <sub>5</sub>	0.18	0.18	0.12	0.09	0.13	0.1	0.12	0.07	0.1
LOI	3.45	5.95	2.24	4.14	2.69	2.15	3.83	3.94	1.74
<b>Total</b>	100	100	100.09	100.26	100.45	100	100	100	99.71
<b>Trace elements (ppm)</b>									
Rb	13.8	42.39	37.54	22.41	33.09	56.96	43.55	28.6	42.62
Ba	111.89	186.88	270.6	165.05	884.47	487.81	152.96	214.1	294.31
Th	1.84	9.77	4.65	2.99	3.23	3.43	5.93	3.32	5.02
U	0.65	3.36	1.05	0.86	1.45	1.19	1.26	0.85	1.44
Nb	6.02	7.61	6.75	4.86	8.77	5.77	7.79	4.46	8.76
Ta	0.57	0.99	0.6	0.33	0.8	0.58	0.63	0.32	0.93
Pb	1.86	17.47	6.66	2.43	7.07	8.56	7.54	3.38	5.45
Sr	92.1	72.81	156.07	44.7	50.6	91.4	125.87	153.4	171.11
Zr	87.21	105.8	111.33	94.02	141.12	98.09	94.47	81.93	142.94
Hf	2.2	2.66	2.67	2.48	3.39	2.61	2.39	2.11	3.7
Y	9.66	17.65	27.33	18.5	14.65	12.37	28.8	16.82	27.42
<b>Rare Earth Elements</b>									
La	10.9	19.46	20.01	15.99	10.01	11.76	14.52	16.82	23.91
Ce	22.52	36.85	36.41	32.1	33.86	27.89	26.89	31.31	48.36
Pr	2.81	4.15	4.86	3.69	2.76	2.69	3.54	3.73	5.54
Nd	11.16	15.54	18.98	14.61	10.42	9.92	15.38	13.63	21.64
Sm	2.26	3.29	4.22	3.17	2.26	2.02	3.92	2.91	4.51
Eu	0.57	0.76	1.17	0.71	0.26	0.44	1.22	0.88	1.17
Gd	2.15	3.03	4.43	3.07	2.56	2.04	4.4	2.86	4.27
Tb	0.33	0.47	0.72	0.52	0.44	0.34	0.75	0.47	0.74
Dy	2.01	2.84	4.44	3.12	2.65	2.32	4.86	2.83	4.79
Ho	0.42	0.63	0.97	0.64	0.59	0.52	1.11	0.61	1.22
Er	1.1	1.82	2.7	1.85	1.69	1.43	3.15	1.73	2.93
Yb	1.04	1.79	2.6	1.9	1.83	1.44	2.9	1.69	2.76
Lu	0.15	0.26	0.38	0.29	0.28	0.21	0.45	0.25	0.42

All sample numbers listed in Table 4 are shown in Figure 17 without the “IG” prefix.

**Table 4.** (Continued) Major and trace element concentrations of the Iron Ore Group from the Eastern Indian Craton

Sample Name	Lower-Lavas Western Limb								
	IG-2a-01	IG-2b-01*	IG-2c-01	IG-3-01*	IG-4-01	IG-4*	IG-8	IG-2-03	IG-1-03
<b>Major Oxides (wt%)</b>									
SiO <sub>2</sub>	51.76	53.56	48.11	54.2	50.71	57.47	55.16	53.96	50.9
Al <sub>2</sub> O <sub>3</sub>	13.57	15.02	15.77	14.69	13.12	13.38	12.85	11.75	12.86
Fe <sub>2</sub> O <sub>3</sub>	9.67	9.44	8.87	9.67	9.81	11.59	9.82	12.03	11.31
MnO	0.16	0.13	0.15	0.16	0.16	0.13	0.14	0.15	0.17
MgO	8.68	5.75	8.91	5.93	8.81	3.52	7.72	6.85	9.71
CaO	8.25	8.39	10.09	10.06	8.17	6.62	7.92	7.37	8.6
Na <sub>2</sub> O	2.76	2.96	1.45	3.07	2.55	3.31	1.83	1.56	2.31
K <sub>2</sub> O	1.53	1.83	1.21	0.8	1.22	1.06	1.13	1.33	1.15
TiO <sub>2</sub>	0.57	0.74	0.38	0.54	0.57	1.03	0.58	1.04	0.86
P <sub>2</sub> O <sub>5</sub>	0.06	0.12	0.05	0.08	0.08	0.16	0.13	0.14	0.12
LOI	2.99	2.25	5.01	1.97	4.8	2.34	2.72	3.82	2.01
Total	100	100.19	100	100.5	100	100.61	100	100	100
<b>Trace Elements (ppm)</b>									
Rb	51.49	64.49	41.21	30.41	23.94	24.44	21.21	15.58	65.69
Ba	286.06	421.15	272.6	331.61	128.95	324.9	144.1	184.87	158.92
Th	3.94	3.71	3.15	3.81	2.29	4.53	3.18	2.61	1.12
U	0.81	0.79	0.55	0.85	0.44	1.24	0.98	0.47	0.24
Nb	6.42	6.82	4.85	6.18	4.24	11.74	5.56	7.18	3.21
Ta	0.55	0.55	0.42	0.55	0.33	0.82	0.41	0.41	0.19
Pb	3.06	5.3	3.02	9.49	3.55	8.48	2.78	4.07	1.19
Sr	191.77	154.72	116.64	287.46	78.25	416.9	119.9	156.72	84.67
Zr	104.95	107.51	78.39	97.6	66.58	167.5	93.39	99.76	42.21
Hf	2.65	2.48	1.95	2.45	1.67	4.38	2.48	2.46	1.13
Y	27.25	22.41	26.3	23.3	17.71	28.04	18.79	17.01	16.17
<b>Rare Earth Elements</b>									
La	17.58	14.84	14.52	17.06	12.22	25.93	15.12	15.09	14.49
Ce	31.34	30.31	25.48	29.98	23.92	56.41	32.03	30.62	31.65
Pr	4.4	3.89	3.7	4.66	4.16	7.22	4.1	3.85	3.76
Nd	18.1	13.62	14.16	18.96	13.67	28.74	11.25	15.79	8.59
Sm	3.85	3.12	3.34	4.16	3.93	6.11	2.93	3.85	2.17
Eu	1.04	1.22	0.88	1.16	1.38	1.71	1.26	1.12	0.89
Gd	4.11	4.17	3.89	4.43	3.41	5.89	3.41	3.74	3.42
Tb	0.68	0.58	0.62	0.58	0.51	0.91	0.46	0.59	0.54
Dy	4.73	4.34	4.25	4.52	2.93	5.27	4.28	3.31	3.55
Ho	1.04	1.01	0.9	0.76	0.69	1.07	0.73	0.63	0.65
Er	2.87	2.4	2.77	1.82	1.78	2.89	1.92	1.67	1.61
Yb	3.04	2.47	2.9	2.31	1.42	2.69	1.88	1.42	1.5
Lu	0.46	0.41	0.38	0.37	0.33	0.38	0.36	0.21	0.23

Fe<sub>2</sub>O<sub>3</sub>: Total Iron Content

Samples with an asterisks (\*) were analyzed at ACT Labs.

**Table 4.** (Continued) Major and trace element concentrations of the Iron Ore Group from the Eastern Indian Craton

Sample Name	Upper Lava									
	IG-15a-01*	IG-15b-01*	IG-15c-01*	IG-15d-01*	UL-1-03*	UL-2-03*	UL-3-03*	UL-4-03*	UL-5-03*	
<b>Major Oxides (wt%)</b>										
SiO <sub>2</sub>	55.59	51.43	57.27	56.38	57.1	54.55	54.92	52.99	54.93	
Al <sub>2</sub> O <sub>3</sub>	13.26	13.55	13.86	14.42	13.06	11.92	13.36	12.47	11.91	
Fe <sub>2</sub> O <sub>3</sub>	11.24	10.41	8.39	9.92	11.26	12.1	10.63	9.94	9.12	
MnO	0.15	0.16	0.12	0.14	0.14	0.15	0.15	0.14	0.16	
MgO	3.35	8.63	4.32	5.67	3.59	6.92	5.78	8.01	6.53	
CaO	8.88	8.15	11.51	5.38	7.38	7.63	6.33	7.51	13.01	
Na <sub>2</sub> O	1.9	2.16	1.14	1.24	2.1	1.53	1.99	2.28	0.27	
K <sub>2</sub> O	0.94	1.59	0.64	3.35	1.42	1.3	3.14	1.23	1.1	
TiO <sub>2</sub>	1.02	0.64	0.6	0.61	1.04	1.03	0.81	0.62	0.51	
P <sub>2</sub> O <sub>5</sub>	0.15	0.12	0.1	0.12	0.15	0.13	0.13	0.1	0.06	
LOI	3.49	3.02	2.15	3.09	2.81	2.9	2.73	4.73	3.99	
Total	99.97	99.86	100.1	100.32	100.5	100.16	99.7	100.02	100.6	
<b>Trace Elements (ppm)</b>										
Rb	32.37	54.07	49.45	120.97	35.97	70.05	152.47	46.74	52.13	
Ba	186.87	211.82	199.42	486.79	254.78	246.48	931.65	342.76	235.92	
Th	18.33	7.13	8.27	6.98	10.32	7.41	9.21	6.68	6.13	
U	5.3	3.6	3.61	3.73	3.79	2.47	3.51	2.3	0.26	
Nb	11.75	8.88	8.2	9.13	8.26	7.51	7.31	5.2	4.7	
Ta	1.93	1.19	1.13	1.28	0.81	0.63	0.68	0.49	0.48	
Pb	14.95	18.22	23.56	19.48	13.12	9.14	13.06	11.13	23.3	
Sr	64.12	75.58	71.38	163.72	65.89	113.88	101.21	74.11	72.66	
Zr	159.01	115.24	120.66	117.45	123.69	116.06	111.87	82.72	76.23	
Hf	3.99	2.78	3.24	2.96	3.38	3.19	3.08	2.32	2.17	
Y	34.41	11.19	14.51	11.94	19.88	19.11	18.3	15.18	14.67	
<b>Rare Earth Elements</b>										
La	41.8	15.09	16.52	16.95	21.36	20.44	19.59	17.14	14.7	
Ce	70.05	35.58	33.04	38.87	43.08	40.73	38.02	32.15	28.84	
Pr	9.79	3.13	3.52	3.66	4.9	4.81	4.34	3.56	3.21	
Nd	36.06	10.48	14.89	12.88	19.16	19.27	16.41	13.45	12.11	
Sm	7.5	2.48	3.13	2.51	4.11	4.22	3.24	2.71	2.56	
Eu	1.83	0.53	0.61	0.53	1.29	1.15	0.68	0.69	0.66	
Gd	6.96	2.19	2.38	2.37	3.74	4.09	3.23	2.63	2.37	
Tb	1.05	0.34	0.39	0.36	0.63	0.64	0.53	0.44	0.41	
Dy	6.2	1.83	2.5	1.94	3.55	3.56	3.18	2.65	2.52	
Ho	1.27	0.38	0.54	0.4	0.69	0.66	0.62	0.54	0.51	
Er	3.38	1.05	1.55	1.15	1.88	1.75	1.67	1.49	1.52	
Yb	3.18	1.09	1.59	1.22	1.76	1.63	1.69	1.52	1.49	
Lu	0.46	0.15	0.24	0.18	0.22	0.25	0.26	0.24	0.22	

Fe<sub>2</sub>O<sub>3</sub>: Total Iron Content

Samples with an asterisks (\*) were analyzed at ACT Labs.

**Table 4 (Continued)** Major and trace element concentrations of the Western-Iron Ore Group, Singhbhum Cra

<b>Lower-Shale</b>							
Sample Name	IG-1a-01	IG-1b-01	IG-1-95	IG-12d-03	IG-12e-03	IG-13-03	IG-5-03
<b>Major Oxides (wt%)</b>							
SiO <sub>2</sub>	49.54	46.88	52.57	55.32	60.1	52.92	56.8
Al <sub>2</sub> O <sub>3</sub>	18.51	16.12	11.15	14.56	11.6	19.67	13.73
Fe <sub>2</sub> O <sub>3</sub>	16.06	24.68	20.74	21.33	15.37	12.08	17.62
MnO	0.064	0.08	0.23	0.05	0.044	0.004	0.157
MgO	3.38	4.98	2.03	3.46	2.71	0.39	0.02
CaO	0.03	0.02	0.52	0.01	0.35	0.03	0.07
Na <sub>2</sub> O	0.05	0.05	0.03	0.02	0.01	0.29	0.02
K <sub>2</sub> O	3.73	1.13	1.19	1.54	1.4	4.98	2.01
TiO <sub>2</sub>	1.87	1.23	2.04	1.02	1.58	3.04	2.43
P <sub>2</sub> O <sub>5</sub>	0.07	0.08	0.06	0.05	0.05	0.07	0.04
LOI	7.4	4.81	10.13	2.99	7.8	5.49	7.7
Total	100.7	100.06	100.7	100.35	99.61	98.96	100.59
<b>Trace elements (ppm)</b>							
Rb	164.1	64.35	4.76	0.34	0.29	145.77	1.49
Ba	309.67	116.56	32.89	3.45	61.41	355.68	84.63
Th	4.48	2.58	5.84	0.36	0.36	0.96	2.52
U	1.44	0.72	1.98	0.42	0.42	0.24	1.16
Nb	10.21	7.65	4.55	1.54	6.34	17.3	8.82
Ta	0.77	0.47	0.41	0.05	0.37	1.11	0.66
Pb	2.42	2.08	21.75	1.42	2.83	5.09	6.14
Sr	10.28	4.09	73.15	0.72	11.28	29.97	5.27
Zr	195.46	107.29	72.54	15.06	68.56	271.03	213.11
Hf	4.94	2.54	1.96	0.45	1.99	7.69	5.16
Y	24.53	23.36	13.36	2.36	31.83	24.69	15.89
<b>Rare Earth Elements</b>							
La	13.91	6.08	15.36	3.43	16.73	13.93	6.65
Ce	27.47	12.39	28.79	5.65	13.59	28.03	47.84
Pr	3.61	1.61	3.17	0.83	0.42	4.98	2.3
Nd	14.88	6.41	12.08	3.62	23.44	13.16	10.21
Sm	3.29	1.72	2.59	0.86	6.32	3.24	2.71
Eu	0.8	0.45	0.71	0.29	2.01	0.93	0.69
Gd	3.64	1.74	2.43	1.05	7.08	3.61	2.48
Tb	0.69	0.31	0.39	0.22	1.15	0.74	0.46
Dy	4.25	2.08	2.27	1.27	6.11	4.62	2.87
Ho	0.96	0.49	0.46	0.25	1.2	1.06	0.64
Er	2.95	1.45	1.27	0.69	3.11	3.52	2.25
Yb	3.03	1.63	1.3	0.66	2.79	4.45	3.24
Lu	0.45	0.24	0.2	0.09	0.39	0.71	0.65
REE	79.93	36.6	71.02	18.91	84.34	82.98	82.99
<b>Significant Ratios</b>							
(La/Yb) <sub>2</sub>	3.12	2.53	8.03	3.53	4.07	2.12	1.39
(La/Sm) <sub>2</sub>	2.64	2.2	3.7	2.49	1.65	2.68	1.53
(Gd/Lu) <sub>2</sub>	1	0.89	1.5	1.44	2.24	0.62	0.47
Eu/Eu*	0.7	0.79	0.86	0.93	0.91	0.82	0.81
Ce/Ce*	0.93	0.95	0.99	0.81	1.24	0.81	2.96

**Table 4 (Continued)**

<b>Banded Iron Formation</b>										
Sample Name	BIF-1	BIF-2	BIF-3A	BIF-3B	BIF-4	BIF-5	BIF-6	BIF-8	BIF-9	BIF-10
<b>Major Oxides (wt%)</b>										
SiO <sub>2</sub>	50.94	42.8	47.3	46.99	37.37	12.78	69.32	14.64	61.38	67.6
Al <sub>2</sub> O <sub>3</sub>	0.31	0.22	0.37	0.34	0.32	0.68	7.18	0.74	0.09	0.05
Fe <sub>2</sub> O <sub>3</sub>	46.79	56.33	51	50.9	61.77	84.55	19.61	82.56	36.22	30.43
MnO	0.015	0.014	0.027	0.022	0.021	0.021	0.014	0.022	0.014	0.011
MgO	0.02	0.02	0.02	0.04	0.06	0.03	0.11	0.04	0.05	0.02
CaO	0.03	0.01	0.02	0.02	0.04	0.02	0.19	0.02	0.08	0.03
Na <sub>2</sub> O	0.01	0.02	0.02	0.04	0.03	0.01	0.13	0.03	0.01	0.01
K <sub>2</sub> O	0.02	0.03	0.01	0.01	0.02	0.02	0.42	0.02	0.01	0.01
TiO <sub>2</sub>	0.021	0.015	0.074	0.057	0.079	0.044	0.737	0.064	0.009	0.002
P <sub>2</sub> O <sub>5</sub>	0.03	0.02	0.05	0.01	0.01	0.06	0.03	0.06	0.05	0.03
LOI	0.32	0.23	0.14	0.13	0.2	2.65	3.13	2.14	0.88	0.77
Total	98.506	99.709	99.031	98.559	99.92	100.865	100.871	100.33	98.77	98.95
<b>Trace elements (ppm)</b>										
Rb	N/A	N/A	N/A	N/A	N/A	N/A	N/A	N/A	N/A	N/A
Ba	50.12	12.14	22.49	19.22	41.67	41.33	73.19	37.88	16.04	12.09
Th	0.05	0.05	0.27	0.46	0.17	0.18	2.97	0.16	0.05	0.05
U	0.06	0.07	0.22	0.14	0.06	0.07	0.94	0.12	0.03	0.01
Nb	0.2	0.2	0.4	0.3	0.3	0.3	3.7	0.2	0.02	0.02
Ta	0.03	0.03	0.03	0.03	0.01	0.03	0.4	0.03	0.01	0.01
Pb	3.45	2.23	2.78	1.34	0.68	0.62	4.67	4.22	0.35	1.9
Sr	6.17	3.52	4.19	2.19	3.06	2.16	14.09	3.01	3.01	3.17
Zr	4.22	4.38	10.47	8.17	7.49	12.31	95.55	11.71	2	1
Hf	0.1	0.2	0.2	0.1	0.1	0.1	2.1	0.1	0.1	0.1
Y	2.2	1.8	4.6	1.3	1.3	3.3	12.3	2.9	1.4	1.1
<b>Rare Earth Elements</b>										
La	4.49	1.03	7.24	0.58	1.67	1.67	15.3	1.78	0.45	0.34
Ce	4.56	1.8	14.1	1.14	2.15	4.51	26.7	4.66	0.92	0.53
Pr	0.78	0.16	1.56	0.14	0.27	0.38	3.32	0.55	0.1	0.06
Nd	2.93	0.63	5.92	0.56	1.14	1.42	12.9	1.38	0.42	0.27
Sm	0.45	0.18	0.9	0.13	0.16	0.32	2.67	0.36	0.08	0.05
Eu	0.182	0.106	0.379	0.085	0.085	0.205	0.668	0.11	0.05	0.03
Gd	0.36	0.28	0.58	0.17	0.16	0.37	2.28	0.28	0.13	0.06
Tb	0.05	0.04	0.08	0.03	0.03	0.06	0.4	0.04	0.02	0.01
Dy	0.29	0.26	0.49	0.16	0.17	0.42	2.72	0.22	0.14	0.06
Ho	0.06	0.05	0.11	0.04	0.03	0.08	0.58	0.07	0.03	0.02
Er	0.15	0.12	0.42	0.12	0.11	0.28	1.71	0.23	0.1	0.06
Yb	0.15	0.09	0.42	0.16	0.11	0.28	1.66	0.27	0.06	0.05
Lu	0.023	0.015	0.067	0.024	0.022	0.04	0.256	0.033	0.008	0.008
REE	14.475	4.761	32.266	3.339	6.107	10.035	71.164	9.983	2.508	1.548
<b>Significant Ratios</b>										
(La/Yb) <sub>2</sub>	20.33	7.77	11.74	2.45	10.31	4.06	6.26	4.47	5.1	4.61
(La/Sm) <sub>2</sub>	6.23	3.58	5.02	2.77	6.51	3.25	3.57	3.09	3.5	4.33
(Gd/Lu) <sub>2</sub>	1.93	2.31	1.06	0.87	0.89	1.11	1.1	1.04	2.03	0.93
Eu/Eu*	1.37	1.44	1.59	1.74	1.61	0.75	0.82	1.05	0.40	1.70
Ce/Ce*	0.58	1.07	1.01	0.96	0.77	1.36	0.9	1.13	1.15	0.86

Fe<sub>2</sub>O<sub>3</sub>\*: Total Iron Content

**Table 4 (Continued)**

Sample Name	Upper-Shale						Tuff	
	IG-10-03	IG-5-01	IG-9-01	IG-12-01	IG-13-01	IG-6-03	IG-4-03	IG-3-03
<b>Major Oxides (wt%)</b>								
SiO <sub>2</sub>	66.31	67.36	61.54	65.86	64.12	74.35	85.62	93.46
Al <sub>2</sub> O <sub>3</sub>	16.22	16.76	19.72	14.61	17.39	14.51	8.33	3.62
Fe <sub>2</sub> O <sub>3</sub>	7.8	6.32	7.85	9.48	7.43	1.54	0.09	0.96
MnO	0.017	0.002	0.005	0.005	0.005	0.005	0.0009	0.009
MgO	0.59	0.63	0.48	0.58	0.61	0.73	0.04	0.07
CaO	0.01	0.03	0.02	0.07	0.03	0.05	0.02	0.01
Na <sub>2</sub> O	0.05	0.05	0.06	0.09	0.06	0.03	0.02	0.04
K <sub>2</sub> O	3.45	2.41	3.6	1.73	3.2	3.35	1.75	1.06
TiO <sub>2</sub>	1.39	0.59	1.7	0.61	1.3	1.34	0.33	0.128
P <sub>2</sub> O <sub>5</sub>	0.01	0.04	0.04	0.06	0.04	0.05	0.06	0.01
LOI	4.74	5.56	5.89	5.53	5.49	4.35	1.68	1.08
Total	100.58	99.75	100.9	98.62	99.67	100.3	98.19	100.44
<b>Trace elements (ppm)</b>								
Rb	177.37	67.12	90.89	45.86	25.09	124.22	57.4	28.67
Ba	198.54	206.1	166.47	214.41	387.65	294.7	60.52	145.17
Th	10.18	16.39	6.12	3.34	1.44	5.46	220.99	7.94
U	3.09	2.17	1.69	0.8	0.69	1.53	12.7	2.01
Nb	13.54	10.56	10.71	4.67	6.71	7.30	7.65	1.84
Ta	1.24	0.91	0.91	0.35	0.4	0.81	0.74	0.21
Pb	22.15	3.95	9.29	3.99	7.7	11.72	43.24	9.22
Sr	6.36	11.36	9.53	9.52	17.33	13.34	30.31	8.64
Zr	188.15	107.95	131.11	82.54	99.62	142.63	237.88	63.45
Hf	5.02	2.77	3.25	2.14	2.37	3.62	7.12	4.17
Y	28.03	11.94	16.7	10.68	20.63	96.8	53.46	12.27
<b>Rare Earth Elements</b>								
La	10.8	14.58	16.11	10.34	13.28	85.9	659.99	32.26
Ce	67.38	13.7	72.77	11.78	41.9	74.3	1180.65	49.51
Pr	2.91	2.37	3.84	2.41	4.77	14.8	114.92	6.14
Nd	11.64	7.97	14.2	9.27	20.72	49.1	408.18	20.43
Sm	3.49	1.93	3.29	2.07	5.47	9.47	77.83	3.79
Eu	0.94	0.45	0.86	0.51	1.96	2.47	4.24	0.58
Gd	4.03	2.03	3.17	1.94	4.8	10.8	46.03	2.75
Tb	0.8	0.35	0.5	0.34	0.72	1.95	4.84	0.41
Dy	4.81	2.17	3.05	2.12	3.94	12.6	16.78	2.56
Ho	1.01	0.46	0.65	0.47	0.80	2.78	2.22	0.46
Er	2.91	1.35	1.88	1.36	2.22	7.55	4.35	1.36
Yb	3.11	1.62	2.13	1.47	2.35	5.75	3.01	1.32
Lu	0.48	0.23	0.32	0.21	0.35	0.93	0.42	0.21
REE	114.31	49.21	122.77	44.29	102.48	278.4	2523.46	121.78
<b>Significant Ratios</b>								
(La/Yb) <sub>2</sub>	2.36	6.11	5.14	4.77	3.84	10.13	146.96	16.6
(La/Sm) <sub>2</sub>	1.93	4.71	3.05	3.12	1.58	5.66	5.22	5.31
(Gd/Lu) <sub>2</sub>	1.03	1.09	1.22	1.14	1.77	1.43	13.55	1.61
Eu/Eu*	0.67	0.69	0.81	0.77	1.18	0.59	0.22	0.55
Ce/Ce*	2.95	0.57	2.27	0.58	1.31	0.5	1.06	0.87

**Table 5** Sm-Nd isotopic data on the W-IOG sedimentary units of the Singhbhum Craton

	<b>Sample</b>	<b>Lithology</b>	Sm (p.p.m)	Nd (p.p.m)	$^{147}\text{Sm}/^{144}\text{Nd} \pm 2\sigma$	$^{143}\text{Nd}/^{144}\text{Nd} \pm 2\sigma$
<u>Lower Shale</u>	IG-1-95	Fe-Shale	2.49	14.12	0.1047 ± 09	0.510854 ± 09
	IG-5-03	Fe-Shale	2.68	10.36	0.1549 ± 10	0.512031 ± 04
	IG-12e-03	Fe-Shale	6.32	23.44	0.1596 ± 09	0.512050 ± 08
	IG-13-03	Fe-Shale	3.24	13.16	0.1488 ± 10	0.511858 ± 07
<u>Tuff</u>	IG-4-03	Air Fall Tuff	77.83	450.18	0.0996 ± 05	0.510588 ± 05
<u>Banded Iron Formatic</u>	BIF-2	BHJ	0.17	0.72	0.1438 ± 12	0.511603 ± 05
	BIF-5	BHJ	0.33	1.38	0.1473 ± 13	0.511612 ± 05
	BIF-6	BHJ	2.72	11.29	0.1483 ± 13	0.511677 ± 05
	BIF-8	BHJ	0.34	1.46	0.1418 ± 12	0.511620 ± 08
<u>Upper Shale</u>	IG-5-01	Red Shale	1.88	8.06	0.1392 ± 11	0.511412 ± 08
	IG-9-01	Banded Shale	3.22	14.61	0.1351 ± 11	0.511418 ± 07
	IG-12-01	Red Shale	2.07	9.27	0.1319 ± 11	0.511311 ± 07
	IG-13-01	Fe-Shale	6.74	27.6	0.1469 ± 12	0.511615 ± 06

\*Sm and Nd concentration data were determination by ICP-MS.

\*The Sm-Nd systematics in this study were carried out on MC-ICP-MS by Abdelmouhcine at CNRS, France.

All sample numbers listed in Table 5 are shown in Figure 17 without the “IG” prefix.

**Table 6** Fe isotopic data on the W-IOG sedimentary units of the Singhbhum Craton

Sample		$\delta^{56}\text{Fe}$ (‰)	$\delta^{57}\text{Fe}$ (‰)		$\delta^{56}\text{Fe}$ (‰)	2SD (‰)	$\delta^{57}\text{Fe}$ (‰)	2SD (‰)
BIF-1	Run#1	0.820	1.148	BIF-1	0.803	0.032	1.137	0.021
	Run#2	0.787	1.127					
	Run#3	0.804	1.137					
BIF-2	Run#1	1.004	1.510	BIF-2	1.023	0.040	1.475	0.062
	Run#2	1.023	1.460					
	Run#3	1.044	1.454					
BIF-3A	Run#1	1.360	2.044	BIF-3A	1.355	0.018	2.014	0.051
	Run#2	1.360	1.998					
	Run#3	1.344	2.001					
BIF-3B	Run#1	1.228	1.876	BIF-3B	1.240	0.025	1.891	0.046
	Run#2	1.253	1.917					
	Run#3	1.240	1.880					
BIF-4	Run#1	0.677	1.089	BIF-4	0.699	0.041	1.082	0.057
	Run#2	0.717	1.107					
	Run#3	0.705	1.051					
BIF-5	Run#1	0.306	0.506	BIF-5	0.306	0.001	0.486	0.035
	Run#2	0.307	0.474					
	Run#3	0.305	0.479					
BIF-6	Run#1	1.753	2.556	BIF-6	1.735	0.041	2.541	0.026
	Run#2	1.713	2.531					
	Run#3	1.738	2.538					
BIF-9	Run#1	0.632	0.777	BIF-9	0.603	0.052	0.783	0.016
	Run#2	0.581	0.792					
	Run#3	0.595	0.779					
BIF-10	Run#1	0.467	0.684	BIF-10	0.449	0.041	0.659	0.044
	Run#2	0.427	0.642					
	Run#3	0.454	0.650					
1a-01	Run#1	0.300	0.425	1a-01	0.323	0.041	0.403	0.039
	Run#2	0.340	0.390					
	Run#3	0.329	0.393					
1b-01	Run#1	0.364	0.526	1b-01	0.360	0.009	0.544	0.044
	Run#2	0.355	0.537					
	Run#3	0.360	0.569					
12d-01	Run#1	1.047	1.502	12d-01	1.043	0.008	1.516	0.028
	Run#2	1.039	1.530					
	Run#3	1.043	1.515					
5/03	Run#1	0.126	0.193	5/03	0.132	0.011	0.188	0.012
	Run#2	0.137	0.182					
	Run#3	0.133	0.189					
ST-1	Run#1	0.027	0.043	ST-1	0.024	0.007	0.041	0.004
	Run#2	0.020	0.039					
	Run#3	0.023	0.041					
ST-7	Run#1	0.044	0.080	ST-7	0.059	0.026	0.096	0.028
	Run#2	0.069	0.106					
	Run#3	0.063	0.102					
BC-1	Run#1	-0.712	-1.032	Ch-1	-0.693	0.034	-1.008	0.046
	Run#2	-0.679	-0.987					
	Run#3	-0.689	-1.004					
BC-2	Run#1	-0.322	-0.438	Ch-2	-0.341	0.043	-0.454	0.036
	Run#2	-0.364	-0.473					
	Run#3	-0.337	-0.45					
BC-3	Run#1	-0.521	-0.681	Ch-3	-0.546	0.048	-0.701	0.047
	Run#2	-0.569	-0.727					
	Run#3	-0.548	-0.696					
IFG	Run#1	0.660	1.016	IFG	0.646	0.045	0.997	0.035
	Run#2	0.621	0.982					
	Run#3	0.634	1.007					
	Run#4	0.669	0.982					
BCR2	Run#1	0.093	0.139	BCR2	0.097	0.019	0.144	0.027
	Run#2	0.087	0.129					
	Run#3	0.101	0.149					
	Run#4	0.109	0.160					

## CHAPTER 4

### WILSON CYCLE TIMESCALES AND COOL CLIMATE CONDITIONS INFERRED FROM SANDSTONES ALONG THE ARCHEAN-PROTEROZOIC TIME BOUNDARY

#### 4.1 Abstract

The evolution of the continents experienced a dramatic transition along the Archean-Proterozoic time boundary ( $2.5 \pm 0.2$  Ga; APTB). Their primary crustal architecture, for example, transitions from being cratons characterized by thick depleted mantle keels and dome and basin crustal architecture, to the formation of modern continental crust. Additionally, marine successions transition from being predominantly deep to shallow water deposits globally, indicating the continents attained a permanent freeboard relative to sea level. However, it remains unknown what role cratons played, if any, in the formation of Proterozoic continental crust as well as the mechanism(s) responsible for that crustal transition. The current study reports new zircon (U-Pb, Hf, O) isotopic data from a suite of Paleoproterozoic sandstones, known as the Birtola Formation, that borders the Singhbhum Craton in Eastern India. Their  $^{207}\text{Pb}/^{206}\text{Pb}$  crystallization ages predominantly cluster between 2.4 to 2.6 Ga, with the youngest concordant zircon suggesting a maximum depositional age of  $\sim 2.3$  Ga. In contrast, these zircons report Hf  $T_{\text{DM}}$  model ages that cluster between 2.7 to 3.2 Ga. Average crustal residence ages are reported based on the difference between the U-Pb zircon crystallization ages and the Hf  $T_{\text{DM}}$  model ages. The results provide a range of characteristic times for average crustal residence between 200 to 500 million years, which suggests a timescale comparable to a Wilson Cycle. This indicates a significant period of crustal growth during the late Archean to Paleoproterozoic, as well as the reworking of ancient crust potentially during the formation of the Singhbhum Mobile Belt. Therefore, the formation of Paleoproterozoic continental crust appears to be strongly linked to

the recycling of Archean cratonic material, and it may have occurred due to modern-like plate tectonics. Further examination of these zircons may support this interpretation. We report a population of low- $^{18}\text{O}$  zircons ( $-6.3 \leq \delta^{18}\text{O} \leq 4.7 \text{ ‰}$ ; avg =  $2.4 \text{ ‰}$ ,  $n = 16$ ) to exhibit an average Mesoproterozoic Hf  $T_{\text{DM}}$  model age of  $3.1 \pm 0.2 \text{ Ga}$ , all of which preserve reworked Hf signatures ( $-28.7 \leq \varepsilon_{\text{Hf}} \leq 5.1 \text{ ‰}$ ; avg =  $-5.4 \text{ ‰}$ ,  $n = 16$ ). Collectively, this zircon population suggests evolving from an older  $> 3.1 \text{ Ga}$  igneous protolith that partially melted a low- $^{18}\text{O}$  source, most plausibly within a continental rift (extensional) tectonic setting. In contrast, a population of high- $^{18}\text{O}$  “supracrustal” zircons ( $6.1 \leq \delta^{18}\text{O} \leq 7.8 \text{ ‰}$ ; avg =  $6.4 \text{ ‰}$ ,  $n = 16$ ) exhibits a much younger average Neoproterozoic Hf  $T_{\text{DM}}$  model age of  $2.8 \pm 0.1 \text{ Ga}$ , and strongly diluted reworked signatures ( $-6.5 \leq \varepsilon_{\text{Hf}} \leq 2.2 \text{ ‰}$ ; avg =  $-0.4 \text{ ‰}$ ,  $n = 17$ ). This high- $^{18}\text{O}$  population likely evolved from a much younger  $2.8 \text{ Ga}$  igneous protolith that became reworked and incorporated high- $^{18}\text{O}$  sediment into its source region upon zircon crystallization between  $2.4$  to  $2.5 \text{ Ga}$ . The most plausible tectonic setting is within a subduction zone and/or continent-continent collision setting. Furthermore, sediment transport and deposition may have occurred within cold-climatic conditions based on the presence of relatively unaltered, well-rounded to sub-rounded detrital feldspar grains. In agreement with some low- $^{18}\text{O}$  ( $< 4.7 \text{ ‰}$ ) zircons reported in this study, hydrogen isotopes ( $-98 \text{ ‰} \leq \delta D_{\text{quartz}} \leq -60 \text{ ‰}$ ; avg.  $-74 \text{ ‰}$ ,  $n = 10$ ) measured from fluid inclusions within bulk quartz samples from these sandstones also suggest a mid-latitude dependence. The Birtola sandstones represent the lowest- $^{18}\text{O}$  bulk sandstones reported to date ( $5.8 \text{ ‰} \leq \delta^{18}\text{O} \leq 8.5 \text{ ‰}$ ; avg.  $7.1 \text{ ‰}$ ,  $n = 10$ ), suggesting their detrital quartz to be little shifted from their primary igneous values. The Birtola zircon crystallization ages span the APTB and isotopic evidence from their zircons suggests a period characterized by extensive crustal reworking, tectonic extension, and tectonic shortening. This data is supported by the observation that the Birtola formation is part of a more

regionally extensive feature known as the Singhbhum Mobile Belt, which is accreted to the Singhbhum Craton, and both are separated by a regional shear zone.

## **4.2 Introduction**

The purpose of this study is to apply geochemical proxies with the potential of characterizing the provenance of the Birtola Formation, a thick sandstone-conglomerate succession deposited along the Archean-Proterozoic Time Boundary (APT<sub>B</sub>,  $2.5 \pm 0.2$  Ga). The APT<sub>B</sub> is of geologic significance because it is subjectively the most transformative period for the evolution of the continents, and encompasses an interval characterized by sustained emergence and build-up of atmospheric oxygen (The Great Oxygenation Event). A crustal hallmark from this transitional phase is the widespread replacement of thin, deep-marine sedimentary successions starved of terrigenous input, with the deposition of thick, shallow-marine clastic sedimentary sequences which resemble modern continental margin sedimentary assemblages (e.g., Windley, 1977). The Birtola formation represents the first 200 meters at the base of a ~10 km thick, time-transgressive metasedimentary assemblage known as the Darjiling Group. The Darjiling Group is part of a more regionally extensive mobile belt system bordering the Singhbhum Craton with the Birtola Formation seen to partially overlie (unconformably) the 3.42 Ga Western Iron Ore Group (W-IOG) greenstone belt. Since such clastic packages serve as important repositories of early surface environments, chemical weathering, and tectonic processes, this unmetamorphosed to weakly metamorphosed setting offers a virtually unparalleled opportunity for such investigations, especially considering its lack of previous examination in these contexts.

The global occurrence of thick modern-style clastic continental margin assemblages has been postulated to be the result of continental emergence relative to sea-level due to the

stabilization of cratons (freeboard argument, see Wise, 1972; Wise, 1974; McLennan and Taylor, 1983; Armstrong, 1991; Eriksson, 1999). An explanation for the rise of the continents has been considered to result from the secular cooling of the mantle (e.g., Holder et al., 2019), crustal maturation (e.g., Valley, 2005), and the onset of Wilson-Cycle style tectonics (e.g., Bedard, 2018; Richter, 1988).

Sandstones, which are abundant in early Proterozoic successions, are dominated by detrital quartz which is the heaviest  $^{18}\text{O}$  mineralogical phase. Additionally, sandstones contain the accessory mineral zircon—which serves as a refractory geochronometer—along with experiencing excessively slow oxygen diffusion in crustal environments and through metamorphism (e.g., King et al., 1998; Peck et al., 2003). Since quartz consists of silica tetrahedrons in a framework structure, a hardness of 7 on Mohs scale for minerals, and conchoidal fracture, it has a high potential for survival in the rock cycle becoming a dominant component in clastic sediments (e.g., Blatt, 1967). Collectively, these physical and chemical characteristics preordain quartz and zircon to co-occur in relative abundance in large-scale terrains and Siliciclastic sedimentary basins. The sampling of both minerals in a sandstone represents the average provenance of sedimentary materials upon surface environments (e.g., the “watershed”) near the time of deposition (e.g., Gregory, 2003; Fedo et al., 2003).

In this contribution, zircons separated from the Birtola sandstones were analyzed for their apparent crystallization ages (U-Th and U-Pb) and isotopic compositions (Hf and O), combined with whole rock stable oxygen and stable hydrogen isotope data. Herein the petrographic characteristics to provide insight into the petrogenesis and crust-mantle heritage for the protoliths of detritus within Archean Singhbhum basin.

### 4.3 Geologic Setting

Preserved in the Northwestern district bordering the Singhbhum Craton is a regionally extensive (4000 sq. km) and thick (~10 km) metasedimentary assemblage classified as the “Darjing Group” (Fig. 16). Mahalik (1987) separated Darjing Group into three lithological formations based on an observable difference in texture, sedimentary structures, and metamorphic grade (Fig. 16). The stratigraphic sequence is represented with the chloritic sandstone-conglomerate of the Birtola Formation at the base, overlain by carbonaceous phyllites of the Kumakela Formation, and the topmost garniferous pelitic schists of the Jalda Formation (Mahalik, 1987). These lithostratigraphic units have been reported to locally unconformably overlie the Western-Iron Ore Group (3.42 to ~2.7 Ga; see Wright et al., 2023a) in the Sundargarh District, Orissa (India) and unconformably flanks the Bonai Granite (~3.37 Ga). The Birtola Formation, which represents the oldest and lowermost unit of the Darjing Group, is a ~ 2 km thick terrigenous succession and has been recognized by Mahalik (1987) and Kundu and Matin (2007) to consist of three broad lithostratigraphic members based on facies changes on variable textures and primary sedimentary structures.

The Darjing Groups Birtola Formation clastic package (Fig. 16) is comprised of three unmetamorphosed to weakly metamorphosed, sandstone-conglomerate vertical aggregation cycles. Specifically, each cycle consists of lower grading upward to coarser grained conglomerate sandstones and conglomerates, whose compositions transition from being chloritic to feldspathic. In concurrent progression are rounded to angular pebbles and cobbles of Banded-Hematite Jasper (BHJ), Banded-Hematite-Quartzite (BHQ) and granite which become increasingly embedded within the polymictic conglomerate. Included in this assemblage are primary sedimentary structures described as large-scale trough cross-beds, Hummocky cross-strata, various ripple marks and interlamination between sandstone and mudstone (Chakabarti et

al., 1998). These sedimentary structures and their architecture have been interpreted to represent shallow marine tidal flat depositional environments (Kundu and Matin, 2007) where in continental-to-marine transport was towards the northwest (Chakabarti et al., 1998).

The source of the Birtola Formation is more speculative than definitive, with mixed acid plutonic-metamorphic sources being proposed (e.g., Saha et al., 2004). A difference of opinion exists concerning the precise age of deposition for the Darjing Group and its chronological relationship with the 2.8 Ga Tamperkola Granite. Bandyopadhyay et al., (2001) suggests an intrusive relation, with the Darjing Group being deposited and metamorphosed between 3.2 and 2.8 Ga. In contrast, Chaki et al., (2005) reported that field observations suggest that the Tamperkola Granite served as the basement for Darjing Group deposition and is thus younger than 2.8 Ga. (Mazumder et al., 2012). Therefore, the age of the Birtola Formation remains unresolved but is postulated to be late Archean. The sandstone samples collected in this study represent the complete stratigraphic succession of the Birtola formation, whose exposure and location for sample collection occurred in the Patasahi, Darjing area where the Brahmani River cuts through the Darjing Group as it drains the Singhbhum Craton.

## **4.4 Materials and Methods**

### *4.4.1 Zircon preparation*

Hand-picked zircons and grains of reference zircons (Temora-2, Mud Tank and FC-1) were cast into epoxy disks, ground, and polished to expose the midsection of the grains. Cathodoluminescence (CL) imaging was conducted using a JEOL JSM6610A Analytical SEM (scanning electron microscope) in the Research School of Earth Sciences (RSES), The Australian National University (ANU), Canberra, equipped with a Robinson CL detector. The instruments

employed include SHRIMP-RG (Reverse Geometry) for U–Pb geochronology at RSES, ANU. The analytical procedures and data processing are summarized below.

Zircon U-Th-Pb isotopic analyses were carried out on the SHRIMP-RG ion microprobe. Analytical procedures are similar to those described in Williams (1998) and references therein as well as Ireland and Williams (2003). Each analysis represents six scans through the different mass stations. The Pb/U ratios were normalized relative to a value of 0.066792 for the  $^{206}\text{Pb}/^{238}\text{U}$  ratio of the reference material Temora-2, equivalent to an age of 416.8 Ma. The standard zircon OG1 (Stern et al., 2009) was also used to monitor the  $^{207}\text{Pb}/^{206}\text{Pb}$  ratio. Data were reduced using the SQUID Excel Macro of Ludwig (2001).

#### *4.4.2 Zircon oxygen isotope procedure*

Oxygen isotope ratios ( $^{18}\text{O}/^{16}\text{O}$ ) of zircons are reported in the delta ( $\delta$ ) notation and are presented in Table 7.  $\delta^{18}\text{O}$  values were determined using the SHRIMP SI ion microprobe. Analytical conditions were similar to those outlined in detail by Fu et al., (2015) and Avila et al., (2020). The locations of ion microprobe pits for oxygen isotopes were correlated, when applicable, with the SHRIMP U-Pb pits. Blocks typically of 3-5 sample analyses were bracketed with 1-2 standard analyses. Corrected  $^{18}\text{O}/^{16}\text{O}$  ratios are reported in  $\delta^{18}\text{O}$  notation, in permil variations relative to Vienna Standard Mean Ocean Water (VSMOW). All  $\delta^{18}\text{O}$  values were calibrated against standard FC-1 zircon ( $5.61 \pm 0.14\text{‰}$ , 2sd,  $n = 6$ ; J.W. Valley, unpublished data; c.f. Fu et al. 2015). Additional zircon standards Mud Tank and Temora-2 (Valley, 2003; Black et al., 2004) were also used to monitor the data quality of the SHRIMP-RG analyses. The spot-to-spot reproducibility (external precision) was typically better than  $\pm 0.90\text{‰}$  ( $2\sigma$ ).

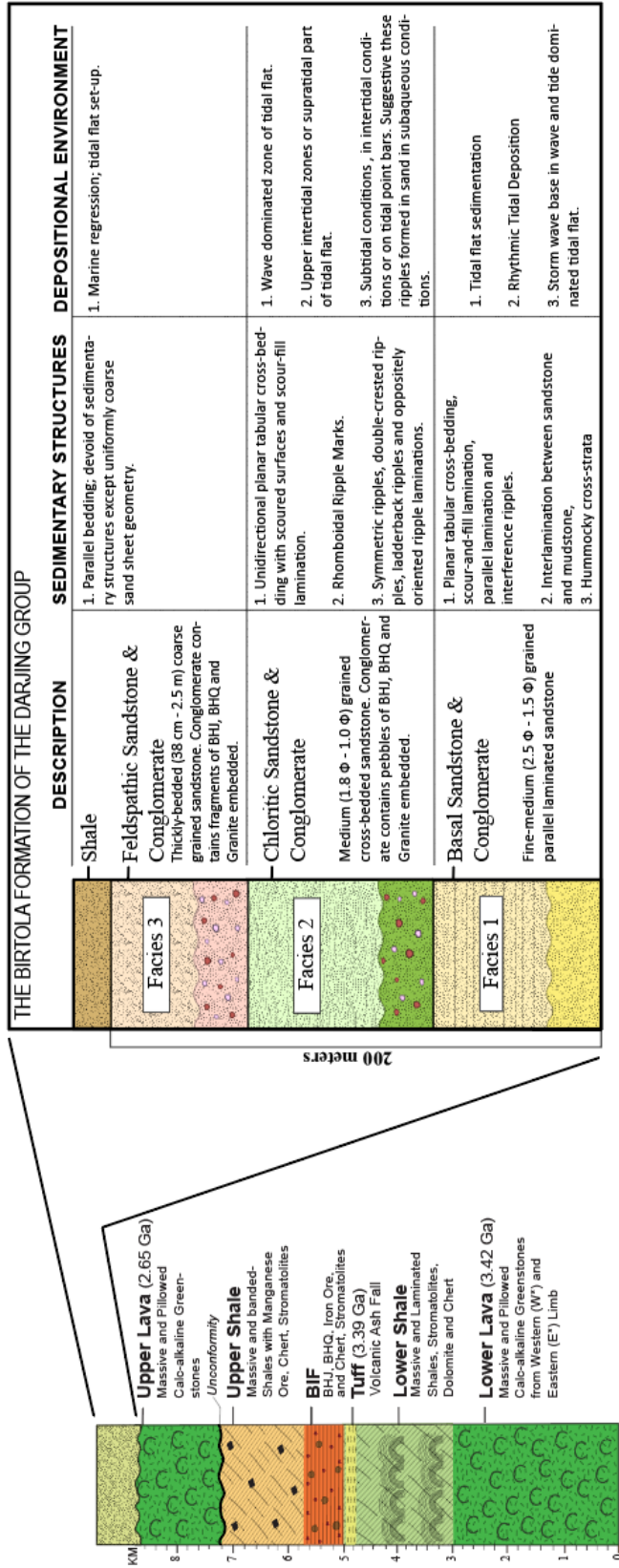


**Figure 16.** Stratigraphic column for the Birtola Formation of the Darjiling Group, Eastern India. The Birtola Formation has been observed to unconformably overlie the Western Iron Ore Group along parts of its Western Limb. Field image is from Google Earth.

#### 4.4.3 Zircon Hafnium Isotopes procedure

LA-MC-ICPMS hafnium isotope analyses for the zircons were carried out (after ion microprobe U-Pb and  $^{18}\text{O}/^{16}\text{O}$ -analysis) at the Australian National University, Canberra, using the 193 nm excimer laser-based HELEX ablation system equipped with a Neptune multiple collectors inductively coupled plasma mass spectrometer (described in Eggins et al., 2005, Wang et al., 2009; and Hiess et al., 2009). Data were reduced offline using the software package Iolite (Hellstrom et al., 2008; Paton et al., 2010, 2011). The results, listed in Table 7, were calibrated with the standard zircons 91500, FC-1, and Plesovice (Wiedenbeck et al., 1995; Woodhead et al., 2004; Woodhead and Hergt, 2005; Slama et al., 2008) and synthetic (Fisher et al. 2011). The laser spot sizes are about 40 microns, and ablation times angled up to 60 seconds. Note  $^{180}\text{Hf}$  was not measured due to the difficulty of multi-collector setup although it is the most abundant mass (35.08%).

Initial epsilon hafnium value,  $\epsilon_{\text{Hf}(t)}$ , was calculated using a decay constant ( $\lambda$ ) of  $1.865 \times 10^{-11} \text{ yr}^{-1}$  (Scherer et al., 2001). For calculating initial epsilon values, present-day CHUR was taken as  $^{176}\text{Lu}/^{177}\text{Hf} = 0.0332$ ,  $^{176}\text{Hf}/^{177}\text{Hf} = 0.282772$  (Blichert-Toft and Albarède 1997).

$$\text{Eq.11} \quad \epsilon_{\text{Hf}(t)} = \left[ \frac{(^{176}\text{Hf}/^{177}\text{Hf})_{\text{initial}}^t}{(^{176}\text{Hf}/^{177}\text{Hf})_{\text{CHUR}}^t} - 1 \right] \times 10^4$$

Depleted mantle model ages were calculated using equations of the form:

$$\text{Eq.12} \quad T_{\text{DM}} = \frac{1}{\lambda} \ln \left[ \frac{(^{176}\text{Hf}/^{177}\text{Hf})_{\text{sample}}^{\text{today}} - (^{176}\text{Hf}/^{177}\text{Hf})_{\text{depleted mantle}}^{\text{today}}}{(^{176}\text{Lu}/^{177}\text{Hf})_{\text{sample}}^{\text{today}} - (^{176}\text{Lu}/^{177}\text{Hf})_{\text{depleted mantle}}^{\text{today}}} + 1 \right]$$

where, the present-day  $\epsilon_{\text{Hf}(t)}$  value used is +16.9 ( $^{176}\text{Lu}/^{177}\text{Hf} = 0.0384$ ,  $^{176}\text{Hf}/^{177}\text{Hf} = 0.28325$ ): for MORB (or DM; Griffin et al. 2000). Another useful parameter is to compare the present day measured  $^{176}\text{Hf}/^{177}\text{Hf}$  ratio from the sample of interest to the present-day CHUR value, which

illustrates the extent to which the individual samples are fractionated relative to CHUR. The  $\epsilon_{\text{Hf}}(0)$  value is:

$$\text{Eq.13} \quad \epsilon_{\text{Hf}}(0) = \left[ \frac{(^{176}\text{Hf}/^{177}\text{Hf})_{\text{measured}}^{\text{today}}}{(^{176}\text{Hf}/^{177}\text{Hf})_{\text{CHUR}}^{\text{today}}} - 1 \right] * 10^4$$

The accepted  $^{176}\text{Hf}/^{177}\text{Hf}$  data for zircon standards used in this study are from Woodhead & Hergt (2005) and Sláma et al. (2008). \* Interference correction, expressed in  $\epsilon_{\text{Hf}}$  units, was estimated as  $((^{176}\text{Yb}/^{177}\text{Hf} + ^{176}\text{Hf}/^{177}\text{Hf})(0.000028))$  (Fisher et al., 2014).

#### 4.4.5 Oxygen Isotopes (whole rock)

##### 4.4.4 Whole rock oxygen isotope procedure

Whole-rock samples were crushed or sieved to a size of approximately 0.5 mm. All samples were treated with 10% HCl over a period of three days to remove any carbonate if present. Samples were then washed with distilled water. Separates of the mineral's feldspar, augite, and amphiboles were achieved through the use of a magnetic separator, followed by hand picking under a Motic binocular microscope. Oxygen isotope analysis on whole-rock and mineral separate samples were performed at the Southern Methodist University Stable Isotope Laboratory, following the  $\text{BeF}_5$  extraction method of Clayton and Mayeda (1963). The extracted oxygen gas was analyzed by dual-inlet Thermo Finnigan MAT 253 isotope mass spectrometer. Replicate analysis of quartz standard NBS-28 gave an average  $\delta^{18}\text{O}$  value of 9.6‰. Reproducibility of analysis of sample quartzs and whole rock  $\delta^{18}\text{O}$  value is  $\pm 0.15\text{‰}$ , and  $\pm 0.2\text{‰}$ , respectively. Oxygen isotope results are presented in Table 9 following the conventional delta ( $\delta$ ) notation, whereby  $\delta^{18}\text{O} = [(^{18}\text{O}/^{16}\text{O}_{\text{sample}} / ^{18}\text{O}/^{16}\text{O}_{\text{VSMOW}}) - 1] \times 1000$ , the deviation in the sample's ratio in parts per mil relative to the standard ratio of modern seawater, SMOW.

**Table 7** Detrital U-Pb zircon geochronology and oxygen isotope compositions

Zircon	Pb %	Isotope Ratios								Age (Ma)				Conc. (%)	$\delta^{18}\text{O}$ (‰)
		$^{238}\text{U}/^{206}\text{Pb}$	$\pm 1 \sigma$	$^{207}\text{Pb}/^{235}\text{U}$	$\pm 1 \sigma$	$^{206}\text{Pb}/^{238}\text{U}$	$\pm 1 \sigma$	$^{207}\text{Pb}/^{206}\text{Pb}$	$\pm 1 \sigma$	$^{206}\text{Pb}/^{238}\text{U}$	$\pm 1 \sigma$	$^{207}\text{Pb}/^{206}\text{Pb}$	$\pm 1 \sigma$		
PRM-01.1	0.1	2.1169	0.0237	10.578	0.117	0.4729	0.003	0.1632	0.001	2,521	23	2,481	15	100	6.89 ± 0.3
PRM-02.1	0.12	2.1366	0.0223	11.047	0.069	0.468	0.0049	0.1712	0.0008	2,486	21	2,569	7	100	4.95 ± 0.2
PRM-04.1	0.14	2.1941	0.0236	9.774	0.075	0.4558	0.0049	0.1555	0.0008	2,421	21	2,408	9	100	4.16 ± 0.1
PRM-09.1	0.05	1.7662	0.0195	15.595	0.153	0.5662	0.0062	0.1998	0.0015	2,892	25	2,824	11	102	5.10 ± 0.1
PRM-12.1	0.03	2.1051	0.0236	10.209	0.127	0.475	0.0053	0.1559	0.0015	2,506	23	2,411	16	103	7.27 ± 0.2
PRM-15.1	0.05	2.1344	0.0232	10.475	0.109	0.4688	0.003	0.1626	0.001	2,507	22	2,478	13	100	6.36 ± 0.2
PRM-17.1	0.19	1.9689	0.0289	11.76	0.132	0.5079	0.0074	0.1679	0.0014	2,648	31	2,537	13	100	5.79 ± 0.2
PRM-19.1	0.07	2.0475	0.0215	11.01	0.079	0.4884	0.0051	0.1635	0.0009	2,564	22	2,492	9	102	5.30 ± 0.1
PRM-22.1	0.17	1.9149	0.0197	13.201	0.075	0.5222	0.0054	0.1833	0.0008	2,709	22	2,683	7	100	-6.30 ± 0.1
PRM-24.1	0.89	2.1202	0.0231	10.605	0.135	0.4759	0.003	0.1703	0.001	2,535	22	2,488	18	100	5.98 ± 0.2
PRM-27.1	0.04	2.0852	0.022	10.698	0.069	0.4796	0.0051	0.1618	0.0007	2,525	22	2,474	6	102	5.40 ± 0.1
PRM-28.1	0.05	2.0698	0.0215	11.548	0.076	0.4834	0.023	0.1737	0.008	2,556	77	2,590	78	98	5.02 ± 0.3
PRM-30.1	0.03	1.8874	0.0208	13.691	0.136	0.5298	0.0058	0.1874	0.0014	2,741	24	2,720	12	100	5.48 ± 0.3
PRM-33.1	0.07	2.1082	0.0232	10.554	0.138	0.4743	0.0052	0.1614	0.0018	2,503	22	2,470	18	101	6.56 ± 0.1
PRM-35.1	0.01	2.1266	0.0231	10.527	0.089	0.4702	0.0051	0.1624	0.0009	2,485	22	2,480	9	100	5.20 ± 0.5
PRM-37.1	0.11	2.273	0.061	9.631	0.401	0.4404	0.017	0.1597	0.002	2,369	53	2,443	12	96	5.17 ± 0.3
PRM-40.1	0.16	2.1972	0.0229	9.957	0.065	0.4551	0.0047	0.1587	0.0008	2,418	20	2,442	8	99	4.62 ± 0.2
PRM-41.1	0.18	1.953	0.0229	12.19	0.125	0.512	0.006	0.1727	0.0012	2,665	25	2,584	11	103	5.34 ± 0.4
PRM-44.1	0.2	2.0955	0.0229	10.608	0.101	0.4772	0.0052	0.1612	0.0011	2,515	22	2,468	11	102	6.38 ± 0.2
PRM-45.1	0.03	2.0835	0.0217	10.556	0.075	0.48	0.005	0.1595	0.0009	2,527	21	2,450	9	103	7.04 ± 0.1
PRM-47.1	0.11	2.1751	0.0249	10.248	0.128	0.4603	0.004	0.1626	0.001	2,492	23	2,473	14	98	6.14 ± 0.4
PRM-48.1	0.97	2.2768	0.0241	10.317	0.084	0.4392	0.0047	0.1704	0.0011	2,297	20	2,561	10	91	5.36 ± 0.1
PRM-49.1	0.02	1.8984	0.0193	13.149	0.055	0.5268	0.0054	0.181	0.0006	2,749	22	2,663	5	102	5.06 ± 0.1
PRM-50.1	0.03	1.8169	0.0199	14.924	0.141	0.5504	0.006	0.1967	0.0014	2,837	25	2,799	11	101	5.92 ± 0.1
PRM-53.1	1.65	1.9595	0.0208	12.466	0.144	0.5103	0.0054	0.1772	0.0018	2,667	23	2,626	17	101	5.85 ± 0.1
PRM-54.1	0.24	1.4196	0.0183	29.509	0.397	0.7044	0.0091	0.3038	0.0025	3,397	34	3,490	12	98	4.51 ± 0.2
PRM-55.1	0.19	2.2977	0.0247	9.6	0.094	0.436	0.003	0.1615	0.001	2,345	21	2,455	11	94	5.83 ± 0.1
PRM-56.1	1.08	2.1824	0.0235	9.976	0.077	0.4582	0.0049	0.1579	0.001	2,431	21	2,433	10	100	-5.12 ± 0.2
PRM-57.1	1.02	2.3632	0.0268	9.3	0.095	0.4232	0.0048	0.1594	0.0014	2,275	21	2,449	14	92	4.40 ± 0.3
PRM-58.1	0.33	2.37	0.0244	8.54	0.048	0.4219	0.0043	0.1468	0.0007	2,269	19	2,309	7	98	5.24 ± 0.1
PRM-59.1	0.45	2.1262	0.1628	10.384	0.617	0.4724	0.028	0.1638	0.001	2,536	162	2,457	15	101	5.85 ± 0.3
PRM-60.1	0.02	2.1614	0.0225	10.281	0.074	0.4627	0.002	0.1613	0.0009	2,475	21	2,468	9	99	6.38 ± 0.2
PRM-63.1	0.19	2.1115	0.0226	10.7	0.105	0.4745	0.003	0.1654	0.001	2,528	22	2,496	13	100	6.81 ± 0.1
PRM-65.1	4.41	2.2135	0.0531	9.755	2.344	0.4726	0.016	0.1928	0.018	2,435	61	2,419	355	99	4.40 ± 0.3
PRM-67.1	0.25	2.1863	0.0254	10.323	0.156	0.4586	0.004	0.1657	0.002	2,500	24	2,494	20	97	4.66 ± 0.2
PRM-68.1	0.06	2.1607	0.0219	9.615	0.052	0.4628	0.0047	0.1507	0.0007	2,452	20	2,354	7	104	1.84 ± 0.3
PRM-69.1	0.12	2.1241	0.024	10.489	0.113	0.4713	0.004	0.1625	0.001	2,551	23	2,472	12	100	3.91 ± 0.2
PRM-70.1	0.03	2.0652	0.0214	11.089	0.07	0.4842	0.005	0.1661	0.0008	2,546	21	2,519	8	101	7.07 ± 0.2
PRM-73.1	0.05	2.2661	0.0244	9.634	0.1	0.4413	0.0048	0.1583	0.0013	2,356	21	2,438	13	96	5.20 ± 0.1
PRM-74.1	0.02	1.8974	0.0196	13.61	0.08	0.527	0.0054	0.1873	0.0008	2,729	22	2,718	7	100	4.70 ± 0.2
PRM-75.1	0.01	1.3543	0.0142	30.585	0.159	0.7384	0.0077	0.3004	0.001	3,565	28	3,472	5	102	5.28 ± 0.1
PRM-76.1	0.05	2.1643	0.0244	10.39	0.119	0.4621	0.0052	0.1631	0.0014	2,449	22	2,488	14	98	6.04 ± 0.1
PRM-78.1	0.19	2.0878	0.0249	10.632	0.166	0.4799	0.004	0.1626	0.002	2,558	25	2,466	12	102	4.59 ± 0.3
PRM-80.1	0.09	2.1444	0.0227	10.552	0.09	0.4663	0.0049	0.1641	0.0011	2,467	21	2,499	11	98	6.76 ± 0.1
PRM-81.1	0.01	1.8045	0.0195	14.938	0.103	0.5542	0.006	0.1955	0.0007	2,842	24	2,789	6	102	6.83 ± 0.1
PRM-82.1	0	2.1378	0.0226	10.316	0.084	0.4678	0.0049	0.1599	0.001	2,474	21	2,455	10	100	6.75 ± 0.1
PRM-83.1	0.37	2.0419	0.0288	11.428	0.303	0.4915	0.007	0.1722	0.003	2,615	30	2,550	36	100	5.69 ± 0.1
PRM-85.1	0	2.1709	0.0293	10.714	0.203	0.4606	0.0062	0.1687	0.0023	2,442	27	2,545	22	96	5.88 ± 0.1
PRM-86.1	0.03	1.9262	0.02	13.067	0.083	0.5191	0.0054	0.1826	0.0009	2,696	22	2,676	7	100	5.67 ± 0.1
PRM-87.1	0.19	2.2504	0.0252	9.912	0.132	0.4452	0.004	0.1633	0.002	2,407	22	2,474	17	95	6.40 ± 0.3
PRM-88.1	0.05	2.2579	0.0232	9.5	0.059	0.4429	0.0046	0.1556	0.0008	2,364	20	2,408	8	98	6.30 ± 0.1
PRM-89.1	0.77	2.0194	0.0237	13.185	0.205	0.4952	0.0058	0.1931	0.0023	2,593	25	2,769	19	93	1.51 ± 0.1
PRM-91.1	0.19	2.1113	0.0253	10.418	0.18	0.4746	0.005	0.1611	0.002	2,528	25	2,451	23	101	5.14 ± 0.1
PRM-92.1	0.09	1.877	0.0208	14.484	0.158	0.5328	0.0059	0.1972	0.0016	2,753	24	2,803	13	98	1.92 ± 0.1
PRM-94.1	0.22	2.2701	0.0252	10.449	0.135	0.4405	0.0049	0.172	0.0018	2,353	21	2,578	17	91	6.24 ± 0.1
PRM-95.1	0.27	1.9933	0.0207	12.511	0.083	0.5017	0.0052	0.1809	0.0009	2,621	22	2,661	8	98	-0.01 ± 0.4
PRM-96.1	0	2.2622	0.0258	9.778	0.131	0.4421	0.005	0.1604	0.0017	2,360	22	2,460	17	96	7.89 ± 0.1
PRM-97.1	0.37	1.7161	0.018	18.624	0.127	0.5827	0.0061	0.2318	0.0012	2,960	24	3,064	8	96	5.59 ± 0.1
PRM-98.1	0.04	2.0963	0.0224	10.578	0.087	0.4772	0.003	0.1611	0.001	2,544	22	2,464	10	102	4.74 ± 0.03
PRM-99.1	0.18	2.3319	0.0264	9.093	0.081	0.4288	0.0049	0.1538	0.001	2,300	21	2,388	10	96	6.18 ± 0.2

Selected SHRIMP U-Pb isotopic data with < 10% discordance from sample PRM of the Birtola Formation

All radiogenic errors are quoted at 1  $\sigma$  level.

Oxygen isotope values are reported in per mil (‰) deviations from Vienna standard mean ocean water (VSMOW); uncertainties in  $\delta^{18}\text{O}$  are reported at 2  $\sigma$ .

Conc. % is concordance percent defined as  $[(^{206}\text{Pb}/^{238}\text{U age}) / (^{207}\text{Pb}/^{206}\text{Pb age})] \times 100$

206-Pb % is common Pb

**Table 8** Lu-Hf isotope data measured from andstone sample PRM from the Birtola Formation

Grain I.D.	$^{176}\text{Lu}/^{177}\text{Hf}$	$\pm 2\text{SE}$	$^{176}\text{Hf}/^{177}\text{Hf}$ (t)	$\pm 2\text{SE}$	$\epsilon\text{Hf}$ (t)	$\epsilon\text{Hf}$ (0)	$T_{\text{DM}}$ (Ma)	t, Age (Ma)
PRM_1	0.001015	0.000046	0.281242	0.000040	-0.2	-54.1	2805	2481
PRM_2	0.001172	0.000093	0.281137	0.000042	-1.6	-57.8	2960	2599
PRM_4	0.0008484	5.3E-06	0.280478	0.000033	-28.7	-81.1	3819	2408
PRM_9	0.000494	0.000017	0.280958	0.000040	-1.6	-64.2	3148	2824
PRM_12	0.000603	0.000015	0.281267	0.000048	-0.2	-53.2	2742	2411
PRM_15	0.000746	0.000014	0.281282	0.000048	1.6	-52.7	2732	2478
PRM_17	0.000472	0.000032	0.281195	0.000037	0.3	-55.8	2829	2537
PRM_19	0.000397	0.000039	0.28112	0.000050	-3.3	-58.4	2924	2492
PRM_20	0.000581	4.4E-06	0.280836	0.000035	-7.0	-68.5	3318	2784
PRM_22	0.001154	0.000043	0.281087	0.000040	-1.4	-59.6	3027	2683
PRM_24	0.0003505	0.000005	0.281193	0.000043	-0.7	-55.8	2823	2488
PRM_27	0.001371	0.000018	0.281278	0.000038	0.3	-52.8	2782	2474
PRM_28	0.000574	0.000014	0.281125	0.000041	-1.2	-58.2	2931	2590
PRM_30	0.0005595	3.1E-06	0.280853	0.000040	-7.8	-67.9	3293	2720
PRM_33	0.0005065	6.1E-06	0.281294	0.000051	2.2	-52.3	2699	2470
PRM_34	0.0004907	8.8E-06	0.280941	0.000037	-14.1	-64.8	3170	2299
PRM_35	0.000377	0.000011	0.281027	0.000034	-6.8	-61.7	3047	2480
PRM_37	0.000796	0.00003	0.281123	0.000045	-4.9	-58.3	2950	2443
PRM_40	0.000736	0.00002	0.281197	0.000039	-2.2	-55.7	2846	2442
PRM_41	0.000916	0.000017	0.281118	0.000052	-2.1	-58.5	2966	2584
PRM_44	0.00079	0.000078	0.281267	0.000043	0.8	-53.2	2755	2468
PRM_45	0.0005986	5.9E-06	0.281269	0.000035	0.8	-53.2	2739	2450
PRM_47	0.0004344	4.1E-06	0.281191	0.000047	-1.2	-55.9	2832	2473
PRM_48	0.000982	0.000028	0.281137	0.000042	-2.1	-57.8	2945	2561
PRM_49	0.00166	0.00011	0.281053	0.000037	-4.0	-60.8	3114	2663
PRM_50	0.00057	0.000019	0.280665	0.000040	-12.8	-74.5	3544	2799
PRM_53	0.00039	0.000018	0.281116	0.000029	-0.3	-58.6	2929	2626
PRM_54	0.003428	0.000059	0.28079	0.000063	0.7	-70.1	3645	3490
PRM_55	0.000917	0.000014	0.281263	0.000051	0.1	-53.4	2770	2455
PRM_56	0.00254	0.00024	0.281093	0.000037	-9.1	-59.4	3132	2433
PRM_57	0.001185	0.000056	0.281101	0.000059	-6.2	-59.1	3010	2449
PRM_58	0.000894	0.000019	0.281157	0.000049	-6.9	-57.1	2912	2309
PRM_59	0.000777	0.000042	0.2811	0.000052	-5.4	-59.1	2980	2457
PRM_60	0.0002794	6.5E-06	0.281196	0.000032	-0.9	-55.7	2814	2468
PRM_63	0.000643	0.000047	0.281151	0.000045	-2.5	-57.3	2901	2496
PRM_65	0.000553	0.000018	0.281251	0.000043	-0.5	-53.8	2760	2419
PRM_67	0.000539	0.000018	0.281139	0.000042	-2.4	-57.7	2909	2510
PRM_68	0.00116	0.00011	0.280925	0.000046	-14.5	-65.3	3247	2354
PRM_69	0.00121	0.00012	0.280959	0.000057	-10.8	-64.1	3205	2472
PRM_70	0.000711	0.000041	0.281235	0.000044	0.9	-54.4	2793	2519
PRM_73	0.000556	0.00003	0.281132	0.000036	-4.3	-58.0	2920	2438
PRM_74	0.002562	0.000087	0.281321	0.000054	5.1	-51.3	2811	2719
PRM_75	0.000844	0.00003	0.280568	0.000043	-1.4	-77.9	3699	3472
PRM_76	0.000585	0.00001	0.281229	0.000040	0.2	-54.6	2792	2488
PRM_78	0.0005698	2.8E-06	0.28105	0.000044	-6.6	-60.9	3031	2466
PRM_80	0.0002786	8.8E-06	0.281238	0.000045	1.3	-54.2	2758	2499
PRM_81	0.000337	0.000019	0.280836	0.000035	-6.5	-68.5	3297	2789
PRM_82	0.000724	0.000047	0.281213	0.000046	-1.3	-55.1	2823	2455
PRM_83	0.000691	0.000014	0.281295	0.000045	3.8	-52.2	2710	2550
PRM_84	0.000505	0.000079	0.281241	0.000047	1.4	-54.1	2770	2515
PRM_86	0.0009	0.00011	0.280968	0.000038	-5.4	-63.8	3167	2676
PRM_87	0.000997	0.000033	0.281282	0.000053	1.1	-52.7	2750	2474
PRM_88	0.000761	0.000036	0.281241	0.000044	-1.5	-54.1	2788	2408
PRM_89	0.000702	0.00001	0.280941	0.000039	-3.9	-64.8	3188	2769
PRM_91	0.001129	0.000043	0.28121	0.000048	-2.2	-55.2	2857	2451
PRM_92	0.000896	0.000026	0.280953	0.000046	-3.0	-64.3	3187	2803
PRM_94	0.0006978	5.2E-06	0.281196	0.000042	0.9	-55.7	2844	2578
PRM_95	0.000895	0.000018	0.281109	0.000038	-0.7	-58.8	2977	2661
PRM_96	0.0007393	5.4E-06	0.281221	0.000046	-1.0	-54.8	2814	2460
PRM_97	0.001593	0.000055	0.280722	0.000058	-6.8	-72.5	3562	3064
PRM_98	0.000784	0.000042	0.281148	0.000049	-3.5	-57.4	2916	2464
PRM_99	0.001108	0.000019	0.281306	0.000034	-0.2	-51.8	2725	2388

Note: t, Age (Ma) refers to the actual U-Pb zircon crystallization age  
 See methodology for  $\epsilon\text{Hf}$  (t),  $\epsilon\text{Hf}$  (0), and  $T_{\text{DM}}$  (Ma) calculations.

**Table 9** Whole rock oxygen, water, and hydrogen data for the Birtola sandstone

Sample	$\delta^{18}\text{O}$ (‰)	Replicate analysis	$\delta\text{D}$ (‰)	H <sub>2</sub> O (wt.%)	Replicate analysis
27/96	8	1	-85	0.17	1
30/96	6.8	1	-77	0.32	1
24/96	7.6	2	-75	0.3	2
25/96	7.4	2	-67	0.28	1
PRM	5.8	3	-98	1.13	2
R/96	7	1	-63	0.44	2
23/96	7.2	1	-73	0.23	2
P3/96	7.1	2	-60	0.43	1
P6/96	6.3	2	-64	0.38	1
31/96	8.5	1	-80	0.4	2

*Note* : reported oxygen values are the average of replicate analysis.  
Replicate analysis deviations for oxygen were less than a per mil.  
Oxygen data is on whole-rock sandstones; hydrogen data represent  
fluid-inclusion values from quartz separates of whole-rocks.  
Samples originally from Saha et al., 2004.

Above samples are from Saha et al., 2004.

## 4.5 Results

### 4.5.1 Petrography

Petrographic analysis for the sandstones of the Birtola Formation in this study was conducted to determine their range of modal compositions. Their principal framework is defined by well-sorted, sub-rounded to well-rounded quartz grains featuring long, concavo-convex and sutured contacts indicative of compaction during metamorphic quartzite formation. The major compositional phases

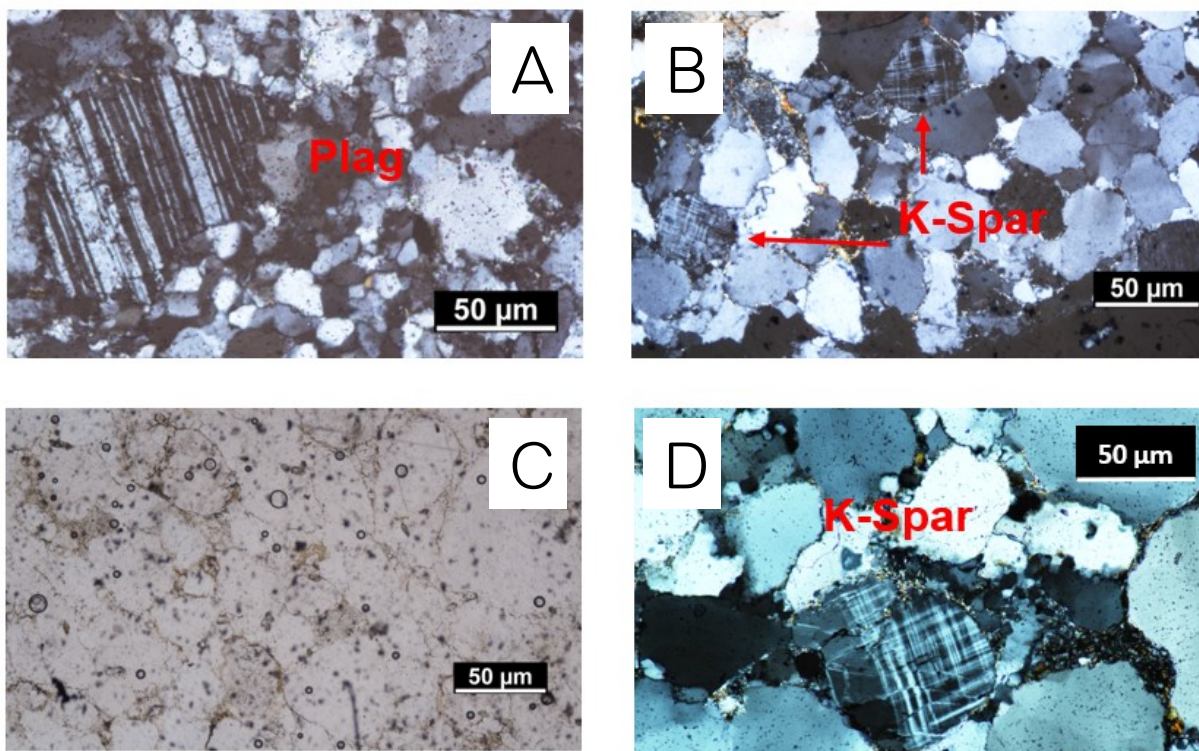


**Figure 17.** Photomicrographs of the Birtola sandstones showing. (A) fresh, medium-sized, rounded plagioclase feldspar grain showing polysynthetic albite twinning, obtuse extinction, surrounded by sutured monocrystalline and polycrystalline quartz. Note the atypical texture observed for the large feldspar grain surrounded by finer quartz; (B) Two well-rounded microcline grains with characteristic grid twinning; (C) Abundant aqueous fluid and vapor inclusions in quartz seen through plain-polarized light. (D). Medium sand-sized microcline grain with characteristic cross-hatched twinning.

consist of quartz with accessory phases of feldspar, chlorite, biotite, sericite, chert, zircon, sphene, magnetite and rock fragments. Quartz, dominantly of the milky to glassy-clear variety, constitutes the bulk composition of each sample, with an average abundance of >90% corresponding to Quartz Arkose. Clasts of monocrystalline and polycrystalline quartz are the two notable forms, with the former representing nearly two thirds in proportion. Most of the observed monocrystalline quartz typically occurs as medium sand-sized, non-undulatory grains which lack mineral inclusions. Whereas polycrystalline grains occur as fine sand-size disaggregation's featuring evidence of plastic deformation from undulatory extinction and sutured grain

boundaries.

These siliciclastic rocks are generally matrix poor with evidence of post-burial or pre-deposition pressure solution deformation (Fig. 17A). However, some grains are rimmed by a diagenetic pseudomatrix of chlorite and sericite around the grain boundaries and along cleavage planes of feldspar. Alkali and Plagioclase feldspar constitute, on average, less than 5% of the total framework minerals. Nearly all feldspar grains are fresh, medium to large sand-sized, sub-rounded to rounded, and freshly preserved and unaltered, with only a few examples of partial sericitization (Fig. 17B). Potassium feldspar dominates the feldspar suite, often occurring a well-rounded sand-sized grains typically displaying characteristic grid “tartan” twinning (Fig. 17C), while plagioclase is subordinate, less rounded and showing characteristic polysynthetic albite twinning (Fig. 17D). These quartz arenites (feldspar bearing  $< 10\%$ ;  $\geq 90\%$  quartz) preserve multi-cycle conditions as indicated by the well-rounded and well-sorted textural nature of the quartz (and separated zircons), which is characteristic of compositional and textural maturity. However, the presence of occasional feldspar grains populated within these quartz arenites suggests a component of immaturity and first-cycle conditions, or a combination of recycled and first-cycle sedimentary materials that were eroded from the Southeastern hinterlands of the basin during Birtola Formation deposition.

#### *4.5.2 Zircon U-Pb ages*

Sensitive High-Resolution Ion Microprobe (SHRIMP) U-Th-Pb zircon dating was undertaken on sample PRM. A total of 100 zircon grains were measured with 40% of zircons being above a 10% discordant threshold and were thus screened out for further analysis. The isotopic results for sixty concordant zircon core analyses are presented in Table 7 and illustrated

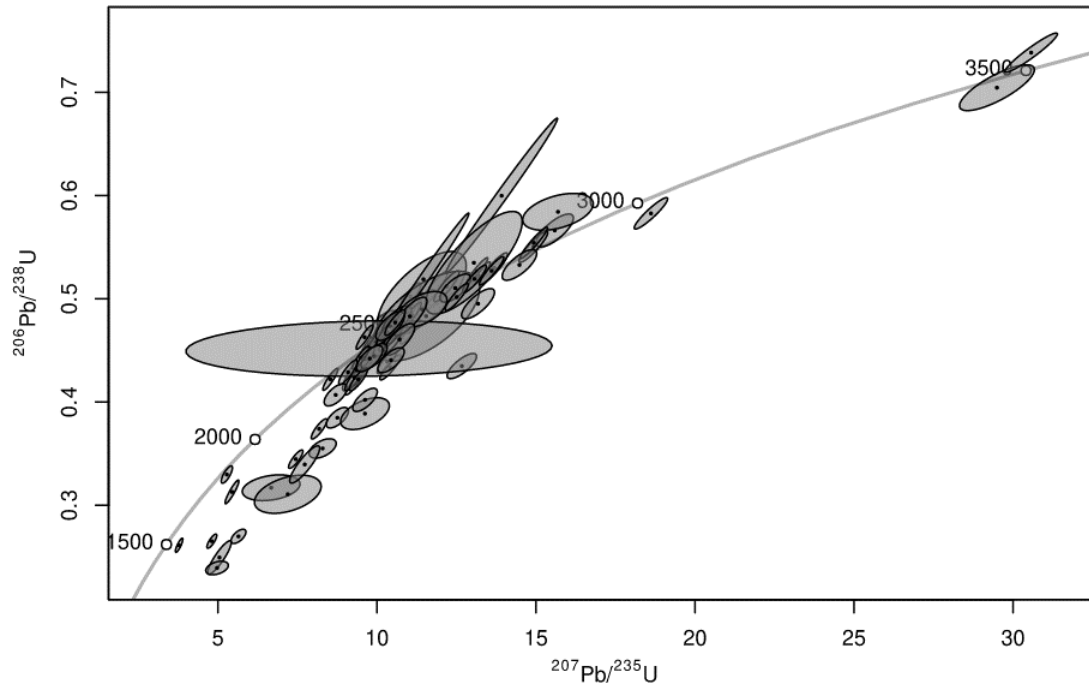


**Figure 18.** U-Pb Zircon geochronology of the Birtola Sandstone for sample PRM. Plotted using Isoplot.

in Fig. 18. These zircon grains are well-rounded in shape and display a broad range in  $^{207}\text{Pb}/^{206}\text{Pb}$  ages, with a maximum and minimum age of 3,490 Ma age and 2,309 Ma, respectively. Within this 1,181 Ma age range lies a bimodal age population exhibiting a weighted mean of 2,567 Ma age and median 2,484 Ma age with rare discrete Paleoproterozoic grains. Thus, most zircon U-Th-Pb estimates ages are Paleoproterozoic-Neoproterozoic in age, coinciding with the APTB. Based on the lowest concordant zircon age, the Birtola metasedimentary succession can be constrained to have a maximum depositional age of 2,309 Ma. We interpret all concordant ages to reflect the protolith ages of magmatic crystallization. Additionally, the 2.8, 2.5, and 2.4 Ga age populations are consistent with the anorogenic 2.8 Ga alkali-feldspar granite, Pallahara gneiss, and syenogranite bodies which are thought to have served as the basement for Dajing Group deposition within the basin (e.g., Mazumder et al., 2012). The more ancestral (3,064, 3,472, and

3490 Ma) grains are interpreted as a minor contribution from the inheritance of the volumetrically dominant tonalites which make up the Singhbhum craton.

#### 4.5.3 Zircon oxygen isotopes

60 zircon grains were selected for in-situ  $\delta^{18}\text{O}$  measurements and exhibit a remarkably variable range ( $-6.30\text{‰} \leq \delta^{18}\text{O}_{\text{zircon}} \leq +7.8 \text{‰}$ ) (Table 7; Fig. 19). These zircons record highly variable  $\delta^{18}\text{O}$  values with more than a 15‰ difference from the maximum and minimum  $\delta^{18}\text{O}$  measurements. Grains PRM-22.1 ( $-6.3\text{‰} \pm 0.1\text{‰}$ ;  $\sim 2.7$  Ga) and PRM-56.1 ( $-5.12\text{‰} \pm 0.2 \text{‰}$ ; 2.4 Ga) are some of the lowest  $^{18}\text{O}$  zircons measured for their age, both of which exhibit 100% concordance. Twenty-five zircons feature  $\delta^{18}\text{O}$  values ( $4.95\text{‰} \leq \delta^{18}\text{O} \leq +5.9 \text{‰}$ ) which fall within error of the primary  $5.3 \pm 0.6 \text{‰}$  mantle value. On the other hand, sixteen zircons fall below the mantle value ( $-6.3 \text{‰} \leq \delta^{18}\text{O}_{\text{zircon}} \leq 4.7 \text{‰}$ ), while nineteen zircons have  $\delta^{18}\text{O}$  supracrustal values ( $6.1 \text{‰} \leq \delta^{18}\text{O}_{\text{zircon}} \leq 7.8 \text{‰}$ ) greater than the mantle value (Fig. 19). Thus, 41% of  $\delta^{18}\text{O}_{\text{zircon}}$  values are “mantle-like,” 31% are “supracrustal-like,” and 26% are “hydrothermal-like” zircons.

#### 4.5.4 Zircon Hf isotopes

Hf isotopic ratios were measured for 63 zircons. The 2,309 to 2,599 Ma age populations exhibit a notable spreads in subchondritic to highly-unradiogenic Hf values ( $^{176}\text{Hf}/^{177}\text{Hf} = 0.280458\text{--}0.281275$ ; initial  $\epsilon_{\text{Hf}} = -28.7$  to 3.8; see Fig. 34; Table 8). This observation is consistent with a mixing between a diluted juvenile population ( $0.2 \leq \epsilon_{\text{Hf}(t)} \leq 3.8$ ,  $n = 14$ ) and a predominant ancestral crustal population ( $-28.7 \leq \epsilon_{\text{Hf}(t)} \leq -0.2$ ,  $n = 47$ ). The 2,626 to 2,824 Ma age populations also consists of a subchondritic and highly unradiogenic spread in Hf values

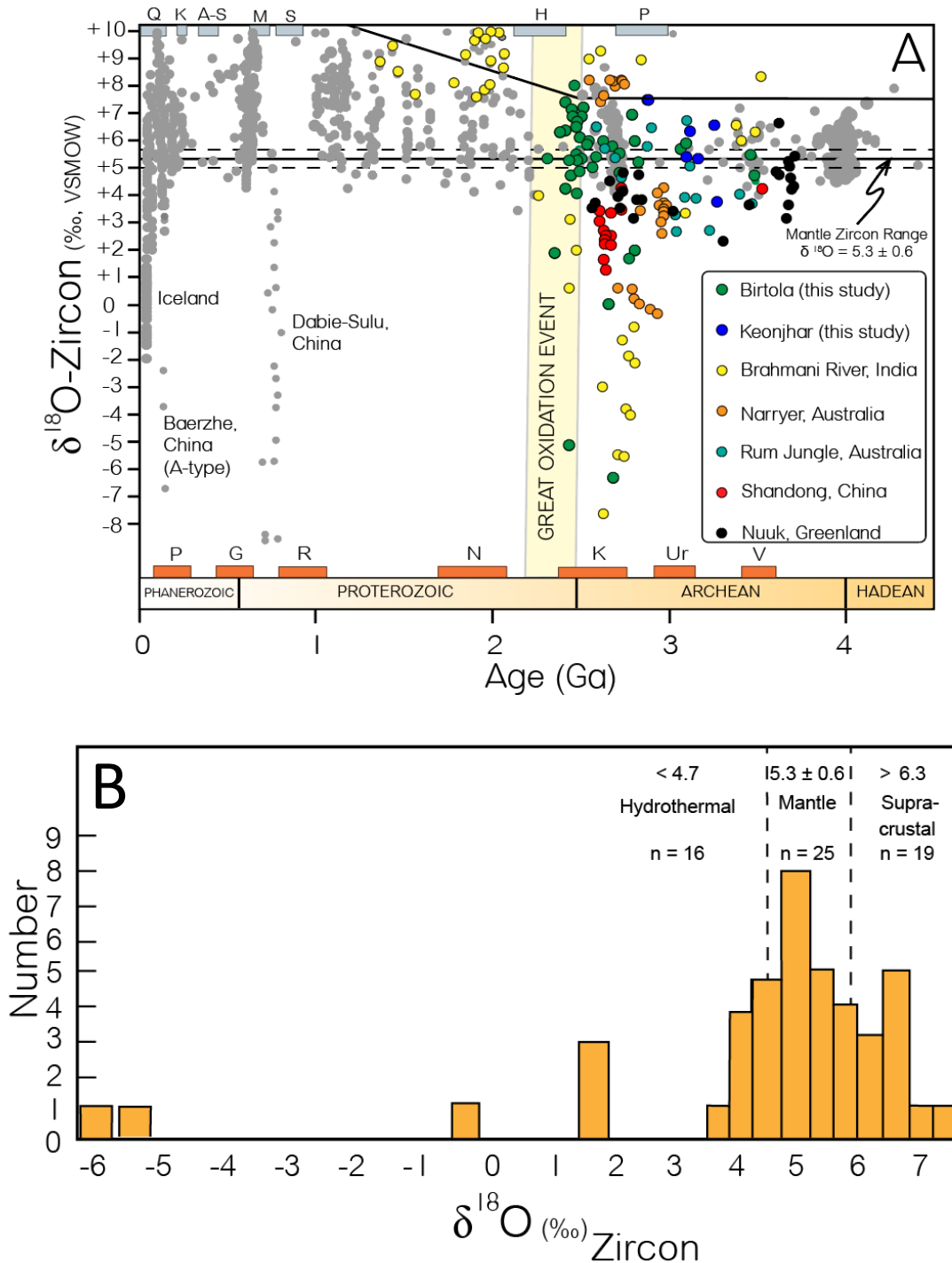


**Figure 19.** Zircon oxygen isotope data. (A) Zircon isotope of interest vs time.  $\delta^{18}\text{O}$ -zircon evolution diagram whereby the most notable features are the onset of  $^{18}\text{O}$ -enrichment and  $^{18}\text{O}$ -depletion in zircons peaking at 2.7 Ga. Note that the Brahmani River mimics the Birtola formation. This is consistent with the observation that this river drains the Singhbhum Craton and cuts directly through the Darjiling Group (i.e., the Birtola Formation). The occurrence of low- $^{18}\text{O}$  zircons samples from the Singhbhum craton is synchronous with the low- $^{18}\text{O}$  zircons

sampled from the Yilgard craton (Australia) and the Chinese Craton (China). Modern low- $^{18}\text{O}$  zircons (Phanerozoic) are sampled from extensional tectonic settings. Errors are smaller than the symbol size. All zircons have a concordance  $\geq 93\%$ . Supplementary data includes Zheng et al., 2004; Yang et al., 2013; Valley, 2005 and references therein. (B) Range of  $\delta^{18}\text{O}$  values for the Birtola zircons. Twenty-five zircons have mantle-like  $\delta^{18}\text{O}$  values of  $5.3 \pm 0.6$ . Sixteen zircons have hydrothermal  $\delta^{18}\text{O}$  values  $< 4.7\%$ . Nineteen zircons have supracrustal  $\delta^{18}\text{O}$  values  $> 6.3\%$ .

( $^{176}\text{Hf}/^{177}\text{Hf} = 0.280665\text{--}0.281321$ ,  $\epsilon_{\text{Hf}} = -12.8$  to  $5.1$ ; Fig. 20). The Birtola sandstone zircons depleted mantle model ages ( $T_{\text{DM}}$ ) correspond to a mean of  $2,986$  Ma, a median of  $2,918$ , a maximum of  $3,818$  Ma, and a minimum of  $2,699$  Ma. Nearly all of the Birtola zircons  $^{207}\text{Pb}/^{206}\text{Pb}$  crystallization ages exhibit depleted mantle model ages which are  $300\text{--}500$  Ma older (Fig. 21B). The low- $^{18}\text{O}$  zircons all consistently correlate with having much older depleted mantle model ages (avg.  $\text{Hf } T_{\text{DM}} = 3,107$  Ma), which are in stark contrast to the high- $^{18}\text{O}$  supracrustal zircons ( $6.1\% \leq \delta^{18}\text{O}_{\text{zircon}} \leq 7.8\%$ ,  $n = 17$ ) with much younger depleted mantle model ages ( $\text{Hf } T_{\text{DM}} = 2,815$  Ma) (Fig. 20A).

#### 4.5.5 Whole rock oxygen and hydrogen isotopes

The oxygen isotope compositions were determined for ten whole-rock sandstones and are presented in the  $\delta^{18}\text{O}$  notation as seen in Table 9. These sandstones are composed on average of  $\geq 90\%$  detrital quartz. The oxygen isotope values for all sandstones are uniformly low ( $+5.8\% \leq \delta^{18}\text{O} \leq +8.5\%$ ; avg.  $7.1\%$ ). These samples appear to be the lowest  $^{18}\text{O}$  sandstones ever reported, with sample PRMs  $5.8\%$  value to be remarkably indistinguishable from upper mantle  $5.5 \pm 0.5\%$  values (see Matthey et al., 1994; Chazot et al., 1997). Hydrogen isotope compositions were determined for ten whole-rock sandstones (quartz separates only) and are presented in the  $\delta\text{D}$  notation as seen in Table 9. The hydrogen isotope

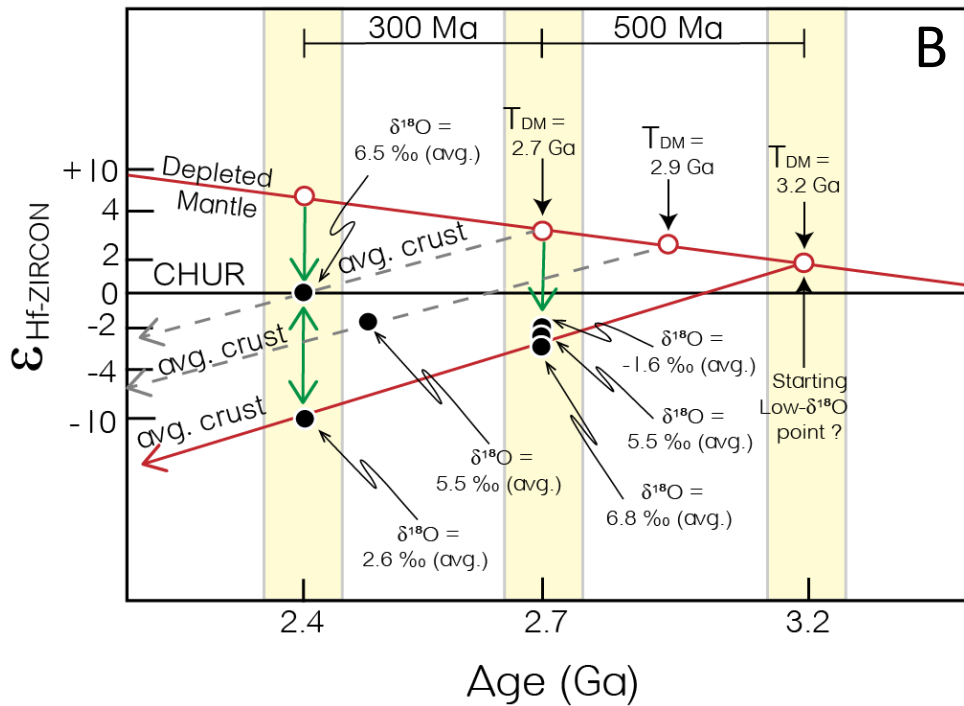
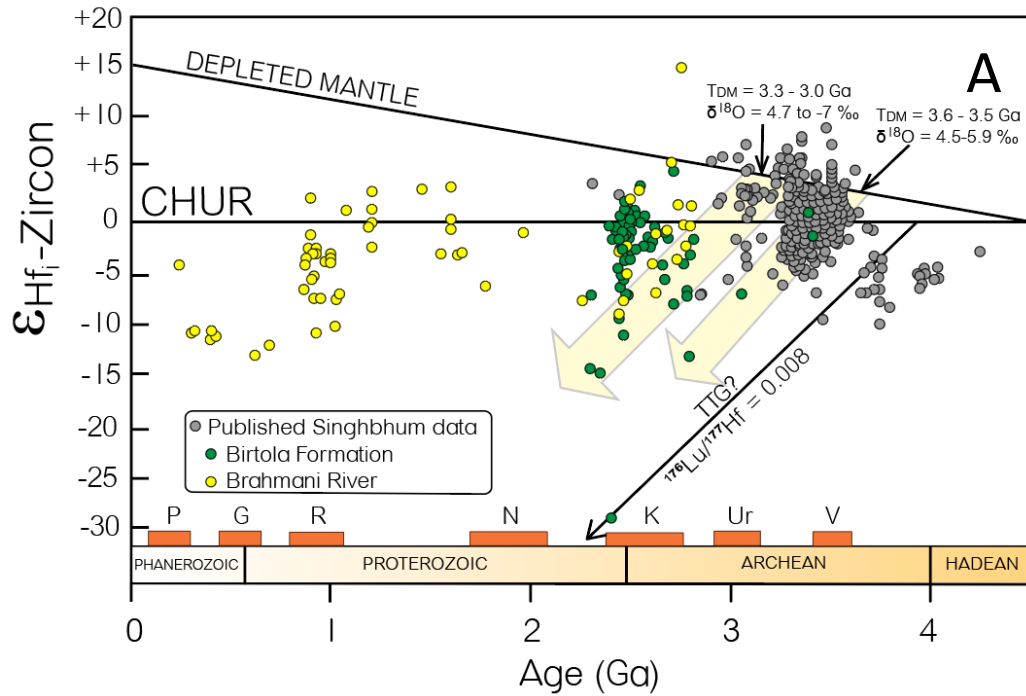


**Figure 20.** Birtola zircon Hf systematics. (A) Zircon from the Birtola Formation, Singhbhum Craton (green data points) exhibit evidence for crustal reworking during 3.3 Ga to 2.4 Ga. A key episode of juvenile input is seen at 2.4 Ga. (B) When parsing the data into two distinct populations, we can observe the low- $^{18}\text{O}$  zircons to have two separate episodes of crystallization at both 2.7 Ga and 2.4 Ga with corresponding  $\sim 3.2$  Ga depleted mantle model ages ( $T_{\text{DM}}$ ). The

data may suggest that, assuming the original low- $^{18}\text{O}$  basaltic source was emplaced at 3.2 Ga, at 2.7 Ga the Birtola zircons grew during a period characterized by crustal reworking and not due to juvenile input. This suggestion is strengthened by the observation that the low- $^{18}\text{O}$  zircons (-1.6 ‰ avg.), mantle-like  $^{18}\text{O}$  zircons (5.5 ‰ avg.), and supracrustal  $^{18}\text{O}$  zircons (6.8 ‰ avg.) all have tightly clustered unradiogenic ( $-\epsilon_{\text{Hf}}$ ) signatures. This reworking event at 2.7 Ga coincides with the amalgamation of the supercontinent Kenorland. The 500 Ma interval from the original mantle-derived low- $^{18}\text{O}$  basaltic source (which may have occurred in a rift setting), to the reworking of the low- $^{18}\text{O}$  basaltic source (which may have occurred during the assembly of Kenorland), represents a characteristic plate tectonic timescale and implies a crustal residence age. The next crustal reworking event occurs at 2.4 Ga, as indicated by the occurrence of a low- $^{18}\text{O}$  zircon population falling along the 3.2 Ga depleted mantle evolution curve and exhibiting increasingly unradiogenic ( $-\epsilon_{\text{Hf}}$ ) signatures. However, at this same crystallization period, the high- $^{18}\text{O}$  population (6.5 ‰ avg.) exhibits chondritic ( $\epsilon_{\text{Hf}}$ ) signatures indicating mixing between ancient crustal and juvenile reservoirs. A plausible tectonic setting which could impart these characteristics is a continental rift setting. The timing of this suggested rifting event coincides with the proposed period of the break-up of the supercontinent Kenorland. This 300 Ma period suggests an average crustal residence age.

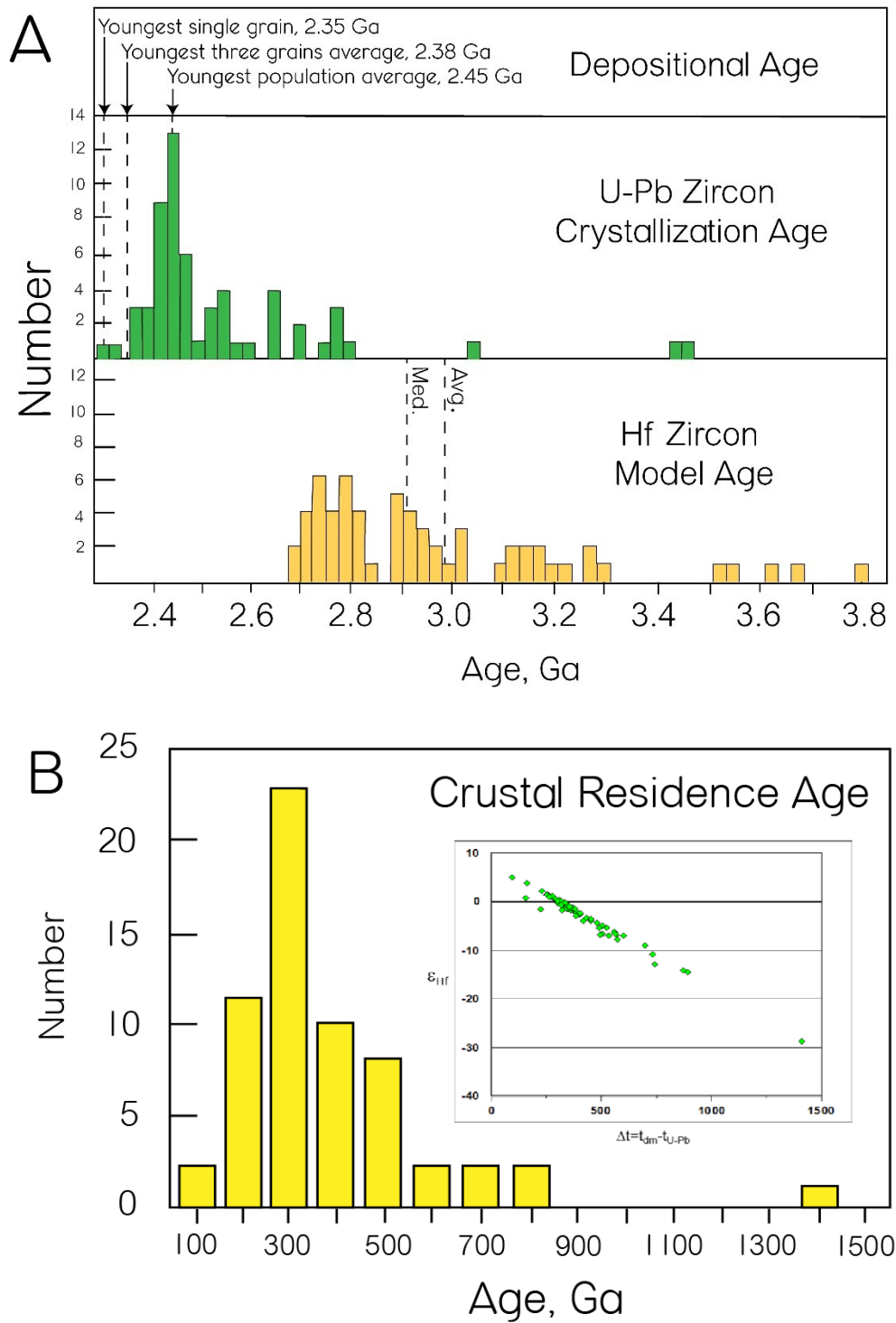


**Figure 21.** Comparison diagrams between the crystallization age vs depleted mantle model age. (A) Nearly all zircons exhibit depleted mantle model ages which are 200-500 million years older than their crystallization age. (B) The emplacement age represents the  $^{207}\text{Pb}/^{206}\text{Pb}$  age measured from the zircons. Juvenile zircons which lack an older continental component have model ages similar to their crystallization ages, while reworked crust exhibits depleted mantle model ages much older than their emplacement age. Average crustal residence age for the Birtola Formation

zircons whose  $^{207}\text{Pb}/^{206}\text{Pb}$  crystallization ages span the Archean-Paleoproterozoic. The average crustal residence age is defined as the difference between the U-Pb zircon crystallization age and the Hf  $T_{\text{DM}}$  model age. This reflects characteristic times for the average residence between 200-500 million years, which is within the time window of a Wilson Cycle (i.e., a plate tectonic cycle). The Hf  $T_{\text{DM}}$  model age may place a constraint on the timing of rifting and the U-Pb zircon igneous ages may place a constraint on the timing of subduction and continental collision (i.e., the time of crustal reprocessing).

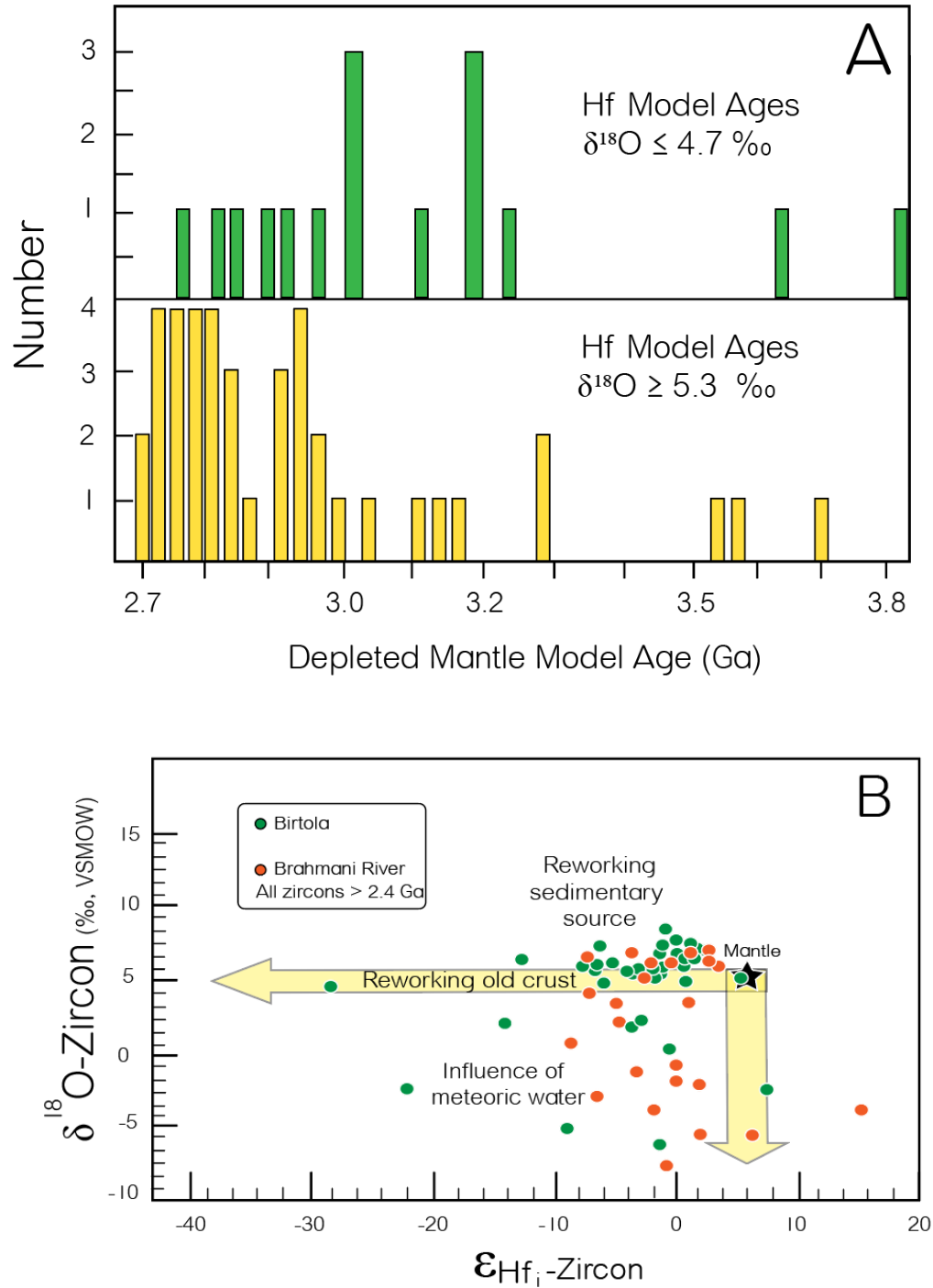


**Figure 22.** Discrimination diagrams between oxygen and Hf isotopes from the Birtola zircons. (A) 60% of all low- $^{18}\text{O}$  zircons reported in this study have depleted mantle model ages older than 3.0 Ga, including sample PRM22 ( $\delta^{18}\text{O} = -6.3 \text{ ‰}$ ; 3,027 Ga) and PRM56 ( $\delta^{18}\text{O} = -5.1 \text{ ‰}$ ; 3,132 Ga) (B) The Birtola zircons suggests having been influenced by a hydrothermal meteoric water component while other suggests having incorporated an older sedimentary component. The Brahmani River zircons which sample the Birtola formation have  $\delta^{18}\text{O}$  values that mimic each other suggesting a common reservoir.

compositions are interpreted to represent fluid inclusions within quartz. Their isotopic values are moderately uniform ( $-98‰ \leq \delta D \leq -60‰$ ; avg.  $-74‰$ ).

## **4.6 Discussion**

### *4.6.1 Detrital feldspar as a proxy for climate*

Granitic rocks, which are predominantly composed of quartz and feldspar, are volumetrically the most abundant rock of the upper continental crust and is therefore tends to be the main source for detrital siliciclastic sediments in many depositional basins. Since quartz consists of silica tetrahedrons in a 3-D framework structure, has a Mohs-scale hardness of seven, as well as conchoidal fracture with no planes of crystalline weakness (cleavage), it is preordained to be highly stable in the low temperatures and pressures of near-surface sedimentary environments; in addition to having a low solubility and rate of dissolution (e.g., Blatt, 1967). In contrast, feldspar is most stable in the higher temperature and pressure igneous and metamorphic environments in which they originated. Unlike quartz, feldspar has two planes of cleavage and is thermodynamically unstable in soils and shallow sedimentary deposits, and quickly alters to clay minerals at Earth's surface, preordaining feldspar, an ephemeral mineral in any sedimentary environment, to not persist long in the sedimentary cycle (e.g., Kastner and Siever, 1979).

The occurrence of feldspars in sandstones are known to either be authigenic or detrital in origin. Authigenic feldspar, however, exists as only a small fraction of the feldspars in the rock. They typically grow in place by replacement through either precipitation from interstitial or formation waters during diagenesis and typically show no evidence of weathering or alteration. Moreover, authigenic feldspar is commonly untwined and occurs as very pure endmembers

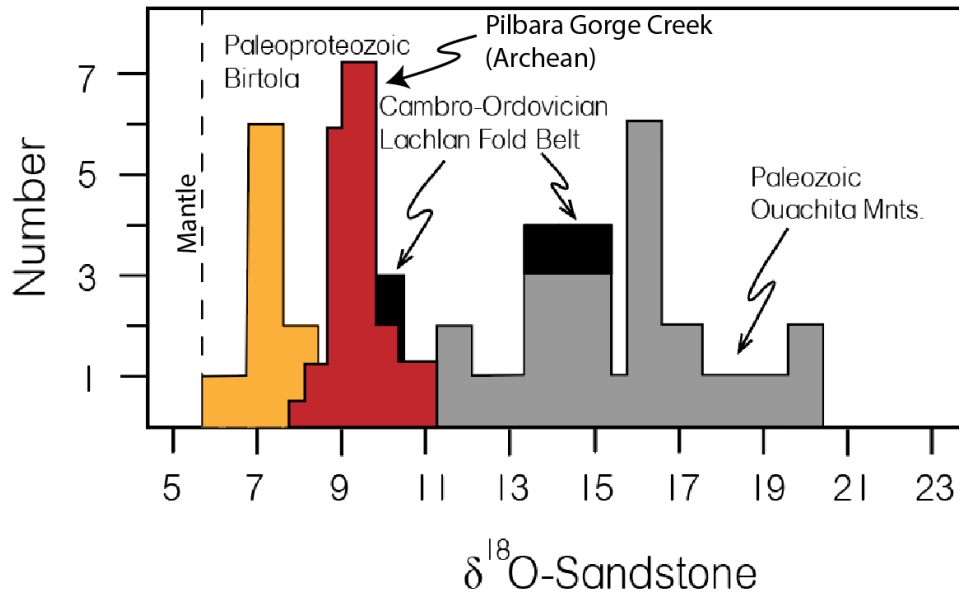


**Figure 23.** Histogram comparison between the  $\delta^{18}\text{O}$  values of first-cycle sandstones from the Paleoproterozoic Birtola Formation sandstones (India), Archean Gorge Creek sandstones (Australia) and the multi-cycle Lachlan Fold Belt (Cambro-Ordovician) and Ouachita Mountains (Paleozoic). The increase in  $^{18}\text{O}$  over geologic time as recorded by quartz in sandstones is consistent with sedimentary material becoming increasingly incorporated into the formation of granite. The bulk sandstones  $\delta^{18}\text{O}$  values for the Birtola formation are consistent with ground-up silicic rocks from volcanic terrains. The quartz grains from the Birtola sandstones are consistent with fractional crystallization from mantle derived magmas, particularly anhydrous silicate magmas of small volume. Sandstone data from Gregory (2007).

(Kastner and Siever, 1979).

On the other hand, the survival of detrital feldspar in a sandstone is dependent on the absence of a sufficient water source or rapid burial which inhibits chemical alteration of these grains.

Therefore, the preservation of fresh detrital feldspar can serve as a climatic indicator since the only environments that allow for a sufficient lack of moisture are a warm arid or cold arid climate. However, abundant feldspar can also become preserved where tectonic processes rapidly uplift local source regions, followed by rapid erosion, deposition, and burial without much transportation under a warm and humid climatic regime (e.g., Basu et al., 1976). Feldspar grains

which are texturally fresh and well-rounded require enough transportation time for abrasion and attrition processes in order to modify the grains-size and morphology prior to deposition and burial (Chakrabarti et al., 1998). If roundness is suggested to have occurred due to aeolian activity within a warm arid climate followed by rapid burial, then primary sedimentary structures for an aeolian depositional setting should be preserved. However, if deposition took place in a cold arid climate, the retention of the freshness and large well-rounded character of feldspar can be attained by aeolian activity in a periglacial environment, as long as primary depositional sedimentary structures preserve evidence for such a depositional setting. Therefore, it seems reasonable to suggest that the large well-rounded feldspars found within the Birtola sandstones became embedded within small, well- to subrounded quartz grains during cool-climate glacial conditions, possibly ice-rafted within an Alpine glacial setting. This is a similar conclusion to the original proposal by Chakrabarti et al., 2005 who suggested that the conglomerate-sandstone association could be argued as a diamictite deposit.

#### *4.6.2 Zircon oxygen isotopes and source characteristics*

Zircons,  $ZrSiO_4$ , are refractory minerals which are chemically akin to granitic (i.e., felsic) rocks. Magmas in equilibrium with the mantle produce igneous zircons with a remarkably narrow range of  $\delta^{18}O$ -values of  $5.3 \pm 0.6\%$  (Valley et al., 1998). Any observed positive or negative departures from this reference point are related to processes that arise from Earth having a stable ocean of liquid water and a dynamic tectonic regime.

For example, fractional crystallization of a silicate magma in a closed system can produce only a limited range of  $\delta^{18}O$ -values for igneous rocks between 5.3‰ to ~6.3‰ (Valley, 2003). However, values greater than ~6.3‰ typically involve melting of an  $^{18}O$ -enriched metasedimentary source that formed from low-temperature interaction with surface waters—a

geochemical signature typical of peraluminous granites (i.e., S-type) (e.g., O'Neil and Chappell 1977; Turi and Taylor, 1971; Valley, 2003). On the other hand, anorogenic granites (i.e., A-type) commonly produce zircons with  $\delta^{18}\text{O}$ -values less than their primary 5.3‰ mantle value. Such low- $^{18}\text{O}$  zircons are the result of a magmatic inheritance of a low- $^{18}\text{O}$  signature through the melting of a hydrothermally altered low- $^{18}\text{O}$  source rock influenced by the high-temperature interaction with  $^{18}\text{O}$ -depleted meteoric water (e.g., Criss and Taylor, 1983; Taylor and Sheppard, 1986; Taylor, 1987; Wei et al., 2008; Tang et al., 2014). From a planetary evolution perspective, Valley et al., 2005 evaluated a compilation of  $\delta^{18}\text{O}$ -values in zircons through geologic time and observed only a narrow range of dominantly normal mantle values during the Hadean and Archean. Valley et al., 2005 and Roberts and Spencer (2014) both submitted that the Archean-Proterozoic boundary signals a clear transition from homogeneous mantle-like values to strongly elevated  $\delta^{18}\text{O}$  heterogeneous signatures (Fig. 33). Their proposal suggests this geologic time boundary may represent the growth and maturation of the continents as well as the transition to collisional tectonics.

The occurrence of low- $^{18}\text{O}$  silicic magmas, and by extension zircons ( $< 5.3 \pm 0.6\text{‰}$ ), are rare worldwide. Most low- $^{18}\text{O}$  magmas are often anhydrous and occur as small volumes that formed under low-pressure (e.g., Balsley and Gregory, 1998; Troch et al., 2020). The two prominent localities known to be currently producing low- $^{18}\text{O}$  values are Iceland (e.g., Bindeman et al., 2012; Pope et al., 2013; Kleine et al., 2018) and the Yellowstone Plateau (Wyoming) within the Snake River Plain system (e.g., Bindeman and Valley, 2001). Even though Neoproterozoic examples are becoming increasingly reported (e.g., Rumble et al., 2002; Zheng et al., 2004; Yang et al., 2016; He et al., 2016), there remains very few known Paleoproterozoic and Archean examples (e.g., Bindeman et al., 2010; Hiess et al., 2011; Hollis et al., 2014;

Hammerli et al., 2018). The common parameter between all low- $^{18}\text{O}$  localities is the presence of an active extensional tectonic regime. Such settings allow for the development of large-scale fractures and faults within the brittle crust permitting the deep penetration, circulation, and interaction of high-temperature ( $> 300^\circ\text{C}$ ) low- $^{18}\text{O}$  fluid with volcanic roof rocks above a shallow-level intrusion of a hot and dry magma reservoir (e.g., Taylor, 1987; Gregory and Taylor, 1981). The most plausible source for this fluid is meteoric water which is the only reservoir with negative  $\delta^{18}\text{O}$  values ranging from 0‰ to  $\leq -33$ ‰ (e.g., Terzer et al., 2013). If the Archean-Proterozoic time-boundary, characterized by a marked increase in zircon  $^{18}\text{O}$  values, is the result of global scale collisional tectonics as Roberts and Spencer (2014) has proposed at the APTB, then there should be preserved a complementary negative- $^{18}\text{O}$  reservoir—a signature most plausibly acquired at extensional (i.e., rifting) zones. Figure 19A shows the Birtola zircon data plotted alongside supplemental zircon- $^{18}\text{O}$  data from India, Australia, China, and Greenland. Collectively, the dataset shows low- $^{18}\text{O}$  zircon values come into the geologic record as early as  $\sim 3.5$  Ga with a notable negative excursion beginning at  $\sim 2.7$  to 2.5 Ga.

#### *4.6.3 Oxygen and hydrogen isotopes as a potential proxy for climate*

Igneous and metamorphic silicate rocks exhibit positive  $\delta^{18}\text{O}$  values, generally ranging from +6 to +15. Such rocks are therefore said to be enriched in  $^{18}\text{O}$  relative to the standard—seawater (SMOW, 0‰). The only source capable of imparting negative  $\delta^{18}\text{O}$  values on igneous and metamorphic rocks is meteoric water (i.e., fresh water), which ranges from -10 to -33 ‰ (e.g., Terzer et al., 2013). When water evaporates from seawater (0‰) near the equator, the evaporation process occurs under non-equilibrium conditions and fractionates the light isotope ( $^{16}\text{O}$ ) into water vapor, creating negative values for  $\text{H}_2\text{O}$  in the atmosphere. The cloud is enriched

in  $^{16}\text{O}$  relative to seawater (SMOW), imparting the whole with a negative  $\delta$  value. As the cloud moves to higher latitudes, it releases some of its water content in the form of rain under near-equilibrium conditions. The rainwater discharged is enriched in the heavy isotope,  $^{18}\text{O}$  and D, thereby making the residual cloud enriched in the light isotope,  $^{16}\text{O}$  and H. The effect is that each subsequent package of precipitation becomes increasingly enriched in the light isotope (negative  $\delta^{18}\text{O}$ ). Topography also plays a role, whereby mountains force air up, causing it to cool and water vapor to condense. Precipitation clouds move across a continental landmass following the Rayleigh distillation law. However, as clouds move towards the poles, the temperature declines causing the temperature dependent fractionation factors to increase—making distillation operate more effectively, resulting in very negative  $\delta$  values at the poles.

The most negative  $\delta^{18}\text{O}$  zircons from the Birtola formation ( $\sim -7$ ) requires fluid below -21 to -23 ‰ to achieve the same lowering in  $\delta^{18}\text{O}$  comparable to the low  $^{18}\text{O}$  silicic magmas in Iceland. The isotopically heavier Iceland zircons (down to -2) which is consistent with inferred source rocks for low  $^{18}\text{O}$  silicic magmas in Iceland partially melted from altered basalts that hydrothermally interacted with Icelandic meteoric waters (e.g., -13 to -15‰; Pope et al. 2013; Berg et al., 2016). Using the empirical calibration for MAT and the  $\delta^{18}\text{O}$  of meteoric water (Ferguson et al 1999), inferred surface temperatures would be sufficient to stabilize glaciers (using the maritime calibration). The hydrogen isotopes as measured from the quartz fluid inclusions ( $-98 \text{‰} \leq \delta\text{D} \leq -60\text{‰}$ ) suggest meteoric waters derived from mid- latitudinal regions not sampling the same the environment as the low  $^{18}\text{O}$  zircons.

#### *4.6.4 Hf isotopes as a proxy for crustal source and evolution*

Granitic zircons are commonly used to study the chemical evolution of the continental crust. Due to hafnium's presence in zircon, hafnium isotopes ( $^{176}\text{Lu}$ - $^{176}\text{Hf}$  system) have become

an increasingly used proxy for the study of crustal growth and changing tectonics. The initial  $\epsilon_{\text{Hf}}$  signature for individual zircons can be used to monitor whether the zircons were growing during periods of addition of fresh material from the mantle (juvenile crust), or simply melting and recycling existing continental crust (reworking) (see, Hawkesworth et al., 2010 and Gardiner et al., 2016 for a review). The growth of isotopically juvenile ( $+\epsilon_{\text{Hfzircon}}$ ) zircons commonly prevail during rifting and subduction-related processes. The growth of isotopically evolved ( $-\epsilon_{\text{Hfzircon}}$ ) zircons are characteristic of crustal reworking (i.e., recycling, metamorphism, remelting during crustal shortening events) which produce positive slopes, with a range of ages and increasingly negative  $\epsilon_{\text{Hf}}$  values through time. This is because ancient crust naturally evolves with time towards lower (more negative)  $\epsilon_{\text{Hf}}$  values because of the ingrowth of  $^{146}\text{Hf}$  due to the decay of  $^{176}\text{Lu}$  (e.g., Schaefer, 2016). The observation that nearly all Birtola zircons have  $T_{\text{DM}}$  ages 200-500 Ma older than their U-Pb emplacement ages (Fig. 21A), combined with an appreciable ancestral evolutionary component as implied by the negative  $\epsilon_{\text{Hf}}$  values and  $T_{\text{DM}}$  ages (Figure 35B), highlights the importance of extensively making new continental crust from reworking preexisting continental crust during the Archean-Proterozoic Time Boundary.

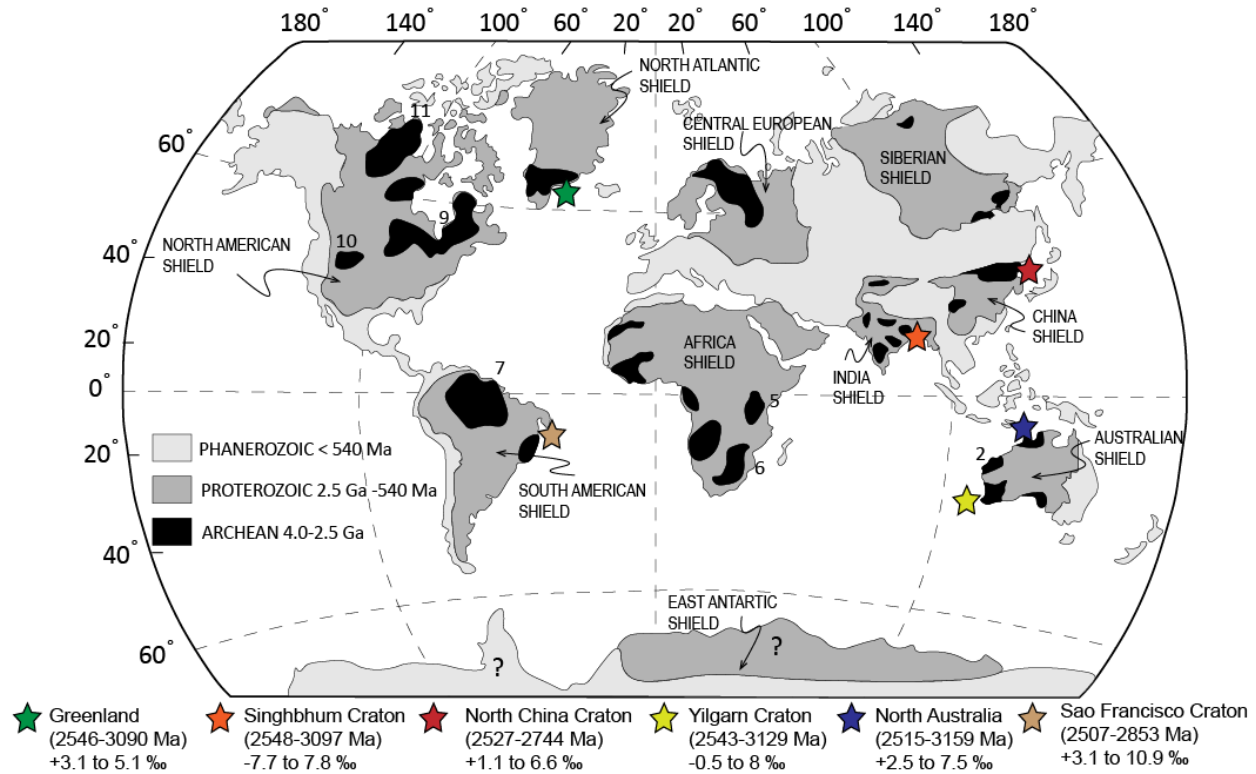


**Figure 24.** Map of continents which includes platforms overlain by sediments (after Condie, 2021). Localities of Mesoarchean to Neoproterozoic low- $^{18}\text{O}$  zircons are starred.

#### 4.6.5 Evidence for characteristic time constants and plate tectonics

The difference between the U-Pb zircon crystallization age and the Hf  $T_{DM}$  model age provides an estimate of the average crustal residence age, which corresponds to characteristic times between 200-500 million years (Fig. 21B). These results are within the time window of a Wilson Cycle (i.e., a plate tectonic cycle), and indicate a significant period of crustal growth and reworking during the late Archean and Paleoproterozoic. This may have occurred during the initial formation of the initial formation of the Singhbhum Mobile Belt that accreted against the Singhbhum craton. The Hf  $T_{DM}$  model age may place a constraint on the timing of rifting and the U-Pb zircon igneous ages may place a constraint on the timing of magmatism and associated

subduction and continental collision (i.e., the time of crustal reprocessing).

Further evidence in support of a Wilson Cycle may come from the correlation between low-<sup>18</sup>O zircons from Greenland, Singhbhum, North China, and Yilgarn, North Australia, and the Sao Francisco craton that indicate they may have been assembled into a single landmass  $\geq 3.1$  Ga (Fig. 19, 24), which subsequently underwent extensional rifting influenced by low-<sup>18</sup>O fluid. This is supported by the low-<sup>18</sup>O Birtola zircons which all have Hf depleted mantle model ages of  $\sim 3.1$  Ga. Similarly, all these cratons have a peak in detrital zircon U-Pb crystallization ages between 2.5-2.7 Ga, suggestive of the timing of subduction and/or collision during continental amalgamation, which is supported by the Birtola sandstones having initial  $\epsilon_{\text{HF}}$  signatures indicative of mixing between an ancient and juvenile source. The survival for the Birtola sandstones in Eastern India is favorable if their detritus was sourced from within an inland collisional setting as this tectonic setting increases its preservation potential (e.g., Hawkesworth et al., 2008). Furthermore, the Birtola formation (and the Darjiling Group as a whole) is part of a much larger geologic feature known as the Singhbhum Mobile Belt, which is accreted to the Singhbhum craton with both separated by a regional shear zone.

The significance of these results suggests that plate tectonics and its contemporary time constants present on Earth  $\sim 3.1$  to 2.5 billion-years ago was very similar to how it is currently. Additionally, the presented data may preserve evidence for the dispersal of the hypothesized supercontinent Ur and the formation of the supercontinent Kenorland. Furthermore, the dataset suggests that following the formation of the Singhbhum Craton, new Paleoproterozoic continental crust formed from extensively reworking cratonic crust, implying that the paucity of Archean crust reflects the efficiency at which it was recycled, not a lack of original production (e.g., Armstrong, 1991).

## 4.7 Conclusion

The Birtola zircons which have moderately evolved  $\epsilon_{\text{Hf}}$  values (5.1 to -28; avg -5.8) and are also low in  $^{18}\text{O}$  (4.9 to -6.3‰) have a  $\sim 3.2$  Ga average Hf depleted mantle model age which may correlate to a  $\sim 3.2$  Ga Kenorland supercontinent break-up event. Such a disassembly event may be reflected by the correlation between low- $^{18}\text{O}$  zircons from Greenland, Singhbhum, North China, and Yilgarn, North Australia, and the Sao Fransisco craton, indicating they may have been assembled into a single landmass which underwent rifting influenced by low- $^{18}\text{O}$  fluid. The most plausible source of fluid capable of imparting zircons as low as -7 is meteoric water at moderate latitude, which requires a depleted meteoric source  $< -13$  similar to that observed on Iceland. The average crustal residence ages for the Birtola zircons range between 200-500 million years, indicating a significant period of crustal growth and reworking occurred during the Late Archean to Paleoproterozoic. This may be related to the formation of the Kenorland supercontinent. In addition to the average crustal residence (and zircon  $T_{\text{DM}}$ ) ages, reworking of ancient crust is suggestive to play a significant role in the formation of new Paleoproterozoic crust as implied by the unradiogenic initial  $\epsilon_{\text{Hf}}$  values exhibited by nearly all 2.7 Ga crystallization zircon populations. This observation, in addition to the appearance of a high- $^{18}\text{O}$  zircon population at  $\sim 2.4$  Ga, may suggest continental rifting processes either during the disassembly of the supercontinent (Kenorland).

This study constrains the maximum age of the deposition for the Birtola formation to be  $\sim 2.35$  Ga as indicated by the youngest zircon age. At this maximum depositional age, large well-rounded feldspars became embedded within small well-rounded quartz grains, plausibly due to a cool climate in local glacial conditions. A cool to moderate latitude is supported by the range of

$\delta D$  ( $-98\text{‰} \leq \delta D_{\text{quartz}} \leq -60\text{‰}$ ; avg.  $-74 \text{‰}$ ,  $n = 10$ ) as measured from fluid inclusions within the detrital quartz from these sandstones.

## CHAPTER 6

### CONCLUSIONS

#### CHAPTER 2

This study obtained a 3.42 Ga Sm-Nd isochron age for the Lower Lava, which is conformable with the 3.39 Ga zircon U-Pb age obtained for the stratigraphically overlying tuff. The Lower Lava's initial  $^{143}\text{Nd}$  suggests derivation from a source that represents one of the best-preserved examples of early Earth's Hadean LREE- depleted mantle reservoir, whose  $^{143}\text{Nd}$  evolution mirrors that of the  $^{176}\text{Hf}$ -enriched crust as preserved in Singhbhum's zircon record. The new Nd isochrons reported between the Lower Lava and the unconformable Upper Lava bracket the depositional age of the W-IOG basin between 3.42-2.65 Ga. Lastly, the 3.39 Ga zircon tuff age immediately below the conformably overlying huge BIF deposit indicates large variations of free atmospheric oxygen during the Paleoproterozoic.

#### CHAPTER 3

This study examined the entire lithological suite of the W-IOG including its relationship with the concomitant emplacement of the adjacent OMTG and invoked a genetic relationship between the unroofing of the Lower Lava flood basalts and the origin of the BIF. The proposed ages for the Lower Lava ( $3.42 \pm 0.14$  Ga, Lower Shale ( $3.42 \pm 0.10$  Ga), Tuff ( $3.39 \pm 0.02$  Ga, and Upper Shale  $3.36 \pm 0.09$  Ga) all coincide with major crustal formation events according to Singhbhum's zircon record, implying pulses of orogenesis played a prominent role in the BIFs development. We estimated sedimentation within the basin to last for 60 Ma which ceased at 3.36 Ga. While the  $\delta^{56}\text{Fe}$  data alone cannot distinguish between the involvement of photosynthetic cyanobacteria or

anoxygenic photoferrotrophic oxidizing bacteria, it is argued that the biomass of the oxidant was limited.

#### CHAPTER 4

The Birtola Formation zircons have moderately evolved  $\epsilon_{\text{Hf}}$  values (5.1 to -28; avg -5.8) and are also low in  $^{18}\text{O}$  (4.9 to -6.3‰) have a  $\sim 3.1$  Ga average Hf depleted mantle model age which may correlate to a  $\sim 3.1$  Ga supercontinent break-up event. Such a disassembly event may be reflected by the correlation between low- $^{18}\text{O}$  zircons from Greenland, Singhbhum, North China, and Yilgarn, North Australia, and the Sao Francisco craton, indicating they may have been assembled into a single landmass which underwent rifting influenced by low- $^{18}\text{O}$  fluid. The most plausible source of fluid capable of imparting zircons as low as -7 is meteoric water at moderate latitude. The average crustal residence ages for the Birtola zircons range between 200-500 million years, indicating a significant period of crustal growth and reworking occurred during the Late Archean to Paleoproterozoic. This may be related to the formation of the Singhbhum Mobile Belt, a much larger geologic feature accreted to the Singhbhum Craton. In addition to the average crustal residence (and zircon  $T_{\text{DM}}$ ) ages, reworking of ancient crust may have been a significant role in the formation of new Paleoproterozoic crust as implied by the unradiogenic initial  $\epsilon_{\text{Hf}}$  values preserved in nearly all zircon populations. This observation, in addition to the appearance of a high- $^{18}\text{O}$  zircon population at  $\sim 2.5$  Ga, suggests active subduction-accretion processes either during the formation of the Singhbhum Mobile Belt or the assembly of a supercontinent (Kenorland). The correlation between reworked low- $^{18}\text{O}$  zircons can be seen within Greenland, Singhbhum, North China, Yilgarn, North Australia, and Sao Francisco may be related to supercontinent assembly around  $\sim 2.5$  Ga.

This study constrains the maximum age of the deposition for the Birtola formation to be ~2.3 Ga. At this maximum depositional age, large well-rounded feldspar detrital sedimentary grains comingled with small well-rounded quartz grains, plausibly due to a cool climate in local glacial conditions. A high-to-moderate latitude characterize by cool climates is supported by the range of  $\delta D$  ( $-98\text{‰} \leq \delta D_{\text{quartz}} \leq -60\text{‰}$ ; avg.  $-74 \text{‰}$ ,  $n = 10$ ) as measured from fluid inclusions within the detrital quartz grains from these sandstones.

## APPENDICES

**Table AI:** Data is compiled from the following sources:

Reference #	AGE (Ga)	$\epsilon\text{Nd}$	Lithology	Location	Country/Cont.	Reference	Journal
1	4.44	0.98	Ferroan Anorthosite	Moon (Apollo) sample 60025	Moon	Carlson & Lugmair (1988)	Earth & Plant. Si.
2	4.02	1.89	Gabbro (amphibolite facies)	Nuvvuagittuq Greenstone belt, Superior craton	Canada	O'Neil et al. 2008	Science
3	4.01	-2.01	Komatiite/peridotite suites	Northern Labrador, North-Atlantic Craton	Canada	Collerson et al. 1991	Nature
4	3.81	2.98	Peridotites/pyroxenites	Northern Labrador, North-Atlantic Craton	Canada	Collerson et al. 1991	Nature
5	3.77	2.03	Metavolcanics, metasediment	Isua Greenstone belt	W. Greenland	Hamilton et al. 1978	Nature
6	3.71	1.6	Komatiite, basalt	Talga-Talga subgroup (Warrawoona GB), Pilbara	W. Australia	Gruau et al. 1987	Earth & Plant. Si.
7	3.7	-2.6	Gneiss	Acasta, Slave Craton	Canada	Bowering et al. 1989	Nature
8	3.7	-4.8	Gneiss	Acasta, Slave Craton	Canada	Bowering et al. 1989	Nature
9	3.62	1.7	Gneiss	Amitsoq, Isua area	W. Greenland	Jones et al. 1985	Lunar & Plant. Sci.
10	3.56	1.95	Komatiite, bas, and, dac	North Star Basalt, Warrawoona Group, Pilbara	W. Australia	Hamilton et al. 1981	Geo. Soc.
11	3.54	1.16	Komatiites, bas, acidics	Onverwatch Greenstone belt, Barberton Craton	S. Africa	Hamilton et al. 1979	Nature
12	3.5	3.3	Amphibolite	Qianan County, Hebi province, Sino-Korean Crat.	China	Xuan et al. 1986	Geochemica
13	3.49	-3.4	Komatiites, grnsts, carbonat	Dresser formation, Warrawoona Group, Pilbara	W. Australia	Tessalina et al. 2010	Nature
14	3.47	2.89	Amphibolite	Hebi province, Sino-Korean Craton	China	Jahn et al. 1987	Precambrian Res.
15	3.43	5.74	Greenstones	Iron Ore Group Greenstone belt, Singhbhum Crat.	India	This Study	This Study
16	3.41	-0.86	Gneiss	AGC of Swaziland, Kaapvaal Craton	S. Africa	Carlson et al. 1983	Nature
17	3.37	2.21	Tonalite gneisses	Singhbhum Craton, OMTG	India	Sharma et al. 1994	Con. Min. Pet.
18	3.3	0.9	Amphibolite	Singhbhum Craton	India	Sharma et al. 1994	Con. Min. Pet.
19	2.95	0.13	Greenstones	Warriador Greenstone Belt, Yilgarn Craton	W. Australia	Fletcher & Rosman 1984	Precambrian Res.
20	3.06	0.27	Greenstones	Diemals Greenstone belt, Yilgarn Craton	W. Australia	Fletcher & Rosman 1984	Precambrian Res.
21	2.93	-2.6	Basalt, andesite, rhyolite	Pongola supergroup, Kaapvaal Craton	S. Africa	Hegner et al. 1984	Earth & Plant. Si.
22	2.92	2.22	Gneisses, Granulites	Lewisian Gneisses, Inner Hebrides	Scotland	Hamilton et al. 1979	Nature
23	2.9	-0.2	Metavolcanics	Santauri & Kalasapura volcanics, Bababudan, D	India	Kumar et al. 1996	Precambrian Res.
24	2.74	3.48	Greenstones	Iron Ore Group Greenstone belt, Singhbhum Crat.	India	This Study	This Study
25	2.82	2.2	Gneisses	K-S-Q	Greenland	Jones et al. 1985	Lunar & Plant. Sci.
26	2.82	2.7	Basalt	Sukumaland Greenstone belt, Tanzania Craton	Tanzania	Manya & Maboko 2003	Precambrian Res.
27	2.8	-2.8	Gabbro	Stillwater Complex, Montana	N. America	DePaolo & Wasserburg 1979	Geochemica
28	3.26	2.23	Greenstones	Kambalda Sequences, Yilgarn Craton	W. Australia	Claoue-Long et al., 1984	Nature
29	2.78	2.5	Greenstones	Kanowna Greenstone belt, Yilgarn Craton	W. Australia	Fletcher & Rosman 1984	Precambrian Res.
30	2.76	1.2	Komatiite, basalt	Munro township, Abitibi Greenstone belt, Superior	Canada	Zindler et al. 1978	U.S. Dept. Int.
31	2.75	2.4	Komatiite	Alexo area, Abitibi Greenstone belt, Superior Crat.	Canada	Dupre et al. 1984	Geochemica
32	2.73	1.81	Gneisses, Graywackes	Rainy Lake Area, Superior Craton	Canada	Shirey & Hanson 1986	Geochemica
33	2.7	1.88	Alkali basalts	Timiskaming Formation, Abitibi Greenstone belt,	Canada	Basu et al. 1984	Earth & Plant. Si.
34	2.7	2.5	Basalt, Rhyolite	Noranda, Abitibi Greenstone belt, Superior Crator	Canada	Vervoort et al. 1994	EPSL
35	2.64	-0.43	Komatiite, greenstones	Bulawayan Greenstone belt, Rhodesian Craton	S. Africa	Hamilton et al. 1977	Earth & Plant. Sci.
36	2.66	4.39	Komatiite, amphibolite, basalt	Hebi province, Sino-Korean Craton	China	Jahn & Ernst 1990	Precambrian Res.
37	2.2	1.3 to -5.2	Granitoids	North America, USA	N. America	Nelson & DePaolo 1985	Geo. Soc. America.
38	1.84	(-7) to (-1)	Basalts, Gabbros, diorites	Sudbury Complex	Canada	Faggart & Basu (1985)	Science
39	1.8	3.7	Granitoids	Colorado Front Range	N. America	Donald DePaolo 1981	Nature
40	1.8	2.8 to 8.2	metabasalt	Harts Range, Complex	Australia	Sivell & McCulloch (1991)	Nature
41	1.7	3.3 to 6.5	Greenstones	Rocky Mountains Range, Wyoming Craton	N. America	Nelson & DePaolo 1984	Nature
42	1.3	(-14) to (-)	Anorthosite	Nain Anorthosite complex	Canada	Emslie et al. 1994	Chicago Press
43	1	2.5	Anorthosite	Snowy Mountain dome	N. America	Basu & Pettingill (1983)	Geology
44	3.3 to 0.2	(-3.7) to -	Shale	Australian Shale	Australia	Allegre and Rousseau (1984)	Earth & Plant. Sci.
45	0.13	8 to 7.5	Basalt, Gabbro	Samail Ophiolite, Oman	Oman	McCulloch et al. 1981	Geophysical Res.
46	Modern	-17	Sediments	River water suspended material (N.A., W.G., Aus, Jap, Philp		Goldstein and Jacobsen (1988)	Earth & Planet. Sci.
47	Modern	12 to 7	Basalt	Mid-ocean ridge basalt (MORB)	Global	DePaolo & Wasserburg (197)	Geophysical. Res. Let.
48	0.2	(-7.5) to 8	Granitoids	California Batholiths	N. America	DePaolo (1981)	Nature
49	0.3 to 0.8	(-10) to 8	Volcanics & Sediments	Lachlan Fold belt	Australia	Keay et al. 1997	Geology
50	0.5	7.7	Pyroxene Gabbro	Bay of Island Ophiolite	Newfoundland	Jacob and Wasserburg (1979)	Geophysical Res.
51	3.71	3	Metasediment	Isua Greenstone belt	W. Greenland	Jacobsen and Dymek (1988)	J. Geophysical. Res. Let.
52	2.66	3.7	Basalt	The's flow, Abitibi greenstone belt	Canada	Debaille et al., 2013	EPSL
53	3.81	4.2	Peridotite	West Greenland	W. Greenland	Locht et al., 2020	Geochemica

**Table A11. References corresponding to Figure 7A.**

Ref#	Citation
1	R. W. Carlson, G. W. Lugmair, The age of ferruginous anorthositic 60025: oldest crust on a young Moon? <i>Earth Planet. Sci. Lett.</i> <b>90</b> , 119-130 (1988).
2	J. O'Neill, R. W. Carlson, D. Francis, R. K. Stevenson, Neodymium-142 Evidence for Hadean mafic, enst. <i>Science</i> <b>321</b> , 1828-1831 (2008).
3	K. D. Collerson, L. M. Campbell, B. L. Weaver, Z. A. Palocz, Evidence for extreme mantle fractionation in early Archean ultra-mafic rocks from Northern Labrador. <i>Nature</i> <b>349</b> , 209-214 (1991).
4	K. D. Collerson, L. M. Campbell, B. L. Weaver, Z. A. Palocz, Evidence for extreme mantle fractionation in early Archean ultra-mafic rocks from Northern Labrador. <i>Nature</i> <b>349</b> , 209-214 (1991).
5	P. Hamilton, R. O'Nions, N. Evensen, <i>et al.</i> Sm-Nd isotopic investigations of Isua supracrustals and implications for mantle evolution. <i>Nature</i> <b>272</b> , 41-43 (1978).
6	G. Grau, B. M. John, A. Y. Gilkeson, R. D. Dyer, A. H. Hickman, C. Whang, Age of the Archean Tula-Tula Subgroup, Pilbara Block, Western Australia, and early evolution of the mantle: new Sm-Nd isotopic evidence. <i>Earth Planet. Sci. Lett.</i> <b>85</b> , 105-116 (1987).
7	S. Bowering, J. King, T. Hoare, <i>et al.</i> Neodymium and lead isotope evidence for enriched early Archean crust in North America. <i>Nature</i> <b>340</b> , 222-225 (1989).
8	S. Bowering, J. King, T. Hoare, <i>et al.</i> Neodymium and lead isotope evidence for enriched early Archean crust in North America. <i>Nature</i> <b>340</b> , 222-225 (1989).
9	N. W. Jones, S. Moorbath, P. N. Taylor, Age and origin of enclaves south of Anaralik, between Kanginuit-Sungmissig and Qasigimuit. In: Workshop: Early Crustal Genesis: the world's oldest rocks. Lunar and Planetary Institute Publication
10	P. J. Hamilton, N. M. Evensen, R. K. O'Nions, A. Y. Gilkeson, Sm-Nd dating of the North Star basalt, Warrawoona group, Pilbara block, Western Australia. <i>Spec. Publ. Geol. Soc.</i> <b>7</b> , 192-197 (1981).
11	P. J. Hamilton, N. M. Evensen, R. K. O'Nions, A. Y. Gilkeson, Sm-Nd dating of the North Star basalt, Warrawoona group, Pilbara block, Western Australia. <i>Spec. Publ. Geol. Soc.</i> <b>7</b> , 192-197 (1981).
12	H. Yuan, B. Zhai, D. J. DePaolo, Sm-Nd isotope study of early Archean rocks, Qianin, Hebei Province, China. <i>Geochim. Cosmochim. Acta</i> <b>59</b> , 625-631 (1986).
13	S. Tessaishi, B. Boudoin, M. Van Kesteren, <i>et al.</i> Influence of Hadean crust evident in basalts and cherts from the Pilbara Craton. <i>Nature Geosci.</i> <b>3</b> , 214-217 (2010).
14	B. M. John, B. Awwray, J. Corniche, Y. L. Bai, Q. H. Shen, D. Y. Liu, 3.5 Ga old amphiboles from eastern Hebei Province, China: field occurrence, petrography, Sm-Nd isochron age and REE geochemistry. <i>Precamb. Res.</i> <b>34</b> , 311-346 (1987).
15	This study.
16	R. Carlson, D. Hunter, F. Barker, Sm-Nd age and isotopic systematics of the bimodal suite, ancient gneiss complex, Swaziland. <i>Nature</i> <b>305</b> , 701-704 (1983).
17	M. Sharma, A. R. Basu, S. L. Ray, Sm-Nd isotopic and geochemical study of the Archean Tonilite-Amphibolite association from the eastern Indian Craton. <i>Contrib. Mineral. Petrol.</i> <b>117</b> , 45-55 (1994).
18	M. Sharma, A. R. Basu, S. L. Ray, Sm-Nd isotopic and geochemical study of the Archean Tonilite-Amphibolite association from the eastern Indian Craton. <i>Contrib. Mineral. Petrol.</i> <b>117</b> , 45-55 (1994).
19	I. R. Fletcher, J. K. R. Roaman, Sm-Nd geochronology of gresstone belts in the Yilgarn block, Western Australia. <i>Precamb. Res.</i> <b>26</b> , 333-361 (1984).
20	I. R. Fletcher, J. K. R. Roaman, Sm-Nd geochronology of gresstone belts in the Yilgarn block, Western Australia. <i>Precamb. Res.</i> <b>26</b> , 333-361 (1984).
21	E. Hejzler, A. Kröner, A. W. Hofmann, Age and isotopic geochemistry of the Archean Pongola and Ushabwana suites in Swaziland, southern Africa: a crust for crustal contamination of mantle-derived magmas. <i>Earth Planet. Sci. Lett.</i> <b>70</b> , 267-279 (1984).
22	P. Hamilton, N. Evensen, R. O'Nions, <i>et al.</i> Sm-Nd systematics of Levisian gneisses: implications for the origin of granulites. <i>Nature</i> <b>277</b> , 25-28 (1979).
23	A. Kumar, R. Bhaskar, Y. J. Sivaraman, Sm-Nd ages of Archean metapelites of the Dharwar craton, South India. <i>Precamb. Res.</i> <b>80</b> , 205-216 (1996).
24	This study.
25	N. W. Jones, S. Moorbath, P. N. Taylor, Age and origin of enclaves south of Anaralik, between Kanginuit-Sungmissig and Qasigimuit. In: Workshop: Early Crustal Genesis: the world's oldest rocks. Lunar and Planetary Institute Publication, 27-30 (1985).
26	S. Mungu, M. Muboko, Dating basaltic volcanism in the Neoproterozoic Sukumaland Greenstone Belt of the Tanzania Craton using the Sm-Nd method: implications for the geological evolution of the Tanzania Craton. <i>Preza</i>
27	D. DePaolo, G. J. Wasserburg, Sm-Nd age of the Stillwater complex and the mantle evolution curve for neodymium. <i>Geochim. Cosmochim. Acta</i> <b>43</b> , 999-1008 (1979).
28	J. Chouk-Long, M. Thirwall, R. Nesbitt, Revised Sm-Nd systematics of Kambalda gresstones, Western Australia. <i>Nature</i> <b>307</b> , 697-701 (1984).
29	I. R. Fletcher, J. K. R. Roaman, Sm-Nd geochronology of gresstone belts in the Yilgarn block, Western Australia. <i>Precamb. Res.</i> <b>26</b> , 333-361 (1984).
30	A. Zindler, C. Brooks, N. T. Arndt, Pb and Nd isotopic study of two Archean komatiite flows from Alexo, Ontario. <i>Geochim. Cosmochim. Acta</i> <b>48</b> , 1965-1972 (1984).
31	B. Dyrce, C. Chauvel, N. T. Arndt, Pb and Nd isotopic data from komatiite and tholeiitic rocks of Munro Township, Ontario. In: Zartman RE (ed) Short papers of the Fourth International Conference on Geochronology, Cosmochronology and Isotope Geology. <i>US Geol. Surv. Open-File Report</i> <b>78</b> , 701-469-701 (1978).
32	S. B. Shirey, G. N. Hanson, Mantle heterogeneity and crustal recycling in Archean granite-gresstone belts: Evidence from Nd isotopes and trace elements in the Ratny Lake area, Superior Province, Ontario, Canada. <i>Geochim. Cosmochim. Acta</i> <b>50</b> , 2631-2651 (1986).
33	A. R. Basu, A. M. Goodwin, M. Tatumoto, Sm-Nd study of Archean alkalic rocks from the Superior Province of the Canadian Shield. <i>Earth Planet. Sci. Lett.</i> <b>70</b> , 40-46 (1984).
34	J. D. Vervoort, W. M. White, R. I. Thorpe, Nd and Pb isotope ratios of the Abitibi gresstone belt: new evidence for very early differentiation of the Earth. <i>Earth Planet. Sci. Lett.</i> <b>128</b> , 215-229 (1994).
35	P. J. Hamilton, R. K. O'Nions, N. M. Evensen, Sm-Nd dating of Archean Basic and Ultramafic Volcanics. <i>Earth Planet. Sci. Lett.</i> <b>36</b> , 263-268 (1977).
36	B. M. John, W. G. Ernst, Late Archean Sm-Nd isochron age for mafic-ultramafic supracrustal amphibolites from the Northeastern Sino-Korean Craton, China. <i>Precamb. Res.</i> <b>46</b> , 295-306 (1990).
37	B. K. Nelson, D. J. DePaolo, Rapid production of continental crust 1.7 to 1.9 by ago: Nd isotopic evidence from the basement of the North American mid-continent. <i>Geol. Soc. Amer.</i> <b>96</b> , 746-754 (1985).
38	B. Faggart, A. Basu, M. Tatumoto, Origin of the Stillwater Complex by Meteorite Impact: Neodymium Isotopic Evidence. <i>Science</i> <b>291</b> , 193-196 (1991).
39	D. DePaolo, Neodymium isotopes in the Colorado Front Range and crust-mantle evolution in the Proterozoic. <i>Nature</i> <b>354</b> , 384-387 (1991).
40	W. Sivel, M. McCulloch, Neodymium isotope evidence for ultra-depleted mantle in the early Proterozoic. <i>Nature</i> <b>354</b> , 384-387 (1991).
41	B. Nelson, D. DePaolo, 1.700-Myr gresstone volcanic successions in southwestern North America and isotopic evolution of Proterozoic mantle. <i>Nature</i> <b>312</b> , 143-146 (1984).
42	R. F. Emalie, M. A. Hamilton, R. J. Theriault, Petrogenesis of a Mid-Proterozoic Anorthositic-Mangite-Charnockite-Granite (AMCG) Complex: Isotopic and Chemical Evidence from the Nam Plutonic Suite. <i>J. Geol.</i> <b>102</b> , 539-558 (1994).
43	A. R. Basu, H. S. Peitangill, Origin and age of Adirondack anorthositic re-evaluated with Nd isotopes. <i>Geology</i> <b>9</b> , 514-518 (1983).
44	C. J. Allegre, D. Rousseau, The growth of the continent through geological time studied by Nd isotope analysis of shales. <i>Earth Planet. Sci. Lett.</i> <b>67</b> , 19-34 (1984).
45	M. T. McCulloch, R. T. Gregory, G. J. Wasserburg, H. P. Taylor, Sm-Nd, Rb-Sr, 180/160 isotopic systematics in an oceanic enst. section: evidence from the Semai ophiolite. <i>J. Geophys. Res.</i> <b>86</b> , 2721-2735 (1981).
46	S. J. Goldstein, S. B. Jacobsen, Nd and Sr isotope systematics of river water suspended material: implications for crustal evolution. <i>Earth Planet. Sci. Lett.</i> <b>87</b> , 249-265 (1988).
47	D. J. DePaolo, Neodymium isotopes in the Colorado Front Range and crust-mantle evolution in the Proterozoic. <i>Nature</i> <b>291</b> , 193-196 (1981).
48	D. J. DePaolo, Neodymium isotopes in the Colorado Front Range and crust-mantle evolution in the Proterozoic. <i>Nature</i> <b>291</b> , 193-196 (1981).
49	S. Kerr, W. J. Collins, M. T. McCulloch, A three-component Sr-Nd isotopic mixing model for granuloid gneiss, Lachlan fold belt, eastern Australia. <i>Geology</i> <b>25</b> , 307-310 (1997).
50	D. J. DePaolo, G. J. Wasserburg, Nd and Sr isotope systematics of the Stillwater complex and the mantle evolution curve for neodymium. <i>Geochim. Cosmochim. Acta</i> <b>43</b> , 999-1008 (1979).
51	S. Jacobsen, Dymek, R., Nd and Sr isotope systematics of classic metasediments from Isua, West Greenland: Identification of pre-3.8 Ga differentiated crustal components. <i>Journal of Geophysical Research</i> <b>93</b> , 338-354 (1988).
52	DeChaille, V., O'Neill, C., Brandon, A.D. <i>et al.</i> Stagnant-ild tectonics in early Earth revealed by 142Nd variations in late Archean rocks. <i>Earth Planet. Sci. Lett.</i> <b>373</b> , 83-92 (2013).
53	Locht, S., Hoffmann, J., Rosting, M., Spreng, P., Munker, C. Preservation of Eoarchean mantle processes in 3.8 Ga peridotite enclaves in the Isua Gneiss Complex, Southwest Greenland. <i>Geochimica Cosmochimica Acta</i> , 280, 1-25 (2020).

## REFERENCES

- Acharyya, S.K., Gupta, A. and Orihashi, Y., New U-Pb zircon ages from Paleo-Mesoarchean TTG gneisses of the Singhbhum craton, eastern India. *Geochemical Journal*. **44**, 81-88 (2019).
- Agrinier, P., Javoy, M, Girardeau, J. Hydrothermal activity in a peculiar oceanic ridge: oxygen and hydrogen isotope evidence in the Xigaze ophiolite (Tibet, China). *Chemical Geology*, **71**, 313-335 (1988).
- Albarede, F. The growth of continental crust. *Tectonophysics*. **296**, 1-14 (1998).
- Al-Aasm, IS., Taylor, B.E., South, B. Stable isotope analysis of multiple carbonate samples using selective acid extraction. *Chem. Geol.*, **80**, 119-125 (1990).
- Albarede F. and Beard B. L. Analytical methods for non-traditional isotopes. In *Geochemistry of Non-Traditional Stable Isotopes* (eds. C. M. Johnson, B. L. Beard and F. Albarede). Mineralogical Society of America and Geochemical Society, Washington, DC, 113–152 (2004).
- Alibert, C., McCulloch, M.T. Rare earth element and Nd isotopic compositions of the banded iron formations and associated shales from Hamersley, Western Australia. *Geochim. Cosmochim. Acta*. **57**, 187-204 (1993).
- Allegre, C.J., Rousseau, D., The growth of the continent through geological time studied by Nd isotope analysis of shales. *Earth Planet. Sci. Lett*, **67**, 19-34 (1984).
- Allègre, C. J. Isotope geology. Cambridge University Press 512 (2008).
- Allwood, A., Walter, M., Kamber, B. *et al.* Stromatolite reef from the Early Archaean era of Australia. *Nature* **441**, 714–718 (2006).
- Amelin, Y., Lee, D.-C., Halliday, A.N., & Pidgeon, R.T. (1999): Nature of the Earth's earliest crust from hafnium isotopes in single detrital zircons. *Nature*, **399**, 252–255 (1999).
- Anbar, A. D., Duan, Y., Lyons, T. W., Arnold, G. L., Kendall, B., Creaser, R. A., ... & Buick, R. A whiff of oxygen before the great oxidation event?. *Science*, **317**(5846), 1903-1906 (2007).
- Anbar, A. D., et al. A Whiff of Oxygen Before the Great Oxidation Event? *Science*. **317**, 1903-1906 (2007).
- Armstrong, R.L. The persistent myth of crustal growth. *Aust. J. Earth sci.* **38**, 613-630 (1991)
- Arndt, N. T., & Goldstein, S. L. Use and abuse of crust-formation ages. *Geology*, **15**(10), 893-895 (1987).

- Asokan, A. D., Mahapatro, S. N., Mohan, M. R., ocholl, A. R., Wiedenbeck, M., Nanda, J. K.. Paleoproterozoic evolution of the Singhbhum Craton, eastern India: New constraints from geochemistry and geochronology of granitoids of Bonai and Champua area. *Precamb. Res.* **366**, 106429 (2021).
- Avasthy, R.K. Stromatolites from Iron Ore formation of Bhopal-Keonjhar District, Orissa, India. *Geological Survey of India, Miscellaneous Publications*, **44**, 54-56 (1980).
- Avila, C. F., Archanjo, C. J., Hollanda, M. H. B., de Macedo Filho, A. A., & Lemos-Santos, D. D. V. Shear zone cooling and fabrics of synkinematic plutons evidence timing and rates of orogenic exhumation in the northwest Borborema Province (NE Brazil). *Precambrian Research*, **350**, 105940 (2020).
- Bachhar, P., Saha, D., Santosh, M., Liu, H.D., et al. Mantle heterogeneity and crust-mantle interaction in the Singhbhum craton: New evidence from 3340 Ma Komatiites. *Lithos*, **105931**, 382-383 (2021).
- Bandopadhyay, P. C., Eriksson, P. G. and Roberts, R. J. A vertic paleosol at the Archean-Proterozoic contact from the Singhbhum-Orissa craton, eastern India. *Precambrian Research*, **177**, 277-290 (2010).
- Banerji, A.K., On the Precambrian banded iron formation and the manganese ores of the Singhbhum region, Eastern India. *Economic Geology*, **72**, 90-98 (1977).
- Banerjee, S. *Stable Isotope Constraints on Global Cycles* (3438847). Available from Dissertations & Theses @ Southern Methodist University; ProQuest Dissertations & Theses Global. (849716913).
- Bandyopadhyay, P. K., Chakrabarti, A. K., Deomurari, M. P. & Misra, S. 2.8 Ga old anorogenic granite-acid volcanic association from western margin of Singhbhum-Orissa craton, eastern India. *Gondwana Research*, **4**, 465-475 (2001).
- Balsley, S.D., Gregory, R.T. Low  $^{18}\text{O}$  silicic magmas: why are they so rare? *Earth. Planet. Sci. Lett.* **162**, 123-136 (1998).
- Barley, M., Pickard, A. & Sylvester, P. Emplacement of a large igneous province as a possible cause of banded iron formation 2.45 billion years ago. *Nature* **385**, 55-58 (1997).
- Barron, E. J., & Washington, W. M. (1984). The role of geographic variables in explaining paleoclimates: Results from Cretaceous climate model sensitivity studies. *Journal of Geophysical Research: Atmospheres*, **89**(D1), 1267-1279.
- Baur, A.M., Reimink, J.R. Chacko, T., Foley, B.J., Shirey, S.B., Pearson, D.G., Hafnium isotopes in zircons document the gradual onset of mid-lid tectonics. *Geochemical Perspectives Letters*, **14**, 1-6 (2020).
- Basu, A. R., Ray, S. L., Saha, A. K., Sarkar, S. N. Eastern India 3800-Million-Year-Old Crust and Early Mantle Differentiation. *Science* **212**, 1502-1506 (1981).

- Basu, A. R., Bandyopadhyay, P. K., Chakrabarty, R., Zhou, H. Large 3.4 Ga Algoma Type BIF in the Eastern Indian Craton. In: Goldschmidt Conference Abstracts, Vancouver. *Geochim. Cosmochim. Acta*, **72**, A59 (2008).
- Basu, A.R., Sharma, M., Premo, W.R. U-Pb age of an older metamorphic group mica-schist: earliest terrain of the eastern Indian craton. In: Saha, A.K. (eds) recent Researches in geology and geophysics of the Precambrian. Essays in Honor of Prof. Samarendra Nath Sarkar on his seventy-fifth birth anniversary. 16, 93-102 (1996).
- Basu, A. Petrology of Holocene fluvial sand derived from plutonic source rocks; implications to paleoclimatic interpretation. *Journal of Sedimentary Research*, **46**, 694-709 (1976).
- Beaty, D.W. The oxygen isotope geochemistry of the Abitibi greenstone belt. *PhD thesis. Cal Tech* (1980).
- Beard B. L., Johnson C. M., Skulan J. L., Nealson K. H., Cox L. and Sun H. Application of Fe isotopes to tracing the geochemical and biological cycling of Fe. *Chem. Geol.* **195**, 87–117 (2003).
- Beck, J.W., Berndt, M.E., Seyfried, W.E. Jr. Application of isotopic doping techniques to evolution of reaction kinetics and fluid/ mineral distribution coefficients: An experimental study of calcite at elevated temperatures and pressures. *Chem. Geol.* **97**, 125-144 (1992).
- Becker, R.H., Clayton, R.N. Oxygen isotope study of a Precambrian banded iron formation, Hamersley Range, Western Range. *Geochimica et Cosmochimica*, **40**, 1153-1165 (1976).
- Bédard, J. H. Stagnant lids and mantle overturns: Implications for Archean tectonics, magmagenesis, crustal growth, mantle evolution, and the start of plate tectonics. *Geoscience Frontiers*, **9**(1), 19-49 (2018).
- Berg, S.E., et al., Exceptionally high whole-rock  $\delta^{18}\text{O}$  values in intra-caldera rhyolites from Northeast Iceland. *Mineralogical magazine*. **82**, 1147-1168 (2018).
- Beukes, N. J., Mukhopadhyay, J., Gutzmer, J., Genesis of high-grade iron ores of the Archean iron ore group around Noamundi, India. *Economic Geology*, **103**, 365-386 (2008).
- Bickle, M.J., Nisbet, E.G., Martin, A. Archean Greenstone Belts are not oceanic crust. *The Journal Geology*, **102**, 121-138 (1994).
- Bindeman, I.N. Triple oxygen isotopes in evolving continental crust, granites, and clastic sediments. *Reviews in mineralogy and Geochemistry*. **86**, 241-290 (2021).
- Bindeman, I.N., Valley, J.W. Formation of low  $\delta^{18}\text{O}$  rhyolites after caldera collapse at Yellowstone, Wyoming, USA. *Geology*, **28**, 719-722 (2000).
- Bindeman, I.N. Schmitt, A.K., Evans, D.A.D. Limits of hydrosphere interaction: Origin of the lowest known  $\delta^{18}\text{O}$  silicate rock on Earth in the Paleoproterozoic Karelian rift. *Geol. Soc. of America* **38**, 631-634 (2010).

- Bindeman, I., Gurenko, A., Carley, T., Miller, C., Martin, E., Sigmarsson, O. Silicic magma petrogenesis in Iceland by remelting of hydrothermally altered crust based on oxygen isotope diversity and disequilibria between zircon and magma with implications for MORB. *Terra Nova* **24**, 227-232 (2012).
- Bowers, T., Taylor, H. An Integrated chemical and stable isotope model of the Origin of Mid-Ocean Ridge Hot Spring Systems. *Journal of Geophysical Research*. **90**, 12583-12606 (1985).
- Bottinga, Y., Javoy, M. Comments on oxygen isotope geothermometry. *Earth Planet. Sci. Lett.* **20**, 250 (1973).
- Borg, L.E., Connelly, J.N., Boyet, M., Carlson, R.W. Chronological evidence that the Moon is either young or did not have a global magma ocean. *Nature*. **477**, 70-72 (2011).
- Borg, L.b., Brennecka, G.A., Symes, S.J.K. Accretion timescale and impact history of Mars deduced from the isotopic systematics of martian meteorites. *Geochimica Cosmochimica Acta*. **175**, 150-167 (2016).
- Borg, L.E., Nyquist, L.E., Wiesmann, H., Reese, Y. Constraints on the petrogenesis of Martian meteorites from the Rb-Sr and Sm-Nd isotopic systematics of the Iherzolite shergottites ALH77005 and LEW88516. *Geochimica Cosmochimica Acta*. **66**, 2037-2053 (2002).
- Boyet, M., Carlson, R.W. <sup>142</sup>Nd Evidence for early (>4.53 Ga) global differentiation of the early silicate Earth. *Science* **309**, 576-581 (2005).
- Bowering, S.A., Housh, T. The Earth's Early Evolution. *Science*. **269**, 1535-1540 (1995).
- Black, L. P., Kamo, S. L., Allen, C. M., Davis, D. W., Aleinikoff, J. N., Valley, J. W., ... & Foudoulis, C. Improved <sup>206</sup>Pb/<sup>238</sup>U microprobe geochronology by the monitoring of a trace-element-related matrix effect; SHRIMP, ID-TIMS, ELA-ICP-MS and oxygen isotope documentation for a series of zircon standards. *Chemical Geology*, **205**, 115-140 (2004).
- Blatt, H., Jones, R. L. Proportions of exposed igneous, metamorphic, and sedimentary rocks. *Geol. Soc. Am. Bull.* **86**, 1085 (1975).
- Blatt, H., 1967, Original characteristics of clastic quartz grains: *Jour. Sed. Petrology*, **37**, 401-424.
- Blichert-Toft, J. & Albarède, F. The Lu-Hf isotope geochemistry of chondrites and the evolution of the mantle-crust system. *Earth Planet. Sci. Lett.*, **148**, 243-258 (1997).
- Brenner, A.R., Fu, R.R., Evans, D.A.D., Smirnov, A.V., Trubko, R., Rose, I.R. Paleomagnetic evidence for modern-like plate motion velocities at 3.2 Ga. *Science Advances*, **6**, [10.1126/sciadv.aaz8670](https://doi.org/10.1126/sciadv.aaz8670) (2020).
- Broecker, W.S., Peng, T.H. Tracers in the Sea. *Eldigo Press, New York*, pp.1-690 (1982).

- Brooks, C., Hart, S. R., & Wendt, I. (1972). Realistic use of two-error regression treatments as applied to rubidium-strontium data. *Reviews of Geophysics*, **10**, 551-577 (1972).
- Busigny, V. et al., Iron isotopes in an Archean Ocean analogue. *Geochimica et Cosmochimica Acta*, **133**, 443-462 (2014).
- Burdett, J.W., Grotzinger, J.P., Arthur, M.A. Did major changes in the isotopic composition of Proterozoic seawater occur? *Geology*, **18**, 227-230 (1990).
- Cameron, E.M., Garrels, R.M. Geochemical compositions of some Precambrian shales from the Canadian Shield. *Chemical Geology*. **28**, 181-197 (1980).
- Campbell, I., St C. O'Neill, H. Evidence against a chondritic Earth. *Nature* **483**, 553–558 (2012).
- Campbell, I.H., Taylor, S.R., NO WATER, NO GRANITES- NO OCEANS, NO CONTINENTS. *Geo. Phys. Res. Lett.* **11**, 1061-1064 (1983).
- Campbell, I, H., Jarvis. T., 1984. Mantle convection and early crustal evolution. *Precambrian Res.* **26**, 15-56.
- Campbell, I. H., Davies, D. R. Raising the continental crust. *Earth Planet. Sci. Lett.* **460**, 11-122 (2017).
- Canet et al., Silica-carbonate stromatolites related to coastal hydrothermal venting in Bahia Concepcion, Baja California Sur, Mexico. *Sedimentology Geology*, **174**, 97-113 (2005).
- Carlson, R., Boyet, M., Composition of the Earth's interior: the importance of early events. *Phil. Trans. R. Soc. A.* **366**, 4077-4103 (2008).
- Cawood, P.A., Hawkesworth, C.J., Dhuime, B. The continental record and the generation of continental crust. *GSA Bulletin*, **125** (1-2): 14–32 (2013).
- Chaudhuri, T., Satish-Kumar, M., Mazumder, R., Biswas, S. Geochemistry and Sm-Nd isotopic characteristics of the Paleoarchean Komatiites from Singhbhum Craton, Eastern India and their Implications. *Precambrian Research*, **298**, 385-402 (2017).
- Chaudhuri, T. A review of Hadean to Neoarchean crust generation in the Singhbhum Craton, India and possible connection with Pilbara Craton, Australia: The geochronological perspective. *Earth Science Reviews.* **202**, 103085 (2020).
- Chaudhuri, T., Kamei, A., Das, M., Mazumder, R., Owada, M., Evolution of the Archean felsic crust of Singhbhum Craton, India: A reassessment. *Earth-Science Reviews.* **231**, 104067 (2022).
- Chaudhuri, T., Wan, Y., Mazumder, R., Ma, M., & Liu, D. Evidence of enriched, Hadean mantle reservoir from 4.2-4.0 Ga zircon xenocrysts from Paleoarchean TTGs of the Singhbhum Craton, Eastern India. *Scientific reports*, **8**, 7069 (2018).

- Chakrabarti, A., Bandyopadhyay, P. K. & Chakrabarty, A. K. Rounded fresh feldspar in the Late Archaean nearshore deposits around Patasahi, Orissa: glacial activity? *Indian Journal of Earth Sciences*, **25**, 94-107 (1998).
- Chaki, A., Bhattacharya, D., Rao, J. S., Chaturbedi, A. K. & Bagchi, A. K. Geochronology of the granitoids of Kunjar area, Sundargarh District, Orissa: implications to the regional stratigraphy. *Journal of the Geological Society of India*, **65**, 428-440 (2005).
- Chavagnac, V., A geochemical and Nd isotopic study of Barberton komatiites (South Africa): Implications for the Archean mantle: *Lithos*, **75**, 253–281 (2004).
- Chazot, G., Lowry, D., Menzies, M. & Matthey, D. Oxygen isotopic composition of hydrous and anhydrous mantle peridotites. *Geochim. Cosmochim. Acta* **61**, 161-169 (1997).
- Chowdhury, P., Mulder, J.A., Cawood, P.A., Bhattacharjee, S., Roy, S., Wainwright, A.N., Nebel, O., Mukherjee, S. Magmatic thickening of crust in non-plate tectonic settings initiated the subaerial rise of Earth's first continents 3.3 to 3.2 billion years ago. *Proc. Natl. Acad. Sci.* **118** (2021).
- Cisneros-Lazaro, D., Adams, A., Guo, J. *et al.* Fast and pervasive diagenetic isotope exchange in foraminifera tests is species-dependent. *Nat Commun* **13**, 113 (2022).
- Clark, F.W. Data of Geochemistry. *Bull. U.S. Geol. Survey.* **770** (1924).
- Clayton, R.N., Mayeda, T.K. The use of bromine pentafluoride in the extraction of oxygen from oxides and silicates for isotopic analysis: *Geochemica et Cosmochimica Acta*, **27**, 43-52 (1963).
- Clayton, R.N., O'Neill, J.R., Mayeda, T.K. Oxygen isotope exchange between quartz and water. *Journal of Geophysical Research* **77**, 3057-3067 (1972).
- Cloud, P., Licar, G. Microbiotas of the Banded Iron Formations. *Proc. Nat. Acad. Sci.* **61**, 779-786 (1968).
- Cloud, P. Chapter 10 Banded Iron Formation- A gradualist's Dilemma. *Developments in Precambrian Geology*, **6**, 401-416 (1983).
- Cloud, P. Paleoecological significance of the banded iron formation. *Economic Geology*, **68**, 1135-1143 (1973).
- Collerson, K. D., Campbell, L. M., Weaver, B. L., Palacz, Z. A. Evidence for extreme mantle fractionation in early Archean ultra-mafic rocks from Northern Labrador. *Nature* **349**, 209–214 (1991).
- Condie, K., Pease, V. When did plate tectonics began on Earth? *Geological Society of America Special Paper*, **440** (2008).
- Condie, K. C. *Earth as an evolving planetary system*. Academic Press (2021).

- Compson, W., Williams, I. S., Meyer, C. U-Pb geochronology of zircons from lunar breccia 73217 using a sensitive high mass-resolution ion microprobe. *J. Geophys. Res.* **89**, 525-534 (1984).
- Craddock, P. R., & Dauphas, N. Iron isotopic compositions of geological reference materials and chondrites. *Geostandards and Geoanalytical Research*, **35**, 101-123 (2011).
- Craig, H. Isotopic variations in meteoric waters. *Science*, **133**, 1702-1703 (1961).
- Criss, R.E., Taylor, H.P. An  $^{18}\text{O}/^{16}\text{O}$  and D/H study of terrestrial hydrothermal systems in the southern half of the Idaho batholith. *Geol. Soc. Amer. Bull.* **94**, 640-663, (1983).
- Criss, R.E., Gregory, R.T., Taylor, H.P., Kinetic-theory of oxygen isotopic ex-change between minerals and water. *Geochim. Cosmochim. Acta* **51**, 1099–1108 (1987).
- Criss, R. E. *Principles of stable isotope distribution*. Oxford University Press (1999).
- Dauphas, N., Rouxel, O., Mass Spectrometry, and natural variations of iron isotopes. *Mass Spec. Rev.* **25**, 515-550 (2006).
- Debaille, V., Yin, Q.Z., Brandon, A.D., Jacobsen, B. Martian mantle mineralogy investigated by the  $^{176}\text{Lu}$ - $^{176}\text{Hf}$  and  $^{147}\text{Sm}$ - $^{143}\text{Nd}$  systematics of shergottites. *Earth Planet. Sci. Lett.* **269**, 186-199 (2008).
- DePaolo, D. J., Wasserburg, G. J. The sources of island arcs as indicated by Nd and Sr isotopic studies. *Geophys. Res. Lett.* **4**, 465-468 (1977).
- DePaolo, D. J., Wasserburg, G. J. Sm-Nd age of the Stillwater Complex and the mantle evolution curve for neodymium. *Geochimica et Cosmochimica Acta.* **43**, 999-1008 (1979).
- DePaolo, D. J. Neodymium isotopes in the Colorado Front Range and crust-mantle evolution in the Proterozoic. *Nature* **291**, 193-196 (1981).
- DePaolo, Donald J. The mean life of continents: Estimates of continent recycling rates from Nd and Hf isotopic data and implications for mantle structure: *Geophys. Res. Lett.*, **10** (8). 705-708(1983).
- DePaolo, D. J., & Wasserburg, G. J. Nd isotopic variations and petrogenetic models. *Geophysical research letters*, **3**, 249-252 (1976).
- DePaolo, D.J., Linn, A.M., Schubert, G. The continental crust age distribution: Methods of determining mantle separation ages from Sm-Nd isotopic data and application to the Southwestern United States. *Journal of Geophysical Research.* **96**, 2071-2088 (1991).
- DePaolo, D. J. *Neodymium isotope geochemistry: an introduction* (Vol. 20). Springer Science & Business Media (2012).
- Dey, S., Topno, A., Liu, Y., Zong, K. Generation and evolution of Paleoproterozoic continental crust in the central part of the Singhbhum craton, eastern India. *Precamb. Res.* **298**, 268-291 (2017).

- De, S., Rosiere, C.A., Mukhopodhyay, J. Detrital zircon LA-ICPMS-U-Pb and Lu-Hf signature from the Mesoarchean Keonjhar Quartzite: Implications for the nature of Archean continental crust and geodynamics. *Geosystems and Geoenvironment*, **1**, 100057 (2022).
- Derry, L.A., and Jacobsen, S.B. The chemical evolution of Precambrian seawater—evidence from REEs in banded iron formations: *Geochim. Cosmochim. Acta.* **54**, 2965–2977 (1990).
- Dickin, Alan P. *Radiogenic isotope geology*. Cambridge university press, 2018.
- Dreher et al., Impact of silica and iron concentrations on microbial iron cycling in the Archean during the genesis of Banded Iron Formations. Goldschmidt abstract (2023).
- Dunn, J.A., The geology of North Singhbhum, including parts of Ranchi and Manbhum districts. *Mem. Geol. Surv. India.* **54**, 166 (1929).
- Dunn, J.A., The origin of iron ores in Singhbhum, India. *Economic Geology*, **30**, 643-654 (1935).
- Dunn, J.A., The origin of banded hematite ores. *Economic Geology*, **36**, 355-370 (1941).
- Dunn, J.A., Dey, A.K., The geology and petrology of eastern Singhbhum and surrounding areas. *Memoir Geologic Survey of India*, **69**, 281-456 (1942).
- Dunn, J. A. The Stratigraphy of south Singhbhum: *Geol. Surv. India. Mem.* **63**, 303-309 (1940).
- Elderfield, H., Greaves, H.J. The rare earth elements in seawater. *Nature*, **296**, 214-219 (1982).
- Eggins, S.M., Grün, R., McCulloch, M.T., Pike, A.W.G., Chappell, J., Kinsley, L., Mortimer, G., Shelley, M., Murray-Wallace, C.V., Spötle, C., Taylor, L. In situ U-series dating by laser-ablation multi-collector ICPMS: new prospects for Quaternary geochronology. *Quaternary Science Reviews* **24**, 2523–2538 (2005).
- Eriksson, P.G. Sea level changes and the continental freeboard concept: general principles and application to the Precambrian. *Precambrian Research*, **97**, 143-154 (1999).
- Eriksson, K. A., Krapez, B, Fralick, P.W. Sedimentology of Archean greenstone belts: Signatures of tectonic evolution. *Earth-Science Rev.* **34**, 1-88 (1994).
- Eugster, H.P., Chou, I-M. The depositional environments of Precambrian banded iron-formations. *Economic Geology*, **68**, 1144-1168 (1973).
- Fanale, F.P. A case for catastrophic early degassing of the earth. *Chemical Geology*, **8**, 79-105 (1971).
- Faure, K., & Harris, C. Oxygen and carbon isotope geochemistry of the 3.2 Ga Kaap Valley tonalite, Barberton greenstone belt, South Africa. *Precambrian Research*, **52**(3-4), 301-319 (1991).

- Fedo, C.M., Myers, J.S., Appel, P.W. Depositional setting and paleogeographic implications of Earth's oldest supracrustal rocks, the >3.7 Ga Isua Greenstone belt, West Greenland. *Sedimentary Geology*, **141-142**, 61-77 (2001).
- Fedo, C., Eriksson, K.A., Krogstad, E. Geochemistry of shales from the Archean (~3.0 Ga) Buhwa Greenstone Belt, Zimbabwe: Implications from provenance and source-area weathering. *Geochimica et Cosmochimica Acta*. **60**, 1751-1763 (1996).
- Fedo, C.M., Sircombe, K.N., and Rainbird, R.H. Detrital zircon analysis of the sedimentary record: *Reviews in Mineralogy and Geochemistry* **53**, 277-303 (2003).
- Fisher, C.M., Hanchar, J.M., Samson, S.D., Dhuime, B., Blichert-Toft, J., Vervoort, J.D., Lam, R., Synthetic zircon doped with hafnium and rare earth elements: A reference material for in situ hafnium isotope analysis. *Chemical Geology* **286**, 32-47 (2011).
- Fisher, C. M., Vervoort, J. D., & Hanchar, J. M. Guidelines for reporting zircon Hf isotopic data by LA-MC-ICPMS and potential pitfalls in the interpretation of these data. *Chemical Geology* **363**, 125-133 (2014).
- Foster, D.A, Gray, D.R., Evolution and structure of the Lachlan Fold Belt (orogen) of Eastern Australia: *Ann. Rev. Earth Planet. Sci.* **28**, 47-80 (2000).
- Frost, C.D., Mueller, P.A., Mogk, D.W., Frost, B.R., Henry, D.J. Creating continents: Archean cratons tell the story. *GSA Today*, **33**, 4-10 (2023).
- Friedman, I., J. R. O'Neil, *Compilation of stable isotope fractionation factors of geochemical interest*, U.S. Geol. Surv. Prof. Pap., **440-KK**, 1977.
- Friedrichsen, H. Strontium, oxygen, and hydrogen isotope studies on primary and secondary minerals in basalts from the Costa Rica Rift, Deep Sea Drilling Project Hole 504B, Leg 83. In: *Anderson, RN; Honnorez, J; Becker, K; et al. (eds.), Initial Reports of the Deep Sea Drilling Project, Washington (U.S. Govt. Printing Office)*, **83**, 289-295, (1985).
- Francois, R. The origin of water on Earth. *Science*, **293**, 1056-1058 (2001).
- Furnes, H., de Wit, M., Staudigel, H., Rosing, M., Muehlenbachs, v. A vestige of earth's oldest ophiolite. *Science*. **315**, 1704-1707 (2007).
- Fu, B., Bröcker, M., Ireland, T., Holden, P., & Kinsley, L. P. Zircon U–Pb, O, and Hf isotopic constraints on Mesozoic magmatism in the Cyclades, Aegean Sea, Greece. *International Journal of Earth Sciences*, **104**, 75-87 (2015).
- Galili, N., et al., The geologic history of seawater oxygen isotopes from marine iron oxides. *Science* **365**, 469–473 (2019).
- Gannoun, A., Suchorski, K., Pin, C., A fast, single column extraction chromatography method for the isolation of neodymium from iron-rich materials prior to radiogenic isotope ratio measurements, *J. Anal. At. Spectrom.*, **37**, 165 (2022).

- Gardiner, N.J., Kirkland, C.L., Van Kranendonk, M.J. The Juvenile Hafnium Isotope Signal as a Record of Supercontinent Cycles. *Sci. Rep.* **6**, 38503; doi: 10.1038/srep38503 (2016).
- Ghosh, S., Mukhopadhyay, J., & Chakraborty, A. Clay mineral and geochemical proxies for intense climate change in the permian gondwana rock record from eastern india. *Research* (2019).
- Gill, R. *Chemical fundamentals of geology and environmental geoscience*. John Wiley & Sons (2015).
- Goldstein, S. J., Jacobsen, S. B. Nd and Sr isotopic systematics of river water suspended material: implications for crustal evolution. *Earth Planet. Sci. Lett.* **87**, 249-265 (1988).
- Goldstein, S.L., O’Nion’s, R.K., Hamilton, P.J., A Sm-Nd study of atmospheric dusts and particles from major river systems. *Earth Planet. Sci. Lett.* **70**, 221-236 (1984).
- Goodwin, J.W., Archean Ion-formation and tectonic basins of the Canadian Shield. *Economic Geology*, **68**, 915-933 (1956).
- Goudie, A.S., Middleton, N.J. Saharan dust storms: nature and consequences. *Earth-Science Reviews.* **56**, 179-204 (2001).
- Graham, C.M., Sheppard, S.M.F., Heaton, T.H.E. Experimental hydrogen isotope studies I: Systematics of hydrogen isotope fractionation in the systems epidote-H<sub>2</sub>O, zoisite-H<sub>2</sub>O and AlO(OH)-H<sub>2</sub>O. *Geochimica et Cosmochimica Acta* **44**, 353-364 (1980).
- Grant, P.R., Murty, V. N., Sengupta, S. The first record of stromatolites from the Koira Group (Iron Ore Series) Precambrian of Bihar—Orissa, India. *Geological Survey of India Miscellaneous Publications*, **44**, 49-53 (1980).
- Gray, D.R., Gregory, R.T., Durney, D.W., Rock-buffered fluid-rock interaction in deformed quartz-rich turbidite sequences, eastern Australia: *J. Geophys. Res.* **96**, 19,681-19,704 (1991).
- Gray, D.R., Foster, D.A., Maas, R., Spaggiari, C.V., Gregory, R.T., Goscombe, B., and Hoffmann, K.H., Continental growth and recycling by accretion of deformed turbidite fans and remnant ocean basins: Examples from Neoproterozoic and Phanerozoic orogens, in Hatcher, R.D., Jr., Carlson, M.P., McBride, J.H., and Martínez Catalán, J.R., eds., 4-D Framework of Continental Crust: *Geological Society of America Memoir* **200**, 63–92 (2007).
- Gregory, R.T. Oxygen isotope history of seawater revisited: 3.5 billion years of the greenstone record and its implication for the stability of seawater<sup>18</sup>O, in H.P. Taylor, Jr., J.R. O’Neil, and I.R. Kaplan (eds.) *Stable Isotope Geochemistry: A Tribute to Samuel Epstein, Geochemical Society Special Publication* 3, 65-76 (1991).
- Gregory, R. T., Taylor Jr, H. P. An oxygen isotope profile in a section of Cretaceous oceanic crust, Samail Ophiolite, Oman: Evidence for  $\delta^{18}\text{O}$  buffering of the oceans by deep (>5 km) seawater-hydrothermal circulation at mid-ocean ridges. *J. Geophys. Res. Solid Earth* **86**, 2737–2755 (1981).

- Gregory, R.T. Stable isotopes as tracers of global cycles. *Enc. Phy. Sci. and Tech.* **15**, 695-714 (2003).
- Gregory, R. T. Ophiolites and global geochemical cycles: Implications for the isotopic evolution of seawater. *Geol. Soc. Lond. Spec. Publ.* **218**, 353–368 (2003).
- Gregory, R.T, Criss, R.E., Taylor, H.P. Oxygen isotope exchange kinetics of minerals pairs on closed and open systems: applications to problems of hydrothermal alteration of igneous rocks and Precambrian iron formations. *Chemical Geology*, **75**, 1-42 (1989).
- Gregory, R.T., Richards, I.J., Ferguson, K.M. Hydrogen, carbon, and oxygen isotope ratios from the Archean Pilbara Block: Constraints on geological cycles. *Geochim, Cosmochim. Acta.* **70**, A217 (2006).
- Gregory, R.T., Oxygen isotope systematics of Quartz-Magnetite pairs from Precambrian Iron Formations: Evidence for fluid-rock interactions during diagenesis and metamorphism. In: J.V. Walther and B.J. Wood (Editors), Fluid-rock interaction during metamorphism. *Springer, New York, N.Y.*, 32-153 (1986).
- Griffin, W.L., Pearson, N.J., Belousova, E., Jackson, S.E., van Achterbergh, E., O'Reilly, S.Y. & Shee, S.R. The Hf isotope composition of cratonic mantle: LAM-MC-ICPMS analysis of zircon megacrysts in kimberlites. *Geochemica et Cosmochimica Acta* **63**, 133-147 (2000).
- Godfrey, J.D. The deuterium content of hydrous minerals from the east-central Sierra Nevada, and Yosemite National Park, *Geochim. Cosmochim. Acta*, **26**, 1215-1245, (1962).
- Groves, D., Archibald, N., Bettenay, L. *et al.* Greenstone belts as ancient marginal basins or ensialic rift zones. *Nature* **273**, 460–461 (1978).
- Gruner, J.W., The origin of sedimentary iron formations: The Biwabik formation of the mesabi range. *Economic Geology*, **17**, 407-460 (1922).
- Hamilton, P.J., O’Nions, R. K., Evensen, N. M., Bridgwater, D. and Allaart., J. H. Sm-Nd isotopic investigations of Isua supracrustals and implications for mantle evolution, *Nature*. **272**, 41-43, (1978).
- Hamilton, P., Evensen, N., O’Nions, R. *et al.* Sm—Nd systematics of Lewisian gneisses: implications for the origin of granulites. *Nature* **277**, 25–28 (1979).
- Hammerli, J., Kemp, A.I.S., Jeon, H. An Archean Yellowstone? Evidence from extremely low  $\delta^{18}\text{O}$  in zircons preserved in granulites of the Yilgarn Craton, Western Australia. *Geol. Soc. of America* **46**, 411-414 (2018).
- Haughton, P.D.W., Todd, S.P., Morton, A.C. Sedimentary provenance studies. *Geological Society Specia Publication.* **57**, 1-11 (1991).

- Haskin, L. A., Frey, F. A., Schmitt, R. A., Smith, R. H. Meteoritic, solar, and terrestrial rare-earth distributions. *Phys. Chem. Earth*. **7**, 167-321 (1966).
- Harris, C., Pronost, J.J.M., Ashwal, L.D., Cawthorn, R.G. Oxygen and hydrogen isotope stratigraphy of the Rustenburg layered suite, Bushveld complex: constraints on crustal contamination. *J. of Petro.* **46**, 579-601 (2005).
- Harper, C., Jacobsen, S. Evidence from coupled  $^{147}\text{Sm}$ - $^{143}\text{Nd}$  and  $^{146}\text{Sm}$ - $^{142}\text{Nd}$  systematics for very early (4.5-Gyr) differentiation of the Earth's mantle. *Nature* **360**, 728-732 (1992).
- Hawkesworth, C., Cawood, P., Kemp, T., Storey, C., Dhuime, B. A matter of preservation. *Science*, **323**, 49-50 (2009).
- Hawkesworth, C.J. The generation and evolution of the continental crust. *J. Geol. Soc. London*. **167**, 229-248 (2010).
- Hawkesworth, C. J., Dhuime, B., Pietranik, A. B., Cawood, P. A., Kemp, A. I., & Storey, C. D. The generation and evolution of the continental crust. *Journal of the Geological Society*, *167*(2), 229-248 (2010).
- Huang, S., Jacobsen, S., Mukhopadhyay, S.  $^{147}\text{Sm}$ - $^{143}\text{Nd}$  systematics of Earth are inconsistent with superchondritic Sm/Nd ratio. *Proc. Natl. Acad. Sci.* **110**, 4929-4934 (2013).
- Heaton, T.H.E., Sheppard, S.M.F. Hydrogen and oxygen isotope evidence for sea-water hydrothermal alteration and ore deposition, Troodos complex, Cyprus. *Geol. Soc. London Spec. Publ.* **7**, 42-57 (1979).
- Hellstrom, J., Paton, C., Woodhead, J., Hergt, J., Lolite: Software for spatially resolved LA- (QUAD and MC) ICPMS analysis. in "Laser Ablation ICP-MS in the Earth Sciences: Current Practices and Outstanding Issues", P. Sylvester, eds., Mineralogical Association of Canada, Quebec, Mineralogical Association of Canada Short Course Series 40, 343-348 (2008).
- Hess, H. History of ocean basins. Petrologic studies: A volume in honor of AF Buddington. New York: *geological society of America*, 599-620 (1962).
- He, Q. Zhang, S.-B., Zheng, Y.-F. High temperature glacial meltwater-rock reaction in the Neoproterozoic: Evidence from zircon in-situ oxygen isotopes in granitic gneiss from the Sulu orogen. *Precambrian Research*, **284**, 1-13 (2016).
- Hiess, J., Bennett, V., Nutman, A.P., Williams, I.S. Archean fluid assisted crustal cannibalization recorded by low  $\delta^{18}\text{O}$  and negative  $\epsilon\text{Hf}(T)$  isotopic signatures of West Greenland granite zircon. *Contributions to Mineralogy and Petrology*, **161**, 1027-1050 (2011).
- Hiess, J., Bennett, V.C., Nutman, A.P., and Williams, I.S., In situ U-Pb, O and Hf isotopic compositions of zircon and olivine from Eoarchean rocks, West Greenland: New insights to making old crust. *Geochimica et Cosmochimica Acta*, **73**, 4489-4516 (2009).

- Hofmann, A., Jodder, J. Xie, H. The Archean geological history of the Singhbhum Craton, India, --a proposal for a consistent framework of craton evolution. *Earth-Science Reviews*, **228**, 103994 (2022).
- Holman, C., Muehlenbachs, K. The  $^{18}\text{O}/^{16}\text{O}$  ratio of 2-billion-year-old seawater inferred from ancient oceanic crust. *Science*. **259**, 1733-1736 (1993).
- Holland, H. D. Why the atmosphere became oxygenated: A proposal. *Geochim. Cosmochim. Acta* **73**, 5241–5255 (2009).
- Hoffman, S.E., Wilson, M., Stakes, D.S. Inferred oxygen isotope profile of Archean oceanic crust, Onverwacht Group, South Africa. **321**, 55-58 (1986).
- Holland, H. D. The Chemistry of the Atmosphere and Oceans. *Wiley-Interscience, New York*. **1** (1978).
- Holland, H.D. The oceans: a possible source of iron-formations. *Econ. Geol.* **68**, 1169-1172 (1973).
- Holder, R.M., Viete, D.R., Brown, M., Johnson, T.E. Metamorphism and the evolution of plate tectonics. *Nature* **572**, 378-381 (2019).
- Hollis, J.A., Van Kranendonk, M.J. Cross, A.J., Kirkland, C.L., Armstrong, R.A., Allen, C.M. Low  $\delta^{18}\text{O}$  zircon grains in the Neoproterozoic Rum Jungle Complex, northern Australia: An indicator of emergent continental crust. *Geol. Soc. of America* **6**, 17-25 (2014).
- Hohl, S.V., Viehmann, S. Stromatolites as geochemical archives to reconstruct microbial habits through deep time: Potential and pitfalls of novel radiogenic and stable isotope systems. *Earth-Science Reviews*, **218**, 103683 (2021).
- Hren, M.T., Tice, M.M., Chamberlain, C.P., Oxygen and hydrogen isotope evidence for a temperature climate 3.42 billion years ago. *Nature*. **462**, 131-185 (2009).
- Ireland T. R. & Williams I. S. Considerations in zircon geochronology by SIMS. In: Hanchar J. M. & Hoskin P. W. O. eds. *Zircon, Reviews in Mineralogy and Geochemistry* **53**, 215–241 (2003).
- Jacobsen, S. B., & Wasserburg, G. J. Sm-Nd isotopic evolution of chondrites. *Earth and Planetary Science Letters*, **50**, 139-155 (1980).
- Jacobsen, S.B., Wasserburg, G.J., Sm-Nd isotopic evolution of chondrites. *Earth Planet. Sci. Lett.* **50**, 139-155 (1984).
- Jacobsen, S., Quick, J.E., Wasserburg, G.J. A Nd and Sr isotopic study of the Trinity peridotite; implications for mantle evolution. *Earth Planet. Sci. Lett.* **68**, 361-378 (1984).
- Jacobsen, S., Dymek, R., Nd and Sr isotope systematics of clastic metasediments from Isua, West Greenland: Identification of pre-3.8 Ga differentiated crustal components. *Journal of Geophysical Research*. **93**, 338-354 (1988).

- Jacobsen, S.B., Pimentel-Klose, M.R. Nd isotopic variations in Precambrian banded iron formations. *Geophys. Res. Lett.* **15**, 393-396 (1988).
- Jacobsen, S. B., Pimentel-Klose., M. R., A Nd isotopic study of the Hamersley and Michipicoten banded iron formations: the source of REE and Fe in the Archean oceans. *Earth Planet. Sci. Lett.* **87**, 29-44 (1988).
- Jaffrés, J. B., Shields, G. A., Wallmann, K. The oxygen isotope evolution of seawater: A critical review of a long-standing controversy and an improved geological water cycle model for the past 3.4 billion years. *Earth Sci. Rev.* **83**, 83–122 (2007).
- Jodder, J., Hofmann, A., Ueckermann, H. 3.51 Ga old felsic volcanic rocks and carbonaceous cherts from the Gorumahisani Greenstone Belt-Insights into the Paleoproterozoic record of the Singhbhum Craton, India. *Precamb. Res.* **357**, 106109 (2021).
- Johnson, T., Brown, M., Gardiner, N. *et al.* Earth's first stable continents did not form by subduction. *Nature* **543**, 239–242 (2017).
- Johnson, T., Brown, M., Kaus, B. *et al.* Delamination and recycling of Archean crust caused by gravitational instabilities. *Nature Geosci.* **7**, 47–52 (2014).
- Johnson, C.M., Beard, B.L. Fe isotopes: An emerging technique for understanding modern and ancient biogeochemical cycles. *GSA Today*, **16**, [10.1130/GSAT01611A.1](https://doi.org/10.1130/GSAT01611A.1) (2006).
- Johnson, C.M., Beard, B.L., Beukes, N.J., Klein, C., O'Leary, J.M., Ancient geochemical cycling in the Earth as inferred from Fe isotope studies of banded iron formations from the Transvaal Craton. *Contrib. Mineral. Petrol.* **144**, 523-547 (2003).
- Johnson, C.M., Beard, B.L., Klein, C., Beukes, N.J., Roden, E.E., Iron isotopes constrain biologic and abiologic processes in banded iron formation genesis. *Geochimica et Cosmochimica Acta*, **72**, 151-169 (2008).
- Jones, C.E., Halliday, A.N., Rea, D.K., Owen, R.M., Neodymium isotopic variations in North Pacific modern silicate sediment and the insignificance of detrital REE contributions to seawater: *Earth Planet. Sci. Lett.* **127**, 55-66 (1994).
- Jones, H. C., The iron ore deposit of Bihar and Orissa. *Geol. Surv. India Mem.*, (2), 167-302. (1934).
- Kato., Y., Yamaguchi., K. E., Ohmoto., H. Rare earth elements in Precambrian banded iron formations: Secular changes of Ce and Eu anomalies and evolution of atmosphere oxygen. *Geol. Soc. America. Memoir.*, **198**, 269-289 (2006).
- Kasting, J. F., Howard, M. T., Wallmann, K., Veizer, J., Shields, G., Jaffrés, J. Paleoclimates, ocean depth, and the oxygen isotopic composition of seawater. *Earth Planet. Sci. Lett.* **252**, 82–93 (2006).
- Karhu, J., Epstein, S. The implication of the oxygen isotope records in coexisting cherts and phosphates. *Geochim. Cosmochim. Acta* **50**, 1745–1756 (1986).

- Kelemen, P., Hanghøj, K., Greene, A. One View of the Geochemistry of Subduction-Related Magmatic Arcs, with an Emphasis on Primitive Andesite and Lower Crust. *Treati. Geochem.* **3**, 593-659 (2003).
- King, E. M., Valley, J. W., Davis, D. W., & Edwards, G. R. Oxygen isotope ratios of Archean plutonic zircons from granite–greenstone belts of the Superior Province: indicator of magmatic source. *Precambrian Research*, **92**, 365-387 (1998).
- Kirkland, C.L., Hartnady, M.I.H., Barham, M. *et al.* Widespread reworking of Hadean-to-Eoarchean continents during Earth’s thermal peak. *Nat Commun* **12**, 331 (2021).
- Klein, C., Some Precambrian banded iron-formations (BIFs) from around the world: Their age, geologic setting, mineralogy, metamorphism, geochemistry, and origins. *American Mineralogist* **90**, 1473–1499 (2005).
- Kleine, B. I., Stefansson, A., Halldórsson, S. A., Whitehouse, M. J., & Jónasson, K. Silicon and oxygen isotopes unravel quartz formation processes in the Icelandic crust. *Geochemical Perspectives Letters*, **7**, 5-11 (2018).
- Knauth, L. P., Epstein, S. Hydrogen and oxygen isotope ratios in nodular and bedded cherts. *Geochim. Cosmochim. Acta* **40**, 1095–1108 (1976).
- Knauth, L. P., Lowe, D. R. High Archean climatic temperature inferred from oxygen isotope geochemistry of cherts in the 3.5 Ga Swaziland Supergroup, South Africa. *Geol. Soc. Am. Bull.* **115**, 566–580 (2003).
- Knauth, L. P. Temperature and salinity history of the Precambrian ocean: Implications for the course of microbial evolution. *Palaeogeog. Palaeoclimat. Palaeoecol.* **219**, 53–69 (2005).
- Kyser, T.K., O’Neil, J.R. Hydrogen isotope systematics of submarine basalts. *Geochim. Cosmochim. Acta.* **48**, 2123-2133 (1984).
- Knauth, L. P. Temperature and salinity history of the Precambrian ocean: Implications for the course of microbial evolution. *Palaeogeog. Palaeoclimat. Palaeoecol.* **219**, 53–69 (2005).
- Krapez, B., Barely, M.E., Pickard, A.L. Hydrothermal and resedimented origins of the precursor sediments to banded iron formation: sedimentological evidence from the Early Paleoproterozoic Brockman Supersequence of Western Australia. *Sedimentology.* **50**, 979-1011 (2003).
- Kundu, A. & Matin, A. Sedimentary and tectonic environment of deposition of the Archean Birtola Formation of Singhbhum Orissa craton, Sundergarh District, Orissa. *Indian Journal of Geology*, **79**, 22-34 (2007).
- Kurzweil, F., Willie, M., Schoenberg, R., Taubald, H., Van Kranendonk., M.J. Continuously increasing  $\delta^{98}\text{Mo}$  values in Neoproterozoic black shales and iron formations from the Hamersley basin. *Geochimica et Cosmochimica Acta* **164**, 523-542 (2015).

- Kusky, T.M., Li, J.H., Tucker, R.D. The Archean Dongwanzi ophiolite complex, North China Craton: 2.505-billion-year-old oceanic crust and mantle. *Science*. **292**, 1142-1145 (2001).
- Kusky, T., Windley, B., Polat, A., Wang, L., Ning, W., Zhong, Y. Archean dome-and-basin style structures form during growth and death of intraoceanic and continental margin arcs in accretionary orogens. *Earth-Science Reviews*, **220**, 103725 (2021).
- Lapen, T.J., Richter, M., Andreasen, R., Irving, A.J., Satkoski, A.M., Beard, B.L., Nishi-izumi, K., Jull, A.J.T., Caffee, M.W. Two billion years of magmatism recorded from a single Mars meteorite ejection site. *Science. Advances*. **3**. (2017).
- Land, L.S., Lynch, F.L. The  $\delta^{18}\text{O}$  of mudrocks: More evidence for an  $^{18}\text{O}$ -buffered ocean. *Geochim. Cosmochim. Acta*. **60**, 3347-3352 (1996).
- Lantink, M. L., Davies, J. H., Ovtcharova, M., & Hilgen, F. J. Milankovitch cycles in banded iron formations constrain the Earth–Moon system 2.46 billion years ago. *Proceedings of the National Academy of Sciences*, *119*(40), e2117146119 (2022).
- Large, R.R., Mukherjee, I., Gregory, D., Steadman, J., Corkrey, R., Danyushevsky, L.V., Atmosphere oxygen cycling through the Proterozoic and phanerozoic. *Mineral. Deposita* **317**, 1–23 (2019).
- Lecuyer, C., Fourcade, S. Oxygen isotope evidence for multi-stage hydrothermal alteration at a fossil slow-spreading center: the Silurian Trinity ophiolite (California, U.S.A). *Chem. Geol.* **87**, 231-246 (1991).
- Lepp, H. and Goldrich, S.S., Origin of Precambrian iron-formation *Economic Geology*, **59**, 1025-1060 (1964).
- Le Bas M.J., Le Maitre R.W., Streickeisen A. and Zanettin B. A chemical classification of volcanic rocks based on the total Alkali-Silica diagram *J. Petrol.* *27*, 745-750 (1986).
- Li, W., Beard, B., Johnson, C. Biologically recycled continental iron is a major component in banded iron formations. *Proceedings of the national academy of sciences*, **112**, 8193-8198 (2015).
- Lin, S., Parks, J., Heaman, L., Simonetti, A., Corkery, M., Diapirism and sagduction as a mechanism for deposition of ‘Timiskaming-type’ sedimentary sequences, Superior Province: evidence from detrital zircon geochronology and implications for the Borden Lake conglomerate exposed middle to lower crust in the Kapuskasing Uplift. *Precambrian Research*. **238**, 148–157 (2013).
- Liakhovitch, V., Quick, J.E., Gregory, RT. Hydrogen and oxygen isotope constraints on hydrothermal alteration of the Trinity peridotite, Klamath, Mountains, California. *Inter. Geo. Rev.* **47**, 203-214 (2005).

- Locht, S., Hoffman, J., Rosing, M., Sprung, P., Munker, C. Preservation of Eoarchean mantle processes in 3.8 Ga peridotite enclaves in the Itsaq Gneiss Complex, Southwest Greenland. *Geochimica Cosmochimica Acta*, **280**, 1-25 (2020).
- Ludwig K.R. SQUID 1.02, A user's manual. *Berkeley Geochronological Center Special. 2* (2001).
- Lynch, F.L., Land, L.S. Diagenesis of calcite cement in Frio formation sandstones and its relationship to formation water chemistry. *J. Sedimentary Research.* **66**, 439-446 (1996).
- Lugmair, G.W., Marti, K., Lunar initial  $^{143}\text{Nd}/^{144}\text{Nd}$ : Differential evolution of the lunar crust and mantle. *Earth Planet. Sci. Lett.* **39**, 349-357 (1978).
- Ludwig, K.R. SQUID 1.00, A user's manual. Berkeley Geochronology Center Special Publications, **2**, (2000).
- Mahapatro, S. N., Pant, N., Bhowmik, S. K., Nanda, J. Archean granulite facies metamorphism at the Singhbhum Craton-Eastern Ghats Mobile Belt Interface: Implication for the Ur Supercontinent assembly. *Geol J.* **47**, 312-333 (2012).
- Mahalik, N. K. Geology of rocks lying between Gangpur Group and Iron Ore Group of the Horse-Shoe Syncline in North Orissa. *Indian Journal of Earth Sciences*, **14**, 73-83 (1987).
- Maisch, M., Wu, W., Kappler, A., Swanner, E. Laboratory simulation of iron (II)-rich Precambrian Marine upwelling system to explore the growth of photosynthetic bacteria. *Journal of visualized experiments* (113), e54251, doi: 10.3791/54251 (2016).
- Manikyamba, C., Kerrich, R. Geochemistry of black shales from the Neoproterozoic Sandar superterrane, India: First Cycle volcanogenic sedimentary rocks in an intraoceanic arc-trench complex. *Geochimica et Cosmochimica Acta* **70**, 4663-4679 (2006).
- Maltese, A., Caro, G., Pandey, O.P. *et al.* Direct evidence for crust-mantle differentiation in the late Hadean. *Commun Earth Environ* **3**, 12 (2022).
- MacRae, N.D., Nesbitt, H.W., Kronberg., B.I. Development of a positive Eu anomaly during diagenesis. *Earth Planet. Sci. Lett*, **109**, 585-591 (1992).
- Macfarlane, A.W., Danielson, A., Holland, H.D. Geology and major and trace element chemistry of late Archean weathering profiles in the Fortescue Group, Western Australia: Implications for atmospheric  $\text{Po}_2$ . *Precambrian Research.* **65**, 297-317 (1994).
- MacGregor, I.G., Manton, S.R. Robert's victor eclogites: ancient oceanic crust. *J. Geophys. Res.* **91**, 14063-14079 (1986).
- Matsuhisa, Y., Goldsmith, J.R., Clayton, R.N. Oxygen isotope fractionation in the systems quartz-albite-anorthite-water. *Geochimica et Cosmochimica Acta* **43**, 1131-1140 (1979).
- Matthews, A., Katz, A. Oxygen isotope fractionation during dolomitization of calcium carbonate. *Geochimica et Cosmochimica Acta* **41**, 1431-1438 (1977).

- Mattey, D., Lowry, D. & Macpherson, C. Oxygen isotope composition of mantle peridotite. *Earth Planet. Sci. Lett.* **128**, 231-241 (1994).
- Mandal, P. Passive source seismic imaging of the crust and upper mantle underlying the Archean Singhbhum Craton, Eastern India. *J. Asian. Earth. Sciences*, **146**, 300-314 (2019).
- Mahapatro, S. N., Pant, N., Bhowmik, S. K., Nanda, J. Archean granulite facies metamorphism at the Singhbhum Craton-Eastern Ghats Mobile Belt Interface: Implication for the Ur Supercontinent assembly. *Geol J.* **47**, 312-333 (2012).
- Martinell, L.A., Victoria, R.L., Dematte, J.I., Richey, J.E., Devol, A.H. Chemical and mineralogical composition of Amazon River floodplain sediments, Brazil. *Applied Geochemistry*. **8**, 394-402 (1993).
- Mazumder, R., Van Loon, A. J., Mallik, L., Reddy, S. M., Arima, M., Altermann, W., Eriksson, P. G. and De, S. Mesoarchean– Palaeoproterozoic stratigraphic record of the Singhbhum crustal province, eastern India: a synthesis. In, Mazumder, R. and Saha, D. (Eds.), *Palaeoproterozoic of India, Geological Society, London, Special Publications*, **365**, 31–49 (2012).
- Mazumder, R., Chaudhuri., T. Paleoarchean terrestrial to shallow marine sedimentation on Singhbhum Craton, eastern India (the Western Iron Ore Group). *Precambrian Research* **354**, 106071 (2021).
- McCulloch, M. T., Wasserburg, G. J. Sm-Nd and Rb-Sr chronology of continental crust formation. *Science* **200**, 1003-1011 (1978).
- McCrea, J.M. On the oxygen isotope geochemistry of carbonates and a paleotemperature scale. *J. Chem. Phys.*, **18**, 849-857 (1950).
- McCulloch, M. T., Gregory, R.T., Wasserburg, G. J., Taylor, H. P. Sm-Nd, Rb-Sr,  $^{18}\text{O}/^{16}\text{O}$  isotopic systematics in an oceanic crustal section: evidence from the Semail ophiolite. *J. Geophys. Res.* **86**, 2721-2735 (1981).
- McCulloch, M. T., & Black, L. P. SmNd isotopic systematics of Enderby Land granulites and evidence for the redistribution of Sm and Nd during metamorphism. *Earth and Planetary Science Letters*, **71**, 46-58 (1984).
- McCulloch, M.T., Gamble, J.A. Geochemical and Geodynamical constraints on subduction zone magmatism. *Earth Planet. Sci. Lett.* **102**, 358-374 (1991).
- McDonough, W. F., Sun, S. S., Ringwood, A. E., Jagoutz, E. A., Hofmann, W. Potassium, rubidium and cesium in the Earth and Moon and the evolution of the mantle of the Earth. *Geochim. Cosmochim. Acta*, **56** 1001-1012 (1992). McLellan, J.G., Oliver, N.H., & Schaubs, P.M. Fluid flow in extensional environments; numerical modeling with an application to Hamersley iron ores. *J. Struct. Geol.* **26**, 1157-1171 (2004).

- McDonough, W. F., Sun, S. S., Ringwood, A. E., Jagoutz, E., Hofmann, A. W., Potassium, rubidium and cesium in the Earth and Moon and the evolution of the mantle of the Earth. *Geochim. Cosmochim. Acta*, **56** 1001-1012 (1992).
- McDonough, W. F., Sun, S. S., The composition of the Earth, *Chemical Geology. Chem. Geol.*, **120**, 223-253 (1995).
- McLennan, S.M., Taylor, S.R. and Kroner, A. Geochemical Evolution of Archean Shales from South Africa, I, the Swaziland and Pogola Supergroups. *Precambrian Research*, **22**, 93-124 (1983).
- McLennan, S.M., Taylor, S.R. Eriksson, K.A. Geochemistry of Archean shales from the Pilbara Supergroup, Western Australia. *Geochimica et Cosmochimica Acta*. **47**, 1211-1222 (1983).
- McLennan, S., Taylor, S. Continental freeboard, sedimentation rates and growth of continental crust. *Nature* **306**, 169–172 (1983).
- Michard, A., Gurriet, P., Soudant, M., & Albarede, F. Nd isotopes in French Phanerozoic shales: external vs. internal aspects of crustal evolution. *Geochimica et Cosmochimica Acta*, **49**, 601-610 (1985).
- Miller, S.L., Urey, H.C., Or'O, J. Origin of organic compounds on the primitive earth and in meteorites. *J. Mol. Evol.* **9**, 59-72 (1976).
- Miller, J.A., Cartwright, I., Buick, I.S., Barnicoat, A.C. An O-isotope profile through the HP–LT Corsican ophiolite, France and its implications for fluid flow during subduction. *Chemical Geology*, **178**, 43-69 (2001).
- Mojzsis, S.J., Harrison, T.M., Pidgeon, R.T. Oxygen-isotope evidence from ancient zircons for liquid water at the Earth's surface 4,300 Myr ago. *Nature*, **409**, 178-181 (2001).
- Muehlenbachs, K., Clayton, R. N. Oxygen isotope composition of the oceanic crust and its bearing on seawater, *J. Geo. Phys. Res.* **81**, 4365-4369 (1976).
- Miller, R., O'Nions, R. Source of Precambrian chemical and clastic sediments. *Nature* **314**, 325–330 (1985).
- Mishra, S., Deomurari, M. P., Wiedenbeck, M., Goswami, J. N., Ray, S. & Saha, A. K.  $^{207}\text{Pb}/^{206}\text{Pb}$  zircon ages and the evolution of the Singhbhum Craton, eastern India: an ion microprobe study. *Precamb. Res.*, **93**, 139–151 (1999).
- Mitra, A., Dey, S., Zong, K., Liu, Y. and Mitra, A. Building the core of a Paleoarchean continent: Evidence from granitoids of Singhbhum Craton, eastern India. *Precambrian Research*, 335,105436 (2019).
- Moorbath, S., Taylor, P.N., Jones, N.W. Dating the oldest terrestrial rocks...facts or fiction, *Chem. Geol.* **57** 63-86 (1986).

- Morris, R., Horwitz, R., The origin of the iron-formation rich Hamersley Group of Western Australia—deposition on a platform. *Precambrian Research*, **21**, 273-197 (1983).
- Mukhopadhyay, D. Precambrian of Eastern Indian Shield—perspective and problems. *Mem. Geol. Soc. India* **8**, 1-12 (1988).
- Mukhopadhyay, D. Precambrian stratigraphy of Singhbhum— the problems and a prospect. *Indian Journal of Earth Sciences*, **3**, 208-219 (1976).
- Mukhopadhyay, J., Ghosh, G., Beukes, N., and Gutzmer, J. Precambrian colluvial iron ores in the Singhbhum Craton: implications for origin, age of BIF-hosted high-grade iron ores and stratigraphy of the Iron Ore Group. *Journal of the Geological Society of India*, **70**, 34 (2007).
- Mukhopadhyay, J., Crowley, Ghosh, G., Ghosh, S., Chakrabarti, K., Misra B. and Bose, S. A Mesoarchean Paleosol from eastern India – the second oldest paleosol on earth. *Mineralogical Magazine*, **77**, 1802 (2013).
- Mukhopadhyay, J., Crowley, Q.G., Ghosh, S., Ghosh, G., Chakrabarti, K., Misra, B., Heron, K., and Bose, S., Oxygenation of the Archean atmosphere: New paleosol constraints from eastern India. *Geology*, **42**, 923-926 (2014).
- Mukhopadhyay, J., Mishra, B., Chakrabarti, K., De, S., and Ghosh, G., Uraniferous paleoplacers of the Mesoarchean Mahagiri Quartzite, Singhbhum craton, India: Depositional controls, nature and source of > 3.0 Ga detrital uraninites. *Ore Geology Reviews*, **72**, 1290-1306 (2016).
- Murthy, V.N., and Acharya, S. Lithostratigraphy of the Precambrian rocks around Koira, Sundergarh district, Orissa. *Journal of the Geological Society of India*, **16**, 55-68 (1975).
- Murthy, V.R., Patterson, C., Primary isochron of zero age for meteorites and the earth. *J. Geophys. Res.* **67**, 1161–1167 (1962).
- Miller, S.R., Mueller, V, Meert, J. G., Kamenov, G. D., Pivarunas, A. F., Sinha, A. K., Pandit, M. K. Detrital Zircons Reveal Evidence of Hadean Crust in the Singhbhum Craton, India. *J. Geol.* **126**, 541-552 (2018).
- Mukhopadhyay, J., Beukes, N.J., Armstrong, R.A., Zimmermann, U., Ghosh, G., Medda, R.A. Dating the oldest greenstone in India: A 3.51-Ga precise U-Pb SHRIMP zircon age for dacitic lava of the Southern Iron Ore Group. *Journal of Geology*, **116**, 449-461 (2008).
- Mukhopadhyay, D., Matin, A. The Architecture and Evolution of the Singhbhum Craton. *Episodes*, **43**, 19-50 (2020).
- Myers, J.S., Watkins, K.P. Origin of granite-greenstone patterns, Yilgarn Block, Western Australia. *Geological Survey of Western Australia*, **13**, 778-780 (1985).

- Nelson, D.R., Bhattacharya, H.N., Thern, E.R., Altermann, W. Geochemical and ion-microprobe U–Pb zircon constraints on the Archaean evolution of Singhbhum Craton, eastern India. *Precambrian Research*, **255**, 412-432 (2014).
- Nelson, D.R., Trendall, A.F., de Laeter, J.R., Grobler, N.J., Fletcher, I.R. A comparative study of the geochemical and isotopic systematics of late Archean flood basalts from the Pilbara and Kaapvaal Cratons. *Precambrian Research*, **54**, 231-256 (1992).
- Nwaila, G., Frimmel, H., Minter, W. Provenance and Geochemical Variations in Shales of the Mesoarchean Witwatersrand Supergroup. *The Journal of Geology*. **125**, 399-422 (2017).
- Nutman, A.P., Mojzsis, S.J., Friend, C.R.L., Recognition of  $\geq 3850$  Ma water-lain sediments in West Greenland and their significance for the early Archaean Earth. *Geochemica et Cosmochica Acta*, **61**, 2475-2484 (1997).
- Olierook, H., Clark, C., Reddy, S., Mazumder, R., Jourdan, F., Noreen, E. Evolution of the Singhbhum Craton and supracrustal provinces from age, isotopic and chemical constraints. *Earth Sci. Rev.* **193**, 237-259 (2019).
- Olivarez, A.M., Owen, R.M. The europium anomaly of seawater: implications for fluvial versus hydrothermal REE inputs into the ocean. *Chemical Geology*, **92**, 317-328 (1991).
- O’Neil, J., Carlson, Building Archean cratons from Hadean mafic crust. *Science*, **355**, 1199-1202 (2017).
- O’Neil, J.R., and Chappell, B.W., Oxygen and hydrogen isotope relations in the Berridale Batholith: *Journal of the Geological Society*, **133**, 559-571, doi:10.1144/gsjgs.133.6.0559 (1977).
- Pandey, O. M., Mezger, K., Ranjan, S. et al. Genesis of the Singhbhum Craton, eastern India; implications for Archean crust-mantle evolution of the Earth. *Chemical Geology*. **512**, 85-106 (2019).
- Paces, J. B., Miller, J. D. Precise U-Pb ages of Duluth Complex and related mafic intrusions, northwestern Minnesota: Geochronological insights to physical, petrogenetic, paleomagnetic, and tectomagnetic process associated with the 1.1 Ga Midcontinent Rift System. *J. Geophy. Res.* **98**, 13997-14013 (1993).
- Pascoe, E. H., A manual of the geology of India and Burma. *Govt. of India Press, Calcutta*, **1**:483 (1950).
- Patterson, C., Brown, H., Tilton, G., & Inghram, M. Concentration of uranium and lead and the isotopic composition of lead in meteoritic material. *Physical Review*, **92**, 1234 (1953).
- Patterson, C. Age of meteorites and the earth. *Geochemica et Cosmochica Acta*, **10**, 230- 237 (1956).

- Paton, C., Woodhead, J.D., Hellstrom, J.C., Hergt, J.M., Greig, A., Maas, R., Improved laser ablation U-Pb zircon geochronology through robust downhole fractionation correction. *Geochemistry, Geophysics and Geosystem* **11**, Q0AA06 (2010).
- Paton, C., Hellstrom, J., Paul, B., Woodhead, J., Hergt, J., Iolite: Freeware for the visualisation and processing of mass spectrometric data. *Journal of Analytical Atomic Spectrometry*, DOI: 10.1039/c1ja10172b (2011).
- Peck, W. H., Valley, J. W., & Graham, C. M. Slow oxygen diffusion rates in igneous zircons from metamorphic rocks. *American Mineralogist*, **88**, 1003-1014 (2003).
- Perry Jr., E. C. The oxygen isotope chemistry of ancient cherts. *Earth Planet. Sci. Lett.* **3**, 62–66 (1967).
- Peucat, J. J., Jegouzo, P., Vidal, P., & Bernard-Griffiths, J. Continental crust formation seen through the Sr and Nd isotope systematics of S-type granites in the Hercynian belt of western France. *Earth and Planetary Science Letters*, **88**, 60-68 (1988).
- Piepgras, D. J., Wasserburg, G. J., Dasch, E. J. The isotopic composition of Nd in different ocean masses. *Earth Planet. Sci. Lett.* **45**, 223-236 (1979).
- Pin., C., Gannoun., A. Dupont, A., Rapid, Simultaneous separation of Sr, Pb, and Nd by extraction chromatography prior to isotope ratios determination by TIMS and MC-ICP-MS, *Journal of Analytical Atomic Spectrometry*, **29**, 1-30 (2014).
- Prasad, J., Venkatesh, A.S., Sahoo, P.R., A submarine hydrothermal origin of banded iron formations from Archean Kiriburu-Meghahatuburu iron ore deposit, Singhbhum Craton, eastern India. *Ore Geology Reviews*. **105**, 105125 (2022).
- Pearce, J.A., Geochemical fingerprinting of oceanic basalts with applications to ophiolite classification and the search for Archean Ocean floor. *Lithos* **100**, 14-48 (2008).
- Philpotts, A. R., & Ague, J. J. *Principles of igneous and metamorphic petrology*. Cambridge University Press (2009).
- Pin, C., Gannoun, A., Dupont, A. Rapid, Simultaneous separation of Sr, Pb, and Nd by extraction chromatography prior to isotope ratios determination by TIMS and MC-ICP-MS, *Journal of Analytical Atomic Spectrometry*, **29**, 1-30 (2014).
- Pope, E., Bird, D.K., Rosing, M.T. Isotope composition and volume of Earth's early oceans, *Proceeding of the National Academy of Science*, **109**, 4371-4375 (2012)
- Pope, E.C., Bird, D.K., Arnorsson, S., Evolution of low-<sup>18</sup>O Icelandic crust. *Earth Planet. Sci. Lett.* **374**, 47-59 (2013).
- Quick, J.E., Gregory, R.T. Significance of melt-wall rock reaction: A comparative anatomy of three ophiolites. *The Journal of Geology*. **103**, 187-198 (1995).

- Ranjan, S., Upadhyay, D., Pruseth, K.L., Nanda, J.K. Detrital zircon evidence for change in geodynamic regime of continental crust formation 3.7-3.6 billion years ago. *Earth Planet. Sci. Lett.* **538**, 116206 (2020).
- Rai, K. L., Sarkar, S. N., and Paul, P. R., Primary depositional and diagenetic features in the banded iron formation and 364 associated iron ore deposits of Noamundai, Singhbhum districts, Bihar, India. *Mineral. Deposita*, **15**: 189-200 (1980).
- Richter, F. M. A major change in the thermal state of the Earth at the Archean-Proterozoic boundary: consequences for the nature and preservation of continental lithosphere. *Journal of Petrology*, **1**, 39-52 (1998).
- Robbins, L.J., Funk, S.P., Flynn, S.L. *et al.* Hydrogeological constraints on the formation of Palaeoproterozoic banded iron formations. *Nat. Geosci.* **12**, 558–563 (2019).
- Roberts, N.M.W., Spencer, C.J. The zircon archive of continent formation through time. *Geol. Soc. London*, **389**, 197-225 (2015).
- Rollinson, H.R. (1993). *Using Geochemical Data: Evaluation, Presentation, Interpretation* (1st ed.). Routledge. <https://doi.org/10.4324/9781315845548>
- Ronov, A.B. & Migdisov, A.A. Geochemical history of the crystalline basement and sedimentary cover of the Russian and North American Platforms. *Sedimentology*, **16**, 137-185 (1971).
- Rouxel O. J., Dobbek N., Ludden J. and Fouquet Y. Iron isotope fractionation during oceanic crust alteration. *Chem. Geol.* **202**, 155–182 (2003).
- Rosenbaum, J., Sheppard, S.M.F. An isotopic study of siderites, dolomites and ankerites at high temperatures. *Geochim. Cosmochim. Acta.*, **50**, 1147-1150 (1986).
- Rubey, W.W. Development of the hydrosphere and atmosphere, with special reference to probable composition of the early atmosphere. *Geol. Soc. America*, **62**, 631-650 (1955).
- Rumble, D., Giorgis, D., Ireland, T. Zhang, Z., Xu, H., Yui, T.F., Yang, J., Xu, Z., Liou, J.G. Low  $\delta^{18}\text{O}$  zircons U-Pb dating and the age of the Qinglongshan oxygen and hydrogen isotope anomaly near Donghai in Jiangsu Province, China. *Geochim. Cosmochim. Acta.* **66**, 2299-2306 (2002).
- Rutherford, Ernest. *Radioactive transformations*. Vol. **3**. New York: C. Scribner's Sons (1906).
- Saha, A., Basu, A.R., Garziona, C.N., Bandyopadhyay, P.K., Chakrabarti, A. Geochemical and petrological evidence for subduction-accretion processes in the Archean. *Earth and Planetary Science Letters*, **220**, 91-106 (2004).
- Sameer, R. Upadhyay, D., Srikantappa., C. Eoarchean to Neoproterozoic crustal evolution of the Western Dharwar Craton, Southern India: Clues from U-Pb-Hf isotope composition of detrital zircon. *Precamb. Res.* **371**, 106559 (2022).

- Sánchez-Lorda, M. E., García de, M., Pin, S., Gil, C., Ibarra, J. I. Concomitant measurement of  $^{143}\text{Nd}/^{144}\text{Nd}$  and  $^{147}\text{Sm}/^{144}\text{Nd}$  ratios without isotope dilution in geological samples: An assessment of MC-ICP-MS capabilities, *Int. J. Mass Spect.* **333**, 34-43 (2013).
- Sarkar, S. C. Geology and Ore Mineralisation of the Singhbhum Copper-Uranium Belt, Eastern India. Jadavpur University, Calcutta, 235-263 (1984).
- Sarkar, S.C. Crustal evolution and metallogeny in the eastern Indian craton: *Geology Survey of India Special Publication*. **55**, 169-194 (2000).
- Sagan, C., Mullen, G. Earth and Mars of atmospheres and surface temperatures. *Science* **177**, 52-56 (1972).
- Sagan, C., Chyba, C. The early faint Sun paradox: Organic shielding of ultraviolet-labile greenhouse gases. *Science* **276**, 1217–1221 (1997).
- Saha, A.K. Crustal evolution of Singhbhum-North-Odisha, Eastern India. *Geol Soc. Ind Mem.* **27**, 341, (1994).
- Scherer, E., Munker, C., & Mezger, K. Calibration of the lutetium-hafnium clock. *Science*, *293*(5530), 683-687 (2001).
- Sengupta, S., Paul, D. K., De Laeter, J. R., Smeth, J. B. Mid-Archean evolution of the Eastern Indian craton: geochemical and isotopic evidence from Bonai pluton. *Precambrian Research*, **49**, 23-37 (1991).
- Smith, H.S., O’Neil, J.R., Erlank, A.J. Oxygen isotope compositions of minerals and rocks and chemical alteration patterns in pillow lavas from the Barberton greenstone belt, South Africa, Archean Geochemistry: The origin and of the Archean continental crust (Kroner, A, Hanson, G.N. and Goodwin, A.M, eds). 115-137 (1984).
- Slama, J., Kosler, J., Condon, D.J., Crowley, J.L., Gerdes, A., Hanchar, J.M., Horstwood, M.S.A., Morris, G.A., Nasdala, L., Norberg, N., Schaltegger, U., Schoene, B., Tubrett, M.N., Whitehouse, M.J. Plesovice zircon: a new natural reference material for U–Pb and Hf isotopic microanalysis. *Chem. Geol.*, **249**, 1–35 (2008).
- Sleep, N. H., Hessler, A. M. Weathering of quartz as an Archean climatic indicator. *Earth Planet. Sci. Lett.* **241**, 594–602 (2006).
- Suzuoki, T., Epstein, S. Hydrogen isotope fractionation between OH-bearing minerals and water. *Geochimica et Cosmochimica Acta*, **40**, 1229-1240 (1976).
- Schad *et al.* Microbial Fe cycling in a simulated Precambrian ocean environment: Implications for secondary mineral (trans)formation and deposition during BIF genesis. *Geochimica et Cosmochimica Acta* **331**, 165-191 (2022).
- Schaefer, Bruce F. *Radiogenic isotope geochemistry: A guide for industry professionals.* Cambridge University Press, 2016.

- Schoenberg, R., Von Blanckenburg, F. An assessment of the accuracy of stable Fe isotope ratio measurements on samples with organic and inorganic matrices by high-resolution multi-collector ICP-MS. *Int. J. Mass. Spectrom.* **242**, 257-275 (2005).
- Sharp, Z. Principles of stable isotope geochemistry (2017).
- Sharma, M., Basu, A.R., Ray, S.L., Sm-Nd Isotopic and Geochemical Study of the Archean Tonalite-Amphibolite association from the eastern Indian Craton. *Contrib. Mineral. Petrol.* **117**, 45-55 (1994).
- Sharma, S.D., Patil, D.J., Srinivasan, R., Gopalan, K. Very high  $^{18}\text{O}$  enrichment in Archean cherts from South India: implications for Archean Ocean temperature. *Terra Nova*, **6**, 385-390 (1994).
- Sholkovitz, E. R. The geochemistry of rare earth elements in the Amazon River estuary. *Geochim Cosmochim Acta* **57**, 2181-2190 (1993).
- Shuckla, Y., Sharma, M., Ansari, A., Kumar, S. Stromatolitic structures from the Mesoarchean Iron Ore Group, Kasia Mine Area, Singhbhum Craton, India. *Journal of the Paleontological Society of India*, **65**, 162-177 (2020).
- Stakes, D.S., O'Neil, J.R., Mineralogy and stable isotope geochemistry of hydrothermally altered oceanic rocks. *Earth Planet. Sci. Lett.* **57**, 285-304 (1982).
- Stern, R.A., Bodorkos, S., Kamo, S.L., Hickman, A.H., Corfu, F. Measurement of SIMS Instrumental Mass Fractionation of Pb Isotopes During Zircon Dating *Geostandards and Geoanalytical Research*, **33**, 145-168 (2009).
- Smithies, R. H., Lu, Y., Kirkland, C. L. *et al.* Oxygen isotopes trace the origins of Earth's earliest continental crust. *Nature* **592**, 70–75 (2021).
- Sreenivas, B., Dey, S, Rao, Y. J. B., Kumar, T. V., Babu, E. V. S. S. K., Williams, I. S. A new cache of Eoarchean detrital zircons from the Singhbhum craton, eastern India and constraints on early Earth geodynamics. *Geosci. Front.* **10**, 1359 (2019).
- Swanner, E.D., Mloszewska, A.M., Cirpka, O.A., Schoenberg, R., Konhauser, K.O., and Kappler, A. Modulation of oxygen production in Archean oceans by episodes of Fe(II) toxicity. *Nature Geoscience* **8** (2), 126-130 (2015).
- Walther, J. *Essentials of geochemistry*. Jones & Bartlett Learning (2009).
- Wang, D., Qiu, X., Carlson, R.W., The Eoarchean Muzidian gneiss complex: Long-lived Hadean crustal components in the building of Archean continents. *Earth and Planetary Science Letters*, **605**, 118037 (2023).
- White, William M. *Isotope geochemistry*. John Wiley & Sons, 2023.
- Windrim, D. P., & McCulloch, M. T. Nd and Sr isotopic systematics of central Australian granulites: chronology of crustal development and constraints on the evolution of lower continental crust. *Contributions to Mineralogy and Petrology*, **94**, 289-303 (1986).

- Xuan, H., Ziwei, B., DePaolo, D.J., Sm-Nd isotope study of early Archean rocks, Qianan, Hebei Province, China. *Geochim. Cosmochim. Acta*, **50**, 625-631 (1986).
- Tessalina, S., Bourdon, B., Van Kranendonk, M.*et al.* Influence of Hadean crust evident in basalts and cherts from the Pilbara Craton. *Nature Geosci* **3**, 214–217 (2010).
- Tachikawa, K., Jeandel, C., Roy-Barman, M. A new approach to the Nd residence time in the ocean: the role of atmospheric inputs. *Earth Planet. Sci. Lett.* **170**, 433-446 (1999).
- Taylor, H.P. The application of oxygen and hydrogen isotopic studies to problems of hydrothermal alteration and ore deposition. *Econ. Geol.* 843-883, (1974).
- Taylor H. P., JR. and Forester R. W. An oxygen and hydrogen isotope study of the Skaergaard intrusion and its country rocks: a description of a 55-m.y. old fossil hydrothermal system. *Petrol.* **20**, 355-419 (1979).
- Taylor, H.P. Jr. Stable isotope studies of spreading centers and their bearing on the origin of granoghyres and plagiogranites, in *Proceedings of the international meeting of mafic-ultramafic association in orogenic belts*, edited by C. Allegre, Centre National de Recherche scientifique, Grenoble, France, in press, 1980.
- Taylor, H.P. and Sheppard, S.M.F. Igneous rocks. I. Processes of isotopic fractionation and isotope systematics. *Rev. Mineral.*, **16**, 227-271 (1986).
- Taylor Jr., H.P., Comparison of hydrothermal systems in layered gabbros and granites, and the origin of low-<sup>18</sup>O magmas. In: Mysen, B.O. (Ed.), *Magmatic Processes: Physiochemical Principles*, *The Geochemical Society Special Publication*, **1**, 337-357 (1987).
- Tang, J., Zheng, Y., Gong, B., Wu, Y., Gao, T., Yuan, H., Wu, F., Extreme oxygen isotope signature of meteor water in magmatic zircon from metagranite in the Sulu orogen, China: Implications for Neoproterozoic rift magmatism. *Geochim. Cosmochim. Acta* **72**, 3139- 3169 (2008). Upadhyay, D., Chattopadhyay, S., Kooijman, E., Mezger, K., Berndt, J. Magmatic and metamorphic history of Paleoproterozoic tonalite–trondhjemite–granodiorite (TTG) suite from the Singhbhum craton, eastern India. *Precambrian Research*. **252**, 180-190 (2014).
- Terzer, S., Wassenaar, L. I., Araguás-Araguás, L. J., & Aggarwal, P. K. Global isoscapes for δ 18 O and δ 2 H in precipitation: improved prediction using regionalized climatic regression models. *Hydrology and Earth System Sciences*, *17*(11), 4713-4728 (2013).
- Troch, J., Ellis, B. S., Harris, C., Bachmann, O., & Bindeman, I. N. Low-δ<sup>18</sup>O silicic magmas on Earth: A review. *Earth-Science Reviews*, *208*, 103299 (2020).
- Turi, B., Taylor, H.P., An oxygen and hydrogen isotope study of a granodiorite pluton from the Southern California batholith. *Geochim. Cosmochim. Acta* **35**, 383-406 (1971).

- Upadhyay, D., Chattopadhyay, S., Kooijman, E., Mezger, K., & Berndt, J. Magmatic and metamorphic history of Paleoproterozoic tonalite–trondhjemite–granodiorite (TTG) suite from the Singhbhum craton, eastern India. *Precambrian research*, **252**, 180-190 (2014).
- Urey, H., On the early chemical history of the Earth and the origin of Earth. *Proc. Natl. Acad. Sci.* **38**, 351-363 (1952).
- Valley, J. W., Kinny, P. D., Schulze, D. J. & Spicuzza, M. J. Zircon megacrysts from kimberlite: oxygen isotope variability among mantle melts. *Contrib. Mineral. Petrol.* **133**, 1-11 (1998).
- Valley, J. W. Oxygen isotopes in zircon. *Rev. Mineral. Geochem.* **53**, 343-385 (2003).
- Valley, J. W. et al. 4.4 billion years of crustal maturation: oxygen isotope ratios of magmatic zircon. *Contrib. Mineral. Petrol.* **150**, 561-580 (2005).
- Van Kranendonk, M.J., Collins, W.J., Hickman, A., Pawley, M.J. Critical tests of vertical vs. horizontal tectonic models for the Archaean East Pilbara Granite–Greenstone Terrane, Pilbara Craton, Western Australia. *Precambrian Research*, **131**, 173-211 (2004).
- Van Kranendonk, M.J., Kröner, A., Hegner, E., and Connelly, J., Age, lithology and structural evolution of the c. 3.53 Ga Theespruit Formation in the Tjakastad area, southwestern Barberton Greenstone Belt, South Africa, with implications for Archaean tectonics: *Chemical Geology*, **261**, 115–139, (2009).
- Vermeesch, P. IsoplotR: a free and open toolbox for geochronology. *Geoscience Frontiers*. **9**, 1479-1493 (2018).
- Veizer, J., Hoefs, J. The nature of  $^{18}\text{O}/^{16}\text{O}$  and  $^{13}\text{C}/^{12}\text{C}$  secular trends in sedimentary carbonate rocks. *Geochim. Cosmochim. Acta*, **40**, 1387-1395 (1976).
- Vervoort, J.D., Patchett, P.J., Behavior of hafnium and neodymium isotopes in the crust: Constraints from Precambrian crustally derived granites. *Geochim. Cosmochim. Acta* **60**, 3717–3733 (1996).
- Vital, H. Statterger, K. Lowermost Amazon River: evidence of late quaternary sea-level fluctuations in a complex hydrodynamic system. *Quaternary International*. **72**, 53-60 (2000).
- Voosen, P. Ancient Earth was a water world. *Science*, **371**, 6534 (2021).
- Wallin, T. Metcalf, R.V., Supra-Subduction Zone Ophiolite Formed in an Extensional Forearc: Trinity Terrane, Klamath Mountains, *The Journal of Geology* , **106**, 591-608 (1998).
- Wallmann, K. The geological water cycle and the evolution of marine  $\delta^{18}\text{O}$  values. *Geochim. Cosmochim. Acta*, **65**, 2469-2485 (2001).

- Wang, C.Y., Campbell, I.H., Allen, C.M., Williams, I.S., Eggins, S.M., Rate of growth of the preserved North American continental crust: evidence from Hf and O isotopes in Mississippi detrital zircons. *Geochimica et Cosmochimica Acta* **73**, 712–728 (2009).
- Weber, J.N. The  $^{18}\text{O}/^{16}\text{O}$  ratio in ancient oceans. *Geokhimiya*, **6**, 674-680 (1955).
- Wei, C.-S., Zhao, Z.-F., Spicuzza, M.J., Zircon oxygen isotopic constraint on the sources of late Mesozoic A-type granites in eastern China. *Chem. Geol.* **250**, 1-15 (2008).
- Windley, B.F., Timing of continental growth and emergence. *Nature* **270**, 426-428 (1977).
- Wiedenbeck, M., Alle, P., Corfu, F., Griffin, W.L., Meier, M., Oberli, F., Von Quadt, A., Roddick, J.C. & Spiegel, W: Three natural zircon standards for U-Th-Pb, Lu-Hf, trace element and REE analyses. *Geostand. Newslett.*, **19**, 1–23 (1995).
- Wise, D. U., 1972, Freeboard of continents through time: *Geol. Soc. America Mem.* **132** (Hess vol.), 87-100 (1972).
- Wise, D.U. Continental margins, freeboard and the volumes of continents and oceans through time. In: Burk, C.A., Drake, C.L. (Eds.), *Geology of continental margins. Springer-Verlag, Berlin*, 45-58 (1974).
- White, W.M., Casey, W.H., Marty, B., Yurimoto., H. A comprehensive reference source on chemistry of the Earth. *Encyclopedia of Earth Sciences Series (Springer)*, **1**, 757-762 (2018).
- Whitehouse, M. Granulite fades Nd-isotopic homogenization in the Lewisian complex of northwest Scotland. *Nature* **331**, 705–707 (1988).
- Wilde, P., Quinby-Hunt, M., Erdtmann, B. D. The whole-rock cerium anomaly: a potential indicator of eustatic sea-level changes in shales of the anoxic facies. *Sedimentology Geology*, **101**, 43-53 (1996).
- Williams, I.S. (1998) U-Th-Pb Geochronology by Ion Microprobe. In: McKibben, M.A., Shanks III, W.C. and Ridley, W.I., Eds., *Applications of Microanalytical Techniques to Understanding Mineralizing Processes*, **7**, 1-35.
- Woodhead, J., Hergt, J., Shelley, M., Eggins, S. & Kemp, R. Zircon Hf-isotope analysis with an excimer laser, depth profiling, ablation of complex geometries, and concomitant age estimation. *Chem. Geol.*, **209**, 121–135 (2004).
- Woodhead, J.D. & Hergt, J.M. A preliminary appraisal of seven natural zircon reference materials for in situ Hf isotope determination. *Geostandards and Geoanalytical Research*, **29**, 183–195 (2005).
- Yang, Y. N., Wang, X. C., Li, Q. L., & Li, X. H. Integrated in situ U–Pb age and Hf–O analyses of zircon from Suixian Group in northern Yangtze: new insights into the

- Neoproterozoic low- $\delta^{18}\text{O}$  magmas in the South China Block. *Precambrian Research*, 273, 151-164 (2016).
- Yin J, Li H, Xiao K. Origin of Banded Iron Formations: Links with Paleoclimate, Paleoenvironment, and Major Geological Processes. *Minerals*. 13(4):547 (2023).  
<https://doi.org/10.3390/min13040547>
- Yung, Y. L., Wen, J. S., Moses, J. I., Landry, B. M., Allen, M., & Hsu, K. J. Hydrogen and deuterium loss from the terrestrial atmosphere: A quantitative assessment of nonthermal escape fluxes. *Journal of Geophysical Research: Atmospheres*, 94(D12), 14971-14989 (1989).
- Zhao, W., Liu, L., Chen, J., Ji, J. Geochemical characterization of major elements in desert sediments and implications for the Chinese loess source. *Science China Earth Sciences*. **62**, 1428-1440 (2019).
- Zhao, Z.F., Zheng, Y.F. Calculation of oxygen isotope fractionation in magmatic rocks. *Chemical Geology*, **193**, 59-80 (2003).
- Zhang, K., Shields, G.A. Sedimentary Ce anomalies: secular change and implications for paleoenvironmental evolution. *Earth-Science Reviews*, **229**, 104015 (2022).
- Zheng, Y-F., Wu, Y.-B., Chen, F.K., Gong, B., Li, L., Zhao, Z.-F. Zircon U-Pb and oxygen isotope evidence for a large-scale  $^{18}\text{O}$ -depletion event in igneous rocks during the Neoproterozoic. *Geochimica et Cosmochimica Acta*, **68**, 4145-4165 (2004).